physchem

MDPI

Review

Synergistic Interfaces: A Critical Review of Mono-, Bi-, Tri-, and Tetra Metal-Metal Oxide Heterostructured Nanoparticles for Biological (Antimicrobial and Anticancer) and Dye Degradation Applications

Renuka Gudepu [1], Azeema H. Shareef [2], Manohar Aele [3], Muralikrishna Cherukuru [4], Aditya Velidandi [5,*], Swati Dahariya [6] and Umme Thahira Khatoon [7]

[1] Department of Microbiology, Pingle Government College for Women (A), Warangal 506001, Telangana, India; renumanduva@gmail.com
[2] Clinical Research, Innospecs Bioresearch Pvt. Ltd., Chennai 600071, Tamil Nadu, India; azeema.hshareef@outlook.com
[3] ModernaTX, 1 Moderna Way, Norwood, MA 02062, USA; aelemanohar@gmail.com
[4] Ingenus Pharmaceuticals, 100 Ford Road, Denville, NJ 07834, USA; murali8556@gmail.com
[5] Department of Biotechnology, School of Sciences and Humanities, SR University, Warangal 506371, Telangana, India
[6] Department of Biotechnology, National Institute of Technology, Warangal 506004, Telangana, India; swati.dahariya@gmail.com
[7] Department of Chemical Engineering and Analytical Sciences, University of Manchester, Manchester M13 9PL, UK; ummethahirakhatoon@gmail.com
* Correspondence: aditya.velidandi@sru.edu.in

Abstract

The increasing crises of antimicrobial resistance and industrial water pollution demand innovative solutions beyond the reach of conventional materials. Metal-metal oxide heterostructured nanoparticles have emerged as powerful candidates, offering synergistic mechanisms that monometallic systems cannot achieve. This review critically examines the evolution of these materials from simple mono- and bimetallic constructs to complex tri- and tetrametallic architectures, focusing on their application in combating pathogens and degrading organic dyes. We present the fundamental role of the heterointerface (as a site for Schottky junctions, plasmonic enhancement, and cascade charge transfer) that underpins their superior performance. While bimetallic systems demonstrably enhance reactive oxygen species generation, broaden light absorption, and improve charge separation, the added value of progressing to higher-order systems remains uncertain. Tri- and tetra-metallic heterostructures show promise for multimodal theranostics and multi-pollutant degradation, yet the literature reveals a critical gap: a lack of standardized, head-to-head comparisons that would quantify whether escalating complexity yields proportional functional gains. By synthesizing mechanistic insights and quantitative performance data, we cross-examine the core premise of 'the more, the better.' Our analysis suggests that optimized bimetallic interfaces may represent a pragmatic peak in the cost–benefit landscape, while higher-order systems should be pursued only when they unlock clinically or environmentally relevant functionalities unattainable with simpler designs. This review provides a roadmap for rational heterostructure design, guiding researchers toward complexity that delivers true synergy over mere sophistication.

Academic Editors: Eralci Moreira Therézio and Paulo Ernesto Marchezi

Received: 9 October 2026
Revised: 6 November 2026
Accepted: 19 November 2026
Published: 22 November 2026

Copyright: © 2026 by the authors. Licensee MDPI, Basel, Switzerland. This article is an open access article distributed under the terms and conditions of the Creative Commons Attribution (CC BY) license.

Keywords: antimicrobial; heterostructures; nanoparticles; photocatalysis; synergistic interfaces

1. Introduction

1.1. The Dual Crisis of Antimicrobial Resistance and Environmental Pollution

Humanity faces impending global health and environmental crises that demand innovative materials-based solutions. Fungal infections alone claim an estimated 1.7 million lives annually and account for approximately 150 million cases worldwide, with the burden rising sharply due to expanding immunocompromised patient populations [1]. Beyond fungal pathogens, the proliferation of multidrug-resistant bacterial strains has reached alarming proportions. Recent surveillance of treated wastewater effluents has documented the persistence of 24 multidrug-resistant isolates even after conventional treatment processes [2], underscoring the inadequacy of existing antimicrobial strategies and the urgent need for alternative therapeutic platforms. The limited efficacy of traditional antibiotic drugs against multidrug-resistant strains, coupled with the slow pace of new antibiotic development, necessitates exploration of fundamentally different approaches to combat bacterial infections [3].

Parallel to the antimicrobial resistance crisis, industrial dye pollution poses severe threats to aquatic ecosystems and human health. Water pollution from textile, pharmaceutical, and chemical industries introduces recalcitrant organic dyes into water bodies, creating oxidative stress and long-term ecological damage [4]. These synthetic dyes resist conventional wastewater treatment methods, accumulate in the environment, and pose carcinogenic and mutagenic risks to exposed populations. The emergence of multidrug-resistant bacterial strains and persistent organic pollutants thus represent significant global threats requiring urgent attention to protect human health and environmental integrity [4].

Traditional remediation approaches (whether antibiotic therapy for infections or physicochemical methods for dye removal) have proven increasingly inadequate [5]. Antibiotics face resistance development, while conventional wastewater treatment technologies struggle with energy intensity, incomplete mineralization, and secondary pollution [6]. This dual crisis has catalyzed intensive research into nanomaterial-based platforms that can simultaneously address antimicrobial and environmental challenges through fundamentally different mechanisms of action.

1.2. The Fundamental Shift: From Monometallic Systems to Synergistic Heterostructures

The past 2 decades have witnessed a paradigm shift in functional nanomaterial design, moving from simple monometallic or single-oxide nanoparticles (NPs) toward increasingly sophisticated heterostructured architectures. This evolution reflects a growing recognition that the most powerful functional properties emerge not from individual components, but from carefully engineered interfaces between dissimilar materials. The concept of 'synergistic interfaces' has emerged as a central organizing principle: heterostructures can exhibit catalytic, antimicrobial, and photophysical properties that are fundamentally unattainable by their constituent materials individually.

The mechanistic foundations of interface-driven synergy are now well-established across multiple material platforms. In semiconductor heterojunctions, strategic band alignment creates built-in electric fields that drive spatial separation of photogenerated electron (e^-)-hole (h^+) pairs, dramatically suppressing recombination and enhancing photocatalytic quantum efficiency [7]. For example, $Ni_{0.5}Zn_{0.5}Fe_2O_4$@polyaniline decoration of

BiOCl demonstrates excellent improvement in photocatalytic degradation performance through band gap tuning and improved charge separation, with the heterogeneous interface suppressing recombination and enhancing radical generation under visible light [7]. Similarly, Mn_3O_4@ZnO hybrid materials achieve enhanced degradation efficiencies of up to 94.59% for methylene blue, attributed to higher charge-separation rates, increased catalytic sites, and a co-catalytic role of Mn_3O_4 that produces more oxidizing radicals compared with ZnO alone [8].

Plasmonic enhancement represents another powerful interface mechanism. When noble metal NPs such as Ag are integrated into semiconductor matrices, localized surface plasmon resonance (LSPR) effects extend light absorption into the visible spectrum, generate hot electrons, and create intense local electromagnetic fields that amplify photocatalytic activity. A ternary tetraaniline/Cu_2O/Ag nanocomposite exemplifies this principle, exhibiting lower bandgap energy and enhanced visible-light response when Ag is incorporated, consistent with plasmonic enhancement and extended absorption that increases photocatalytic activity versus the pure polymer or metal-oxide components [9]. The composite demonstrates promising applications in wastewater treatment with excellent performance in dye degradation under visible light due to a lower bandgap energy, visible light response, high absorptivity, and long-lived excitation [9].

Co-catalytic mechanisms further amplify heterostructure performance. When multiple metal or metal-oxide phases coexist at nanoscale interfaces, they can participate in complementary redox cycles, provide diverse active sites for multi-step reactions, and facilitate e^- transfer pathways that would be kinetically inaccessible in single-phase materials. Core–shell architectures represent a particularly elegant manifestation of interface engineering. Fe_3O_4-Ag core–shell nanostructures demonstrate substantially lower minimum inhibitory concentrations (MICs) than commercial antibiotics in microbial assays, with the core–shell architecture enhancing colloidal stability and bioactivity while providing magnetic recoverability as a functional benefit [10].

Quantitative evidence for synergistic enhancement has accumulated across diverse material systems. Ag-Zr NPs decorated on graphene oxide achieve up to 71% reduction in biofilm formation at sub-MICs compared with controls, attributed to synergistic interactions between Ag and Zr on the graphene oxide support [11]. Trimetallic silica nanohybrids exhibit the highest radical scavenging activity at approximately 90.67% and superior antifungal performance compared with bimetallic and monometallic counterparts, consistent with synergistic multimetal interactions [1]. These studies collectively document interface mechanisms (electron transfer and band alignment for heterojunctions, plasmonic contributions to visible absorption, and enhanced radical generation from co-catalytic sites) accompanied by quantifiable performance improvements.

1.3. The Core Premise: Does Complexity Yield Proportional Gains?

The demonstrated success of bimetallic and trimetallic heterostructures naturally raises a fundamental question that motivates this review: Does increasing the number of metal elements within metal-metal oxide heterostructures lead to proportional gains in antimicrobial and catalytic functionality, or does performance plateau or even decline beyond an optimal complexity threshold? This question has profound implications for rational nanomaterial design, resource utilization, and the practical translation of multimetallic systems from laboratory curiosities to scalable technologies.

Existing experimental evidence reveals a complex landscape. Monometallic systems establish baseline performance benchmarks. While impressive, these systems typically operate through single-mechanism pathways—either plasmonic photocatalysis (Ag, Au) or semiconductor photocatalysis (metal oxides)—limiting their functional versatility.

Bimetallic heterostructures demonstrate clear performance enhancements over their monometallic counterparts. Ag-doped CuO NPs (10% Ag-CuO) achieve approximately 98.9% rhodamine-B and 97.8% carmine photodegradation, with reported MICs for Ag/CuO formulations in the 100 to 120 μg/mL range and bactericidal concentrations of 150 to 300 μg/mL for complete microbial killing [12]. Bimetallic Ag-CuO nanohybrids exhibit MICs and minimum bactericidal concentrations (MBCs) against *Escherichia coli* and *Candida albicans* in the ranges of MIC 4 to 12 mg/mL and MBC 2 to 24 mg/mL, respectively [13]. $BiPO_4$/ZnO bimetallic nanocomposites show superior photocatalytic dye degradation and increased antibacterial inhibition zones (e.g., 20 mm inhibition against *Acinetobacter baumannii* at 80 μg/mL) compared with the component oxides [14]. These improvements are consistently attributed to synergistic interface effects—charge separation, complementary band structures, and dual-metal reactivity.

Trimetallic systems push performance boundaries further. Fe/Cu/Ag trimetallic NPs achieve 100% methyl orange degradation within 1 min under low pH conditions, following pseudo-first-order kinetics for rapid dye removal [15]. ZnO:NiO:CuO ternary heterojunctions degrade 96% methylene blue and 91% methyl orange in 90 min under sunlight [16]. Mesoporous Fe/Al/La trimetallic oxides report 93.85 ± 2% photodegradation for reactive black 5 under solar irradiation with pseudo-first-order kinetics and reusability up to 5 cycles [17]. Multiple studies directly comparing mono-, bi-, and tri-metallic formulations consistently report that trimetallic composites outperform bimetallic and monometallic variants within the same experimental framework, demonstrating higher radical scavenging activity, larger inhibition zones, and higher dye-degradation percentages [1,16,17].

However, critical gaps remain in our understanding of the complexity-functionality relationship. Tetrametallic systems are conspicuously underrepresented in the literature, with insufficient quantitative data for rigorous comparative analysis. More fundamentally, the existing studies lack standardized assay conditions, consistent performance metrics, and controlled series spanning mono → bi → tri → tetra metal compositions under identical experimental parameters. While individual reports demonstrate case-by-case gains with increasing metallic complexity, the field lacks population-level evidence to quantify whether these gains are proportional, whether diminishing returns emerge beyond a certain threshold, or whether optimal complexity depends on application domain (antimicrobial vs. photocatalytic), target substrate, or heterostructure architecture.

1.4. Scope and Organization of This Review

This review critically examines the current state of knowledge regarding metal-metal oxide heterostructured NPs, with a specific focus on how compositional complexity influences performance in 2 primary application domains: biomedical applications (antimicrobial activity against multidrug-resistant pathogens and anticancer properties) and environmental applications (photocatalytic degradation of organic dyes for wastewater treatment). We define heterostructured NPs broadly to encompass metal-decorated metal oxides, core–shell architectures, Janus particles, and intimately mixed multiphase nanocomposites where distinct metal and metal-oxide domains coexist at nanoscale interfaces. Figure 1 serves as the conceptual roadmap for the review.

By synthesizing quantitative data, mechanistic insights, and critical analysis across the mono- to tetra-metallic complexity spectrum, this review aims to provide a roadmap for next-generation heterostructure design. We seek to move beyond empirical trial-and-error toward predictive frameworks that guide researchers and engineers in selecting optimal compositional complexity for specific antimicrobial or environmental applications, ultimately accelerating the translation of synergistic heterostructures from laboratory

demonstrations to real-world impact in combating drug-resistant infections and remediating polluted water resources.

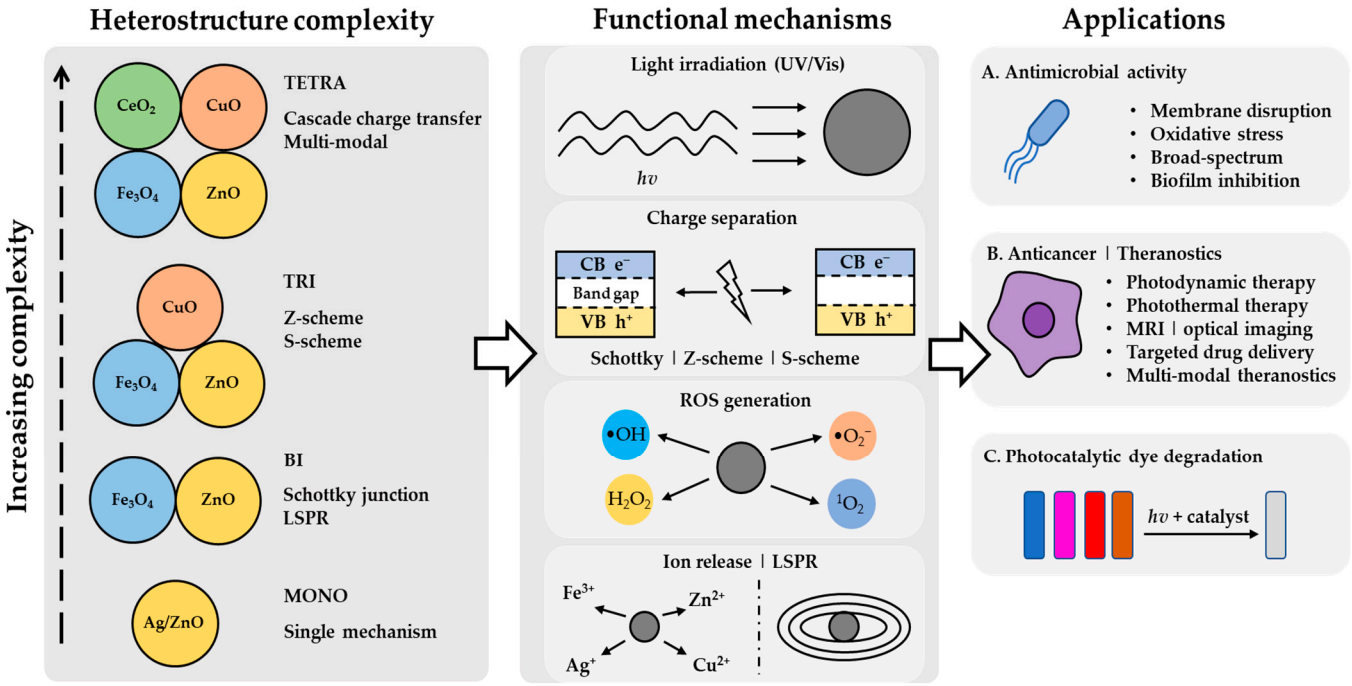


Figure 1. Schematic overview of heterostructure complexity in metal–metal oxide nanoparticles and the associated functional mechanisms and applications.

2. Synthesis Strategies and Architectural Control

The functional performance of metal-metal oxide heterostructured NPs in biological and dye degradation applications is fundamentally governed by the quality of the metal-oxide interface, which serves as the primary focus of synergistic interactions. While the literature frequently emphasizes compositional diversity (spanning mono-, bi-, tri-, and tetra-metallic systems), the critical determinant of enhanced catalytic activity, charge transfer efficiency, and reactive oxygen species (ROS) generation is not merely the presence of multiple elements, but rather the establishment of intimate, defect-minimized interfacial contact between metallic and oxide domains [18,19]. True heterostructure formation, characterized by epitaxial or near-epitaxial junctions with continuous lattice registry and minimal interfacial strain, enables efficient e− transfer, localized electric field enhancement, and cooperative catalytic mechanisms that are absent in simple physical mixtures or poorly integrated composites [20,21]. Consequently, synthesis strategies must be evaluated not only for their ability to incorporate multiple metallic species, but more critically for their capacity to engineer high-quality interfaces with controlled crystallographic orientation, minimal amorphous interlayers, and tunable electronic coupling. This section critically reviews how synthesis methodologies (from monometallic oxide preparation through increasingly complex multimetallic deposition sequences) dictate interfacial architecture and, by extension, the synergistic properties that underpin advanced catalytic applications.

2.1. Monometallic Base Oxide Synthesis

The synthesis of monometallic base oxides constitutes the foundational step in heterostructure fabrication, as the crystallinity, surface chemistry, morphology, and defect density of the oxide substrate directly influence subsequent metal deposition and interfacial quality. Established wet-chemical routes (including sol–gel, hydrothermal, co-

precipitation, and emerging green synthesis approaches) offer distinct advantages and limitations in controlling these critical parameters across a diverse range of metal oxides.

2.1.1. Sol–Gel and Seeded Growth Strategies

Sol–gel chemistry, particularly when implemented as a seeded growth strategy, enables precise control over oxide shell thickness and crystallinity through manipulation of precursor concentration, hydrolysis kinetics, and thermal treatment protocols. The synthesis of Fe_3O_4@TiO_2 core–shell NPs exemplifies this approach: magnetite cores prepared via co-precipitation serve as nucleation sites for TiO_2 shell growth from titanium alkoxide precursors, with shell thickness controlled by the stoichiometric ratio of titania precursor to core surface area [19]. High-resolution transmission electron microscopy (HR-TEM) lattice fringe analysis confirmed intimate contact between the Fe_3O_4 core (lattice spacing ~0.48 nm for [111] planes) and the anatase TiO_2 shell (lattice spacing ~0.35 nm for [101] planes), with X-ray diffraction (XRD) and X-ray photoelectron spectroscopy (XPS) corroborated by inductively coupled plasma atomic emission spectroscopy (ICP-AES) validating phase purity and compositional stoichiometry [19]. The sol–gel route's versatility extends to diverse oxide systems, including CeO_2 shells grown via aqueous cerium nitrate hydrolysis in alkaline citrate media at room temperature, and Cu_2O shells formed through controlled reduction in $CuCl_2$ with hydroxylamine on gold seed particles [18]. Critical to interface quality is the post-synthesis calcination step, which promotes crystallization and removes residual organic ligands, though excessive temperatures risk sintering and loss of nanostructure definition.

2.1.2. Hydrothermal and Solvothermal Synthesis

Hydrothermal synthesis, conducted in sealed autoclaves under elevated temperature and autogenous pressure, facilitates crystallization of metal oxides with high crystallinity and controlled morphology. The synthesis of ZnO@Fe_3O_4 composite nanostructures via hydrothermal treatment yielded materials with optical band gaps in the range of 2.0 to 2.1 eV, as determined by ultraviolet (UV)-visible (Vis) diffuse reflectance spectroscopy, indicating successful integration of the 2 oxide phases [22]. Hydrothermal conditions promote dissolution-recrystallization mechanisms that enhance crystallinity and reduce defect densities, thereby improving the electronic properties critical for subsequent metal deposition. Solvothermal variants, employing organic solvents such as octadecene or dioctyl ether, enable higher reaction temperatures (200 to 300 °C) and are particularly effective for synthesizing Fe_3O_4 shells on noble metal cores through thermal decomposition of $Fe(CO)_5$ [18]. The choice of solvent, surfactant (e.g., oleylamine, oleic acid), and temperature profile governs particle size distribution, surface functionalization, and the density of coordinatively unsaturated surface sites that serve as anchoring points for subsequent metal deposition.

2.1.3. Co-Precipitation and Wet-Chemical Precipitation

Co-precipitation, involving simultaneous precipitation of metal hydroxides or oxides from aqueous salt solutions via pH adjustment, is widely employed for synthesizing magnetite (Fe_3O_4) and spinel-structured oxides. The synthesis of Co_3O_4 cores, subsequently used in Co_3O_4–$Mn_xCo_{3-x}O_4$ core–shell architectures, employed cobalt acetate and potassium hydroxide as reagents, with pH control during precipitation governing particle size and morphology [23]. TEM and XRD analyses revealed an average particle size of approximately 19.8 nm for the Co_3O_4 cores, with Scherrer analysis of XRD peak broadening providing complementary crystallite size estimates [23]. The co-precipitation method's simplicity and scalability are offset by challenges in achieving narrow size distributions

and preventing aggregation, necessitating careful control of supersaturation, stirring rate, and the use of capping agents or surfactants to stabilize nascent particles.

2.1.4. Green Synthesis Approaches

Biogenic synthesis routes, employing plant extracts or microbial metabolites as reducing and stabilizing agents, represent an environmentally benign alternative to conventional chemical methods. The synthesis of ZnO@TiO_2 bimetallic oxide nanocomposites using *Cinnamomum verum* (cinnamon) bark extract as a biogenic reductant and capping agent yielded NPs with controlled morphology and surface functionalization [24]. While green synthesis offers advantages in terms of reduced toxicity and waste generation, the mechanistic complexity of biomolecule-mediated reduction and the batch-to-batch variability of natural extracts pose challenges for reproducibility and precise control over particle size, crystallinity, and surface chemistry. Nonetheless, the mild reaction conditions and inherent biocompatibility of green-synthesized oxides are advantageous for biological applications.

2.1.5. Surface Properties and Subsequent Metal Deposition

Irrespective of the synthesis route, the surface properties of monometallic base oxides—including hydroxyl group density, surface charge (zeta potential), crystallographic facet exposure, and defect concentration—critically determine the efficiency and selectivity of subsequent metal deposition. High surface area oxides with abundant hydroxyl groups facilitate electrostatic adsorption of metal precursor ions, while specific crystallographic facets may exhibit preferential nucleation kinetics due to differences in surface energy and atomic coordination. Brunauer–Emmett–Teller (BET) surface area measurements, though not consistently reported across all studies, provide essential metrics for normalizing catalytic activity and understanding metal dispersion. For instance, sub-5 nm Au-Cu bimetallic cores encapsulated in mesoporous SiO_2 shells exhibited bimodal porous structures with high surface areas, as confirmed by BET analysis, enabling enhanced catalytic activity for carbon monoxide (CO) oxidation at elevated temperatures [25].

2.2. Bimetallic Heterostructure Synthesis: Controlled Metal Deposition

The transition from monometallic oxides to bimetallic heterostructures introduces the critical challenge of achieving selective, uniform deposition of secondary metals (Ag, Au, Pt, Pd, Cu, Ni, Co, Fe, Ru, Rh, Ir) onto oxide substrates while maintaining interfacial integrity and preventing undesired alloying, galvanic replacement, or phase segregation. Multiple deposition techniques (photodeposition, chemical reduction, impregnation, seed-mediated growth, electrochemical deposition, and green synthesis) offer distinct control parameters and yield architectures ranging from decorated NPs to conformal core–shell structures.

2.2.1. Photodeposition: Light-Driven Interfacial Synthesis

Photodeposition exploits photogenerated charge carriers in semiconducting oxides to drive in situ reduction of metal precursors at the oxide surface, yielding intimate metal-oxide contact with minimal interfacial contamination. A surfactant-free photodeposition strategy on reduced graphene oxide (rGO) enabled the synthesis of diverse core–shell bimetallic nanostructures by controlling the sequence of metal precursor introduction and the duration of UV irradiation [20]. Surface photovoltage microscopy and XPS analysis provided direct evidence of photogenerated e^- transfer from the rGO substrate to deposited Pd NPs, confirming electronic coupling at the metal-support interface [20]. In a model system employing atomic layer deposition-grown anatase TiO_2 thin films, sequential photodeposition of Au followed by Ag yielded Au-core/Ag-shell NPs with low areal densities

(<100 μm^{-2}), whereas reversing the deposition order (Ag first, then Au) resulted in Au-Ag alloy formation due to galvanic replacement of Ag by Au^{3+} ions [26]. This deposition-order dependence underscores the critical role of redox potentials and kinetic barriers in dictating architectural outcomes. Control parameters in photodeposition include light intensity, irradiation duration, metal precursor concentration, and the presence of h^+ scavengers (e.g., methanol, ethanol) to suppress photocorrosion and enhance quantum efficiency.

2.2.2. Chemical Reduction and Seed-Mediated Growth

Chemical reduction employing mild reducing agents (e.g., ascorbic acid, sodium borohydride ($NaBH_4$), hydrazine) enables room-temperature (RT) or low-temperature deposition of noble metals onto oxide supports with precise control over particle size and shell thickness. A seed-mediated approach for synthesizing Ag@M (M = Au, Pt, Pd) core–shell nanoplates (Figure 2) employed Ag nanoplates as seeds, with ascorbic acid as the reducing agent and poly(vinylpyrrolidone) (PVP) as a stabilizer [27]. Critically, pH control via sodium hydroxide addition was essential to prevent galvanic dissolution of the Ag core by Au^{3+}, Pt^{2+}, or Pd^{2+} ions, with higher pH (>10) promoting uniform shell growth and preserving core integrity [27]. HR-TEM lattice fringe analysis confirmed epitaxial or near-epitaxial growth of Au, Pt, and Pd shells on Ag [111] facets, with lattice spacings of 0.235 nm (Au), 0.226 nm (Pt), and 0.224 nm (Pd) closely matching the Ag [111] spacing of 0.236 nm [27]. Energy-dispersive X-ray spectroscopy (EDX) elemental mapping validated the core–shell architecture and quantified compositional gradients across the nanostructure. The reducing agent concentration, addition rate, and reaction temperature are critical parameters: excessive reducing agent can induce homogeneous nucleation of secondary metal particles rather than heterogeneous deposition on the oxide surface, while insufficient reducing power results in incomplete shell coverage.

2.2.3. Impregnation and Reverse Micelle Encapsulation

Impregnation methods, involving adsorption of metal precursor salts onto oxide supports followed by thermal reduction or calcination, are widely employed in heterogeneous catalysis but often yield broad metal particle size distributions and limited control over interfacial architecture. A more sophisticated variant, reverse micelle (water-in-oil microemulsion) encapsulation, confines metal precursor reduction within nanoscale aqueous droplets, enabling synthesis of sub-5 nm Au-Cu bimetallic cores subsequently encapsulated in mesoporous SiO_2 shells [25]. The synthesis protocol involved $HAuCl_4$ and $Cu(NO_3)_2$ reduction within Igepal CO-520 reverse micelles, followed by tetraethyl orthosilicate hydrolysis to form the SiO_2 shell, and final calcination at 550 °C under hydrogen to reduce Cu^{2+} to metallic Cu [25]. HR-TEM confirmed sub-5 nm bimetallic cores with intimate Au-Cu contact, while XRD and XPS verified the metallic state and compositional homogeneity. The SiO_2 encapsulation prevented sintering and maintained high dispersion even at elevated temperatures (up to 500 °C), demonstrating the utility of encapsulation strategies for stabilizing reactive bimetallic interfaces [25].

2.2.4. Electrochemical Deposition

Electrochemical deposition offers unparalleled temporal control, enabling ultrafast metal deposition on conductive oxide substrates. Pt/Au core–shell NPs were deposited on TiO_2 nanotube arrays via pulsed electrodeposition in as little as 60 s, without requiring additional reducing agents or thermal treatment [28]. The deposition potential, pulse duration, and electrolyte composition (metal salt concentration, pH, supporting electrolyte) govern nucleation density, particle size, and shell conformality. Electrochemical methods are particularly advantageous for fabricating electrode-integrated heterostructures for

photoelectrochemical and electrocatalytic applications, though they are limited to conductive or semiconducting oxide substrates.

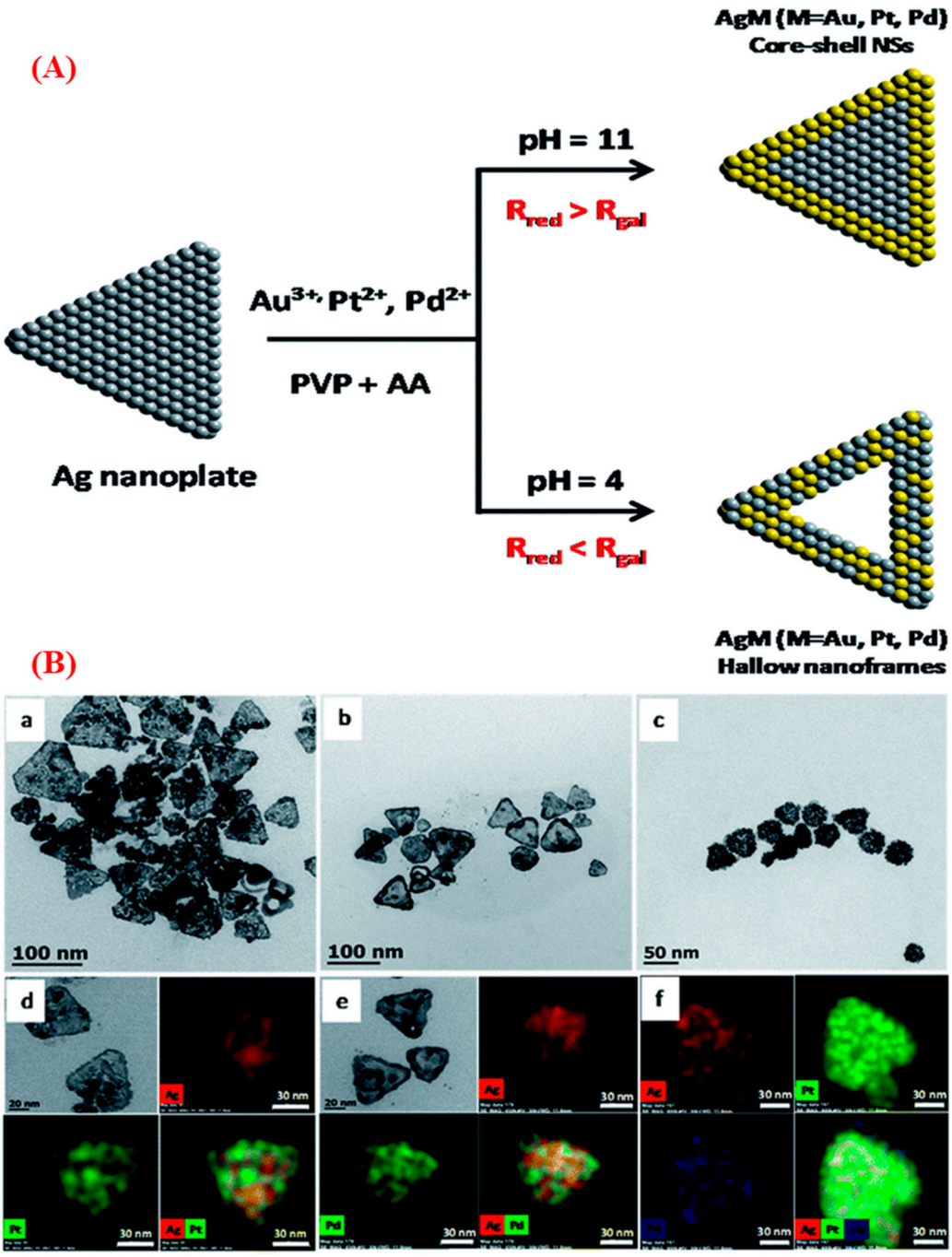


Figure 2. (**A**) A schematic representation outlining the synthesis process for creating triangular core–shell nanostructures composed of AgM (where M = Au, Pt, or Pd) and their corresponding hollow nanoframes. (**B**) TEM and scanning transmission electron microscopy (STEM)-EDX mapping images of Ag@Pt (**a** and **d**), Ag@Pd (**b** and **e**), and Ag@PdPt (**c** and **f**) nanoplates, respectively. Reproduced from [27].

2.2.5. Green Synthesis of Bimetallic Heterostructures

Biogenic synthesis routes have been extended to bimetallic systems, with plant extracts serving as both reducing and capping agents. While offering environmental benefits, green synthesis of bimetallic heterostructures faces challenges in achieving selective, sequential reduction in multiple metal precursors with distinct redox potentials, often

resulting in alloyed rather than core–shell architectures [29,30]. Nonetheless, the mild reaction conditions and biocompatible surface functionalization are advantageous for biological applications.

2.3. Trimetallic Heterostructure Synthesis: Increasing Complexity

The synthesis of trimetallic heterostructures introduces formidable challenges in maintaining phase segregation, controlling stoichiometry, and preserving clean interfaces across multiple metal-metal and metal-oxide junctions. Sequential deposition strategies, one-pot competitive reaction approaches, and advanced thermal decomposition methods have been developed to address these challenges, though each approach entails trade-offs in synthetic complexity, scalability, and architectural precision.

2.3.1. Sequential Deposition and Mask-Assisted Strategies

Mask-assisted seeded growth represents a paradigm for achieving segmented metallic heterotrimers with spatially resolved metal domains. In this approach, Au seed particles are first partially encapsulated in SiO_2 via controlled hydrolysis of tetraethyl orthosilicate in a water-in-oil microemulsion, creating Au-SiO_2 dumbbell structures in which the SiO_2 mask blocks a portion of the Au surface [21]. Subsequent reduction of K_2PdCl_4 with ascorbic acid in the presence of PVP selectively deposits Pd on the exposed Au surface, yielding Pd-Au heterodimers with lattice spacings of 0.236 nm (Au [111]) and 0.228 nm (Pd [111]), indicative of epitaxial growth [21]. Removal of the SiO_2 mask via HF etching, followed by a second masking and deposition cycle with K_2PtCl_4, produces Pt-Pd-Au heterotrimers with controlled domain sizes (Pd thickness: 4, 7, or 10 nm, depending on precursor concentration) [21]. HR-TEM confirmed continuation of lattice fringes across the Pd-Au and Pt-Pd interfaces, demonstrating intimate contact and epitaxial registry. EDX elemental mapping validated the spatial segregation of Au, Pd, and Pt domains, confirming the absence of significant interdiffusion or alloying [21]. The mask-assisted seeded growth method's precision comes at the cost of synthetic complexity, requiring multiple masking, deposition, and etching cycles, and is challenging to scale beyond laboratory quantities.

2.3.2. Total-Synthesis Framework for Stepwise Assembly

A 'total-synthesis' framework, inspired by organic synthesis methodologies, employs chemoselective, regiospecific, and sequential solid-state reactions to construct high-order colloidal heterostructures, including M-Pt-Fe_3O_4 heterotrimers and higher-order oligomers [31]. This approach leverages the distinct reactivity of different metal and oxide domains: for example, Fe_3O_4 NPs can be selectively functionalized with thiol ligands, enabling subsequent attachment of Au NPs via Au-S bonding, followed by Pt deposition on the Au domain via seed-mediated growth [31]. The stepwise nature of the synthesis allows for precise control over the number, size, and spatial arrangement of each component, with HR-TEM, selected area electron diffraction (SAED), and multi-element STEM-EDX mapping providing comprehensive structural and compositional characterization. However, the multi-step protocol is labor-intensive and requires careful optimization of each reaction to prevent cross-reactivity or loss of previously assembled domains.

2.3.3. One-Pot Competitive Reaction Approaches

One-pot synthesis strategies, employing coupled competitive reactions with kinetic control over nucleation and growth, offer a more streamlined route to trimetallic heterostructures. A hybrid process combining sequential reducing-nucleation and co-precipitation reactions enabled temporal separation of alloy core formation and surface gradient-doping shell growth, thereby avoiding lattice mismatch and phase separation [32]. Kinetic

control over latent nucleation times—achieved by manipulating precursor concentration, reducing agent strength, and reaction temperature—serves as the primary lever for ordering components and preventing undesired alloying [32]. Microfluidic reactors, with their precise control over mixing, residence time, and temperature gradients, are particularly well-suited for implementing competitive reaction strategies, enabling high-throughput screening of synthesis conditions. However, one-pot methods generally afford less architectural precision than sequential approaches, and the resulting heterostructures may exhibit compositional gradients or partial alloying at interfaces.

2.3.4. Thermal Decomposition and Selective Etching

Thermal decomposition of organometallic precursors in high-boiling-point solvents (e.g., octadecene, oleylamine) enables synthesis of Cu-PGM (platinum group metal: Ru, Rh, Ir) core–shell NPs with controlled surface segregation of the PGM shell [33]. The synthesis protocol involves co-decomposition of Cu and PGM precursors at elevated temperatures (200 to 300 °C), followed by controlled cooling to promote surface segregation of the PGM due to its lower surface energy [33]. Subsequent selective etching of the Cu core with mild oxidants (e.g., $Fe(NO_3)_3$) yields hollow PGM shells with tunable wall thickness, as confirmed by HR-TEM and EDX mapping [33]. This thermal decomposition-etching strategy offers a route to complex architectures (e.g., yolk-shell, hollow) that are difficult to achieve via sequential deposition, though it requires careful control of decomposition kinetics and etching selectivity to prevent collapse or aggregation of the hollow structures.

2.3.5. Phase Separation Challenges and Mitigation

Phase separation (manifested as uncontrolled alloying, domain coarsening, or loss of interfacial definition) is a pervasive challenge in trimetallic synthesis. The reversal of deposition order in Au/Ag photodeposition, which transformed the architecture from Au-core/Ag-shell to Au-Ag alloy via galvanic replacement, exemplifies how redox potentials and kinetic barriers dictate phase behavior [26]. Mitigation strategies include: (i) pH control to suppress galvanic replacement, as demonstrated in Ag@Au/Pt/Pd shell formation [27]; (ii) use of masking agents (e.g., SiO_2, polymers) to spatially confine deposition [21]; (iii) kinetic trapping via rapid quenching or low-temperature synthesis to prevent thermodynamically favored alloying; and (iv) encapsulation in inert shells (e.g., SiO_2, CeO_2) to prevent sintering and interdiffusion during post-synthesis thermal treatments [25,34].

2.4. Tetrametallic Heterostructure Synthesis: Frontier Challenges

Tetrametallic heterostructures, incorporating 4 distinct metallic or oxide components, represent the current frontier of synthetic complexity, requiring advanced methodologies to achieve controlled stoichiometry, prevent phase mixing, and maintain interfacial integrity across multiple junctions (Figure 3). The limited number of reported tetrametallic systems reflects the formidable synthetic challenges, though emerging strategies offer pathways to these architecturally sophisticated materials.

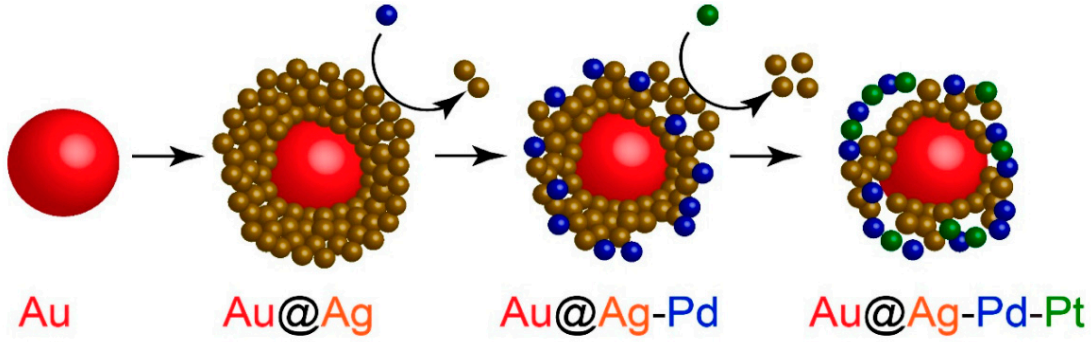


Figure 3. Schematic representation of NPs synthesis. Reproduced from [35].

2.4.1. Total-Synthesis of Heterotetramers

The total-synthesis framework has been extended to heterotetramers, such as M_xS–Au–Pt–Fe_3O_4 oligomers, through iterative application of chemoselective coupling reactions [31]. Each addition step exploits the unique surface chemistry of the most recently added domain: for example, Fe_3O_4 NPs are functionalized with thiol ligands to enable Au attachment; the Au domain is then used as a seed for Pt growth; and finally, metal sulfide (M_xS) NPs are attached via ligand exchange or direct bonding to the Pt surface [31]. HR-TEM, SAED, and multi-element STEM-EDX mapping are essential for confirming the spatial arrangement and compositional identity of each domain. The stepwise nature of the synthesis allows for precise architectural control but is synthetically demanding and difficult to scale.

2.4.2. Quaternary Heterojunction Systems

Quaternary heterojunctions, in which a fourth component is deposited onto a ternary oxide substrate, offer an alternative route to tetrametallic functionality. A Pd nanoparticle-decorated ternary $Bi_2O_2CO_3$–Bi_2MoO_6–CuO heterojunction was synthesized via a combined solvothermal-chemical reduction approach: the ternary oxide heterojunction was first prepared by solvothermal treatment of Bi, Mo, and Cu precursors, followed by photodeposition or chemical reduction in Pd^{2+} to deposit Pd NPs on the oxide surface [36]. Field-emission scanning electron microscopy (FE-SEM), powder XRD, HR-TEM, EDX mapping, and Fourier-transform infrared spectroscopy (FTIR) provided comprehensive structural and compositional characterization, confirming the coexistence of the 3 oxide phases and the spatial distribution of Pd NPs (Figure 4) [36]. Photoelectrochemical measurements, including cyclic voltammetry, chronoamperometry, and electrochemical impedance spectroscopy (EIS), demonstrated enhanced charge transfer and catalytic activity for ethanol oxidation, attributed to synergistic interactions at the multiple metal-oxide interfaces [36]. The solvothermal-chemical reduction approach is more scalable than total-synthesis methods but offers less precise control over the spatial arrangement of components.

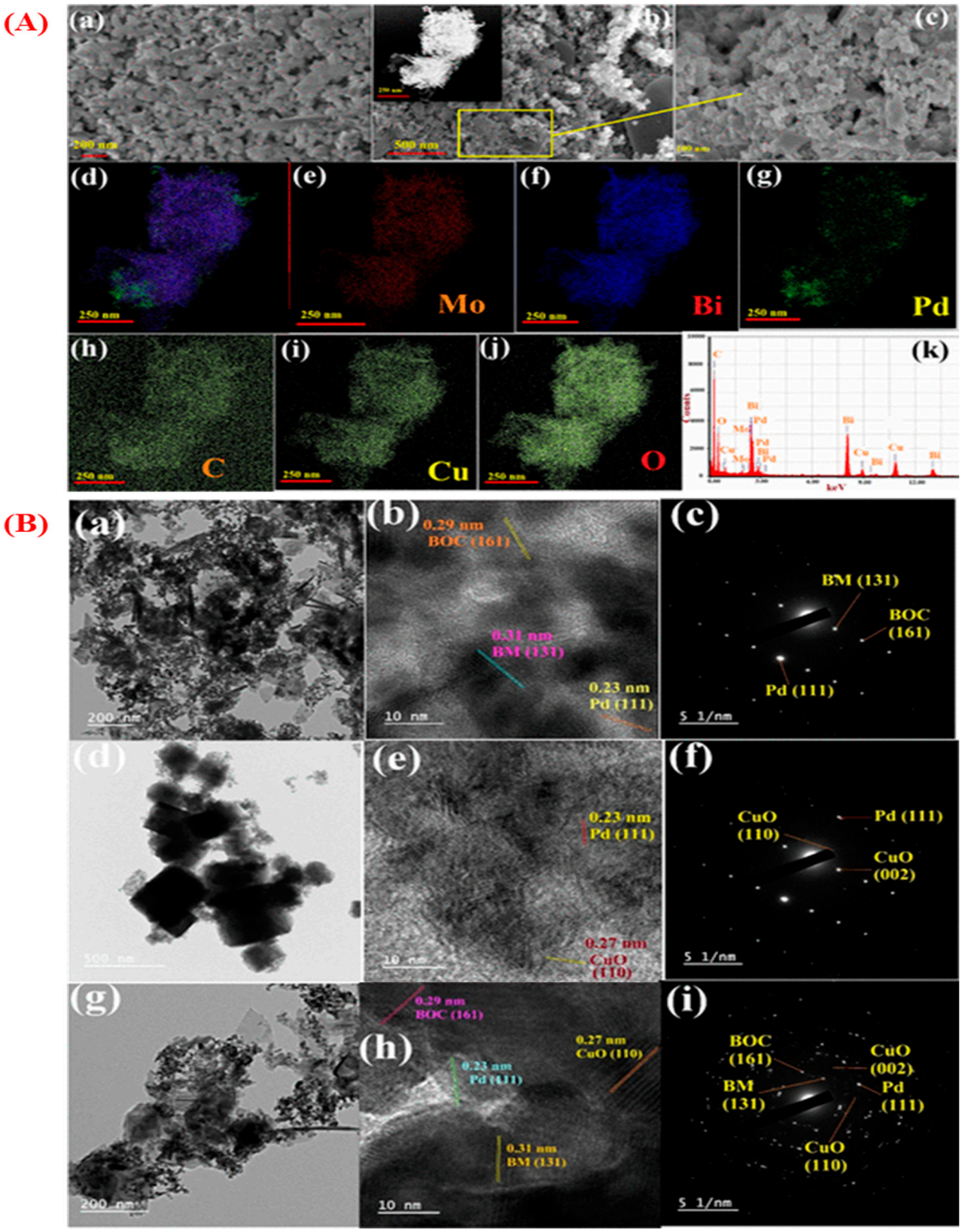


Figure 4. (**A**) FE-SEM images of the Pd/Bi_2MoO_6–$Bi_2O_2CO_3$ catalyst (**a**) and the Pd/Bi_2MoO_6–$Bi_2O_2CO_3$–CuO catalyst (**b**). The inset in (**b**) and panel (**c**) display elemental mapping images showing the overlay of all elements (**d**), along with individual maps for Mo (**e**), Bi (**f**), Pd (**g**), C (**h**), Cu (**i**), and O (**j**). Panel (**k**) presents the corresponding EDX spectrum obtained from FE-SEM. (**B**) TEM images, HR-TEM images, and SAED patterns of the Pd/Bi_2MoO_6–$Bi_2O_2CO_3$ (**a**–**c**), Pd/CuO (**d**–**f**), and Pd/Bi_2MoO_6–$Bi_2O_2CO_3$–CuO (**g**–**i**) catalysts, respectively. Reproduced from [36].

2.4.3. High-Entropy and Complex Stoichiometry Control

High-entropy alloy NPs, incorporating 5 or more metallic elements in near-equimolar ratios, represent an emerging class of multimetallic materials with unique catalytic and electronic properties [37]. However, achieving controlled stoichiometry and preventing phase separation in high-entropy systems remains a significant challenge, particularly when integrating oxide components [38]. Strategies under development include: (i) rapid quenching from high-temperature melts to kinetically trap homogeneous solid solutions; (ii) co-reduction in multiple metal precursors in the presence of strong complexing agents to equalize reduction kinetics; and (iii) atomic layer deposition or chemical vapor deposition to achieve atomic-scale compositional control [39]. The application of these methods to oxide-supported high-entropy NPs is an active area of research.

2.4.4. Encapsulation Strategies to Prevent Sintering and Phase Mixing

Encapsulation in chemically inert, thermally stable shells (e.g., SiO_2, CeO_2, Al_2O_3) is a critical strategy for stabilizing tetrametallic heterostructures against sintering, interdiffusion, and phase mixing during post-synthesis treatments or catalytic operation at elevated temperatures. CeO_2-encapsulated noble metal nanocatalysts exhibited enhanced activity and stability for CO oxidation, with the CeO_2 shell providing both physical confinement and electronic modification via metal-support interactions [34]. The encapsulation shell must be sufficiently thin and porous to allow reactant access to the active metal surface while providing effective stabilization, a balance achieved through careful control of shell growth kinetics and post-synthesis calcination conditions. Mesoporous SiO_2 shells, with pore sizes in the 2 to 10 nm range, offer an optimal compromise between accessibility and stabilization [25].

3. Characterization: Confirmation of Heterostructure Formation and Interface Quality

The synthesis of high-quality metal-metal oxide heterostructures must be rigorously validated through a comprehensive suite of characterization techniques that probe structure, composition, and electronic properties at multiple length scales. Characterization is not merely a post-synthesis verification step but an integral component of the synthesis-structure-property feedback loop, enabling iterative optimization of synthetic protocols to achieve target architectures.

3.1. HR-TEM

HR-TEM is the gold standard for confirming heterostructure formation (Figure 5) and assessing interfacial quality at the atomic scale. Lattice fringe imaging enables direct visualization of crystallographic planes and measurement of lattice spacings, providing unambiguous identification of phases and assessment of epitaxial relationships. In Fe_3O_4@TiO_2 core–shell NPs, HR-TEM revealed lattice spacings of ~0.48 nm (Fe_3O_4 [111]) and ~0.35 nm (anatase TiO_2 [101]), with continuous lattice fringes across the core–shell interface indicating intimate contact and minimal amorphous interlayer [19]. In Pd-Au heterodimers synthesized via mask-assisted seeded growth, HR-TEM showed continuation of lattice fringes from Au [111] planes (0.236 nm) to Pd [111] planes (0.228 nm), demonstrating epitaxial growth despite the ~3.4% lattice mismatch [21]. Particle size distributions, essential for assessing synthesis reproducibility, are routinely extracted from HR-TEM images: Co_3O_4 core–shell NPs exhibited an average size of 19.8 nm, with a narrow size distribution indicative of well-controlled synthesis [23]. Sub-5 nm Au-Cu bimetallic cores encapsulated in SiO_2 shells were confirmed by HR-TEM, demonstrating the technique's capability to resolve ultrasmall NPs [25].

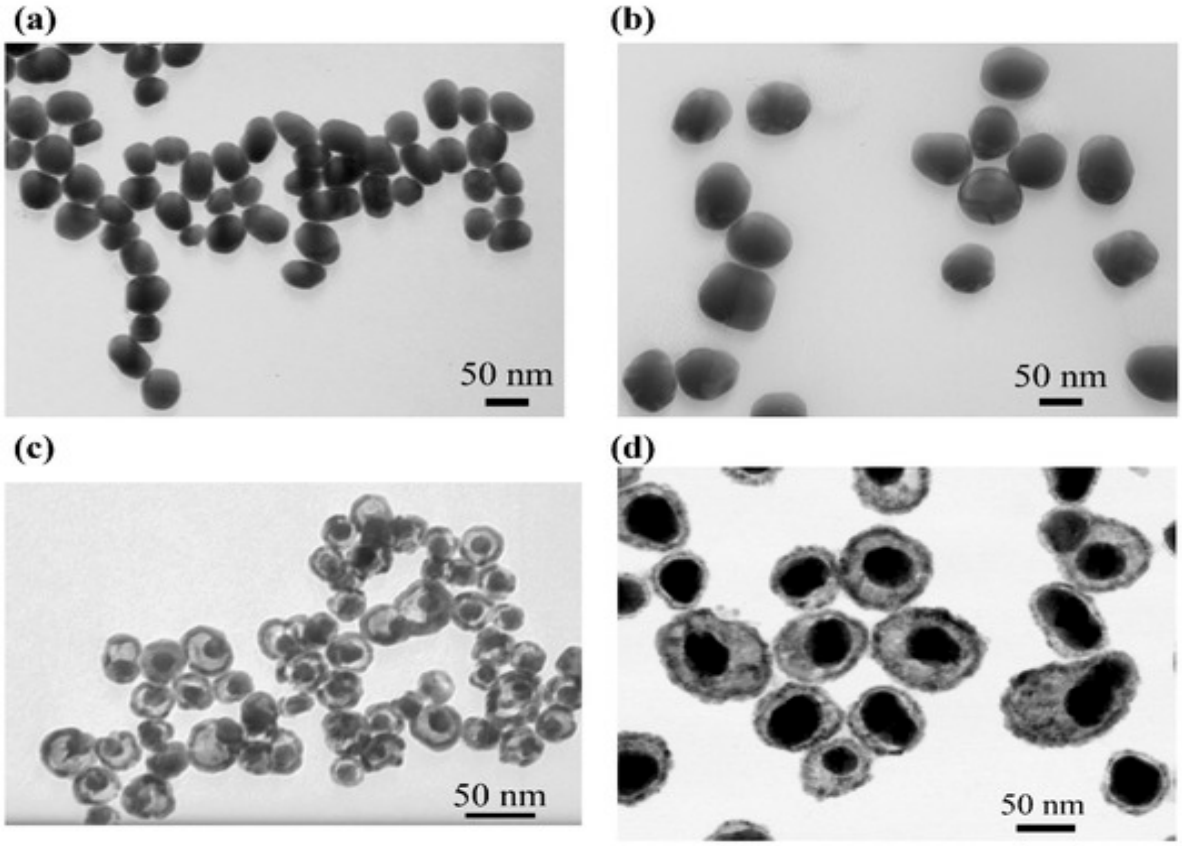


Figure 5. TEM micrographs of synthesized NPs: (**a**) Au (55 nm); (**b**) Au/Ag (55 nm, 400 μM Ag); (**c**) Au/Ag/Pd (15 nm Au, 100 μM Ag, 50% Pd); (**d**) Au/Ag/Pd/Pt (40 nm Au, 400 μM Ag, 25% Pd, 40% Pt). Reproduced from [35].

3.2. XPS

XPS provides surface-sensitive (probing depth ~5 to 10 nm) information on elemental composition, oxidation states, and chemical bonding, making it indispensable for characterizing metal-oxide interfaces. Binding energy shifts in core-level spectra indicate charge transfer and electronic interactions between metal and oxide domains. In photodeposited Pd NPs on rGO, XPS analysis combined with surface photovoltage microscopy revealed photogenerated electron transfer from rGO to Pd, evidenced by a negative shift in the Pd 3d binding energy and enhanced surface photovoltage under illumination [20]. Correlation of XPS-derived compositions with ICP-AES measurements provides validation of bulk stoichiometry and assessment of surface enrichment or depletion: in Fe_3O_4@TiO_2 core–shell NPs, XPS and ICP-AES data were in good agreement, confirming the absence of significant surface segregation [19]. Oxidation state determination via XPS is critical for distinguishing metallic, oxide, and mixed-valence species: in Cu-based heterostructures, XPS can differentiate Cu^0, Cu^+, and Cu^{2+} based on the Cu 2p binding energy and Auger parameter.

3.3. XRD and SAED

XRD provides bulk-averaged information on crystalline phases, lattice parameters, and crystallite sizes, complementing the local information obtained from HR-TEM. Phase identification via comparison with reference patterns (e.g., Joint Committee on Powder Diffraction Standards (JCPDS) database) confirms the presence of target phases and detects impurities or secondary phases. In Co@Ag core–shell NPs, XRD revealed coexistence of hexagonal close-packed Co and face-centered cubic Ag phases, with no evidence of

intermetallic compound formation [40]. Crystallite size estimation via the Scherrer equation, applied to XRD peak broadening, provides an independent measure of particle size: for Co_3O_4–$Mn_xCo_{3-x}O_4$ core–shell NPs, Scherrer analysis yielded a crystallite size of ~19.8 nm, in excellent agreement with TEM measurements [23]. SAED, performed in the TEM, provides single-particle or small-ensemble diffraction patterns, enabling assessment of crystallographic orientation relationships and detection of epitaxial growth. Fast Fourier transform analysis of HR-TEM images yields diffraction patterns equivalent to SAED, facilitating identification of zone axes and measurement of interplanar angles.

3.4. EDX

EDX elemental mapping, performed in STEM mode, provides spatially resolved compositional information at the nanoscale, enabling visualization of core–shell architectures, elemental segregation, and interfacial composition gradients. In Pt-Pd-Au heterotrimers, multi-element EDX mapping confirmed the spatial segregation of Au, Pd, and Pt domains and the absence of significant interdiffusion (Figure 6) [21,35]. Quantitative EDX analysis, when properly calibrated and corrected for matrix effects, provides compositional stoichiometry that can be correlated with bulk techniques (ICP-AES) to assess homogeneity. Line-scan EDX profiles across core–shell interfaces reveal the sharpness of compositional transitions, with abrupt changes indicative of well-defined interfaces and gradual transitions suggesting interdiffusion or alloying.

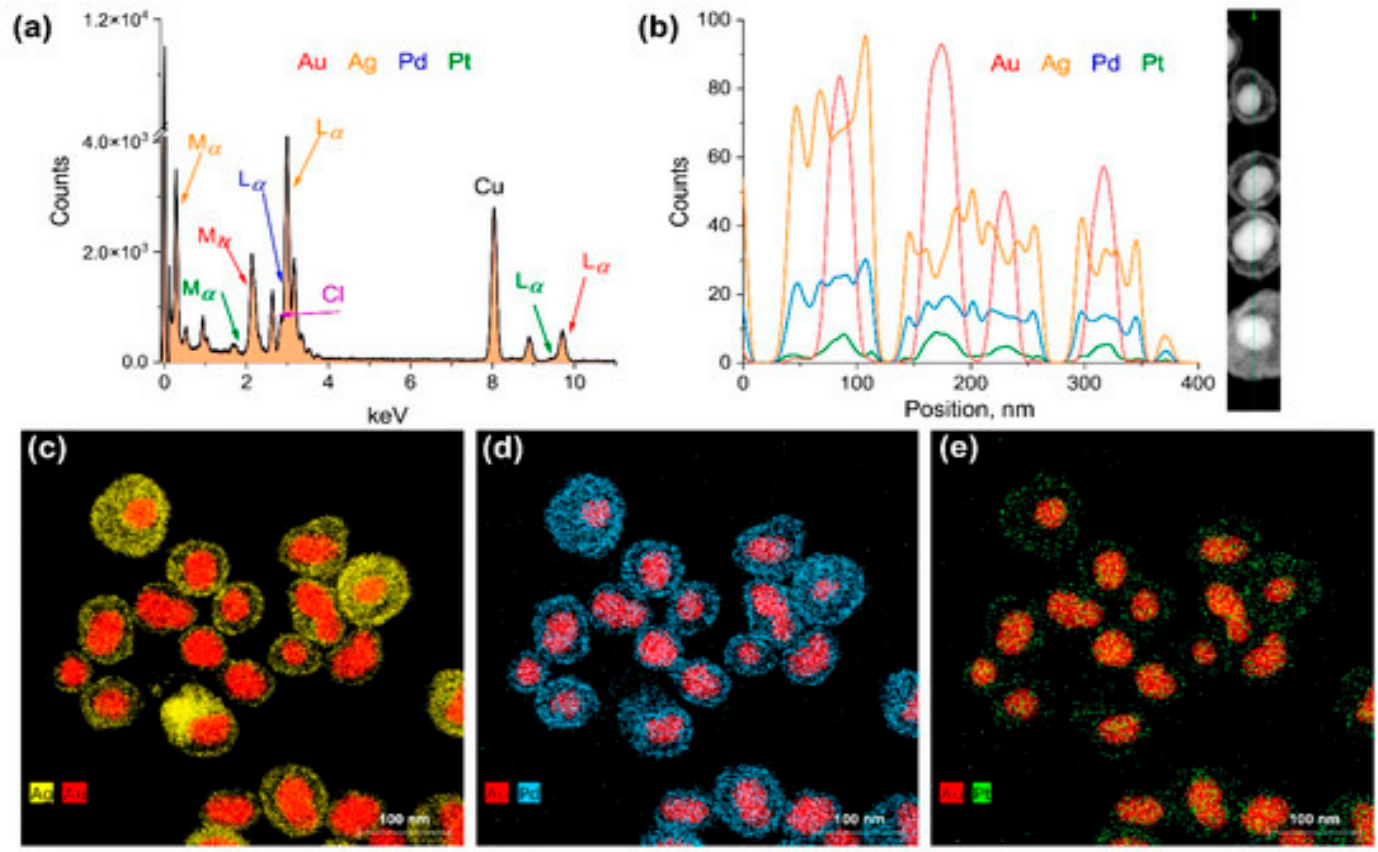


Figure 6. Compositional characterization of the multimetallic NPs. (**a**) EDX spectrum confirming the elemental composition (Au, Ag, Pd, Pt). (**b**) Cross-sectional EDX line profile displaying the relative distribution of elements. (**c**–**e**) Elemental maps of an individual nanoparticle: (**c**) Au/Ag overlay, (**d**) Au/Pd overlay, and (**e**) Au/Pt overlay. Reproduced from [35].

3.5. BET: Surface Area and Porosity Analysis

BET analysis of nitrogen adsorption–desorption isotherms provides quantitative measures of specific surface area, pore volume, and pore size distribution, which are critical for understanding catalytic activity and reactant accessibility. Sub-5 nm Au-Cu@SiO_2 catalysts exhibited bimodal porous structures with high surface areas, as determined by BET analysis, contributing to their enhanced CO oxidation activity [25]. Pore size distributions, calculated via the Barrett-Joyner-Halenda method, distinguish microporous (<2 nm), mesoporous (2 to 50 nm), and macroporous (>50 nm) regimes [41], with mesoporous structures generally preferred for catalytic applications due to their balance of surface area and diffusion accessibility.

Pore structure and active-site accessibility are as important as total surface area in determining catalytic performance. Micropores (<2 nm) contribute disproportionately to measured BET surface area but can impose diffusional restrictions on dye molecules and reactants, whereas mesopores (2 to 50 nm) offer a favorable compromise between surface area and mass-transport accessibility [41]. This distinction is particularly relevant for heterostructured catalysts, where the active sites are located at metal–oxide interfaces that must remain reachable by reactants and light. For example, the bimodal porous structure of sub-5 nm Au–Cu@SiO_2 catalysts, confirmed by BET analysis, combined high surface area with accessible diffusion pathways, contributing to their enhanced CO oxidation activity [25]. Similarly, mesoporous SiO_2 shells with pore sizes in the 2 to 10 nm range provide an optimal balance between reactant accessibility to the encapsulated metal surface and structural stabilization against sintering [25]. In contrast, aggregation or pore blockage (common in high-order heterostructures) can bury interfacial active sites and reduce effective surface area even when BET values appear favorable, which may partly explain the non-proportional gains often observed for tri- and tetra-metallic systems. Thus, pore architecture and interfacial site accessibility, rather than surface area alone, should be reported and optimized when benchmarking heterostructured catalysts.

3.6. Optical and Electronic Characterization

UV-Vis diffuse reflectance spectroscopy enables determination of optical band gaps via Tauc plot analysis, providing insight into electronic structure and the influence of heterostructure formation on band alignment. ZnO@Fe_3O_4 composites exhibited band gaps of ~2.0 to 2.1 eV, intermediate between the band gaps of pure ZnO (~3.2 eV) and Fe_3O_4 (~0.1 eV), indicating electronic coupling between the 2 oxide phases [22]. Plasmonic absorption bands in noble metal-containing heterostructures (e.g., Au, Ag) provide evidence of metallic nanoparticle formation and can be used to estimate particle size and shape via Mie theory. Photoelectrochemical measurements, including photocurrent response, Mott-Schottky analysis, and EIS, provide direct evidence of charge transfer efficiency and interfacial electronic coupling. In Pd/$Bi_2O_2CO_3$–Bi_2MoO_6–CuO quaternary heterojunctions, enhanced photocurrent and reduced charge transfer resistance (as measured by EIS) confirmed improved charge separation and interfacial conductivity relative to single-component oxides [36].

3.7. Advanced Spectroscopic Techniques

X-ray absorption spectroscopy (XAS), including X-ray absorption near-edge structure (XANES) and extended X-ray absorption fine structure (EXAFS), provides element-specific information on oxidation state, local coordination environment, and bond distances, making it invaluable for characterizing metal-oxide interfaces and detecting subtle structural changes. EXAFS analysis of Ag/Fe-oxide heterostructures revealed interfacial bonding configurations and coordination numbers that were not accessible via XRD or HR-TEM [42]. FTIR and Raman spectroscopy probe vibrational modes, enabling

identification of surface functional groups, adsorbed species, and metal-oxygen bonding. In Pd/$Bi_2O_2CO_3$–Bi_2MoO_6–CuO heterojunctions, FTIR confirmed the presence of carbonate and molybdate groups, validating the ternary oxide composition [36].

3.8. Summary: Synthesis-Structure-Property Relationships

The synthesis of high-quality metal-metal oxide heterostructures for biological and dye degradation applications demands a holistic approach that integrates rational selection of synthesis methods, precise control of reaction parameters, and comprehensive characterization to validate interfacial architecture (Table 1). The progression from monometallic oxides through bimetallic, trimetallic, and tetrametallic heterostructures is accompanied by escalating synthetic complexity, with each additional component introducing new challenges in phase control, stoichiometry, and interfacial integrity (Table 2). The critical insight emerging from this review is that true synergy—demonstrated as enhanced catalytic activity, improved charge transfer, and cooperative reactivity—arises not from the mere presence of multiple elements, but from the establishment of intimate, well-defined interfaces with controlled crystallographic orientation and minimal defect density. Synthesis strategies must therefore be evaluated and optimized not only for their ability to incorporate multiple components, but more fundamentally for their capacity to engineer high-quality interfaces that serve as the focus of synergistic interactions. Future advances in multimetallic heterostructure synthesis will likely leverage emerging techniques such as atomic layer deposition, microfluidic synthesis, and machine learning-guided optimization to achieve unprecedented control over interfacial architecture, enabling rational design of next-generation catalysts for environmental remediation and biomedical applications.

Table 1. Comprehensive comparison of bi-, tri-, and tetra-heterostructures: synthesis methods, conditions, and physicochemical properties.

Heterostructure	Heterojunction System and Components	Synthesis Method	Synthesis Conditions	Crystal Structure/Phase	Morphology	Particle/Crystallite Size	Band Gap (eV)	Surface Area (m^2/g)	Ref.
Bi-component heterostructures									
ABO (Au-Bi_2O_3)	Au-Bi_2O_3 Schottky heterojunction with PEG coating	Coprecipitation + polymer modification	Au NRs synthesis, Bi_2O_3-Au coprecipitation (RT), mPEG-SH coating	Bi_2O_3 (JCPDS 27-0052), Au (JCPDS 04-0784)	Floral nanostructure	Au nanorods: 11 nm diameter × 44 nm; ABO: ~550 nm (DLS)	3.45 (ABO), 3.75 (BO)	-	[43]
TiO_2/Au	TiO_2 nanowires decorated with Au NPs	Pulsed laser ablation in liquid	1064 nm laser, 50 mJ, 10 ns, 10 Hz, 5 min ablation + 355 nm post-irradiation	Anatase TiO_2 (JCPDS 89-4921), fcc Au	Nanowires with spherical Au NPs	TiO_2 nanowires: 55 nm; TiO_2/Au: 34 nm	3.4 (TiO_2), 3.24 (TiO_2/Au)	-	[44]
BiCuOS nanoflowers	CuS-Bi_2O_3 nanoarrays	Hydrothermal with oleylamine/sodium citrate	180 °C, 12 h	CuS, Bi_2O_3 nanoplates	Flower-like 3D superstructure with vertical nanoplates	800 ± 100 nm; nanoplates: 150 ± 50 nm length, 25 nm thick	0.6 (indirect)	-	[45]

ZnO-Ag	ZnO-Ag bimetallic nanocomposite	Pulsed laser ablation in water	355 nm laser, 190 mJ, 10 Hz, 30 min + 60 min post-irradiation	Hexagonal ZnO wurtzite, metallic Ag	Nanorods + nanosheets	ZnO: ~130 nm diameter × 240 nm; Ag: 30 nm; composite: 30 to 130 nm	3.4 (ZnO), 5.8 (ZnO-Ag)	-	[46]
Pd-Pt NPs	Pd-Pt bimetallic	Green synthesis (rosemary/ginseng extract)	Reflux at 100 °C, 3 to 6 h with PVP stabilization	fcc Pd and Pt phases	Cubic, spherical	22.2 nm; 54.1 nm (DLS)	-	-	[47]
Mn_3O_4-Ag_2S JNPs	Mn_3O_4-Ag_2S Janus NPs	Low-temperature reversed-phase microemulsion	RT, 24 h with TAA, PF127 coating	Mn_3O_4 (JCPDS 77-0435), Ag_2S (JCPDS 14-0072)	Janus (asymmetric)	Mn_3O_4: 9 nm; Ag_2S: 5 to 10 nm; MA-PF127: 58.8 nm	-	-	[48]
BOMO (Bi_2O_3/MoO3)	Bi_2O_3-MoO_3 composites	Hydrothermal + coprecipitation	220 °C, 18 h, calcination at 550 °C	Monoclinic Bi_2O_3, orthorhombic MoO_3	Sheets-like	-	2.41–2.48 (composites)	21.04 (Bi_2O_3), 48.5 (BOMO-5)	[49]
Bi_2SiO_5/$CuBi_2O_4$	Bi_2SiO_5-$CuBi_2O_4$ Z-scheme with oxygen vacancies	One-pot hydrothermal	190 °C, 12 h, pH 11	Orthorhombic Bi_2SiO_5, tetragonal $CuBi_2O_4$	Microrods + nanosheets	-	-	-	[50]
NiO/g-C_3N_4	Type-II/Z-scheme (NiO, g-C_3N_4)	Ultrasonic-assisted deposition	Ultrasonication, pH 9, 90 °C drying, 500 °C calcination	Hexagonal NiO, g-C_3N_4 nanosheets	NiO NPs dispersed on g-C_3N_4 sheets	~50 nm (TEM)	2.90 (for 10% NiO)	-	[51]
HMTA-ZnO/Ag	Plasmonic/Schottky (Ag, ZnO)	Solid-state dispersion	HMTA-assisted, 450 °C calcination	Hexagonal wurtzite ZnO, cubic Ag	Hexagonal prism-like ZnO with Ag nanospheres	50 ± 20 nm (average)	2.75	-	[52]
$MoSe_2$/$BiVO_4$ (BM)	Type-II ($MoSe_2$, $BiVO_4$)	Hydrothermal	200 °C ($BiVO_4$), 180 °C ($MoSe_2$)	Monoclinic $BiVO_4$, hexagonal $MoSe_2$	Fern-like $BiVO_4$ with $MoSe_2$ nanosheets	19.8 nm ($BiVO_4$), few-layer $MoSe_2$	2.5 ($BiVO_4$), 1.5 ($MoSe_2$)	-	[53]
p-n NiO-ZnO	p-n (p-NiO, n-ZnO)	Homogeneous precipitation	pH 11, 600 °C calcination	Rhombohedral NiO, hexagonal wurtzite ZnO	Cubic NiO on hexagonal ZnO particles	33.94 nm (ZnO)	-	-	[54]
NiO/CuO	p-p (NiO/CuO)	Co-precipitation	55 °C precipitation, 400 °C calcination	Monoclinic CuO, fcc NiO	Needle/snowflake	16.2 nm	3.8	117.8	[55]
B-ZnO/TiO_2	Heterojunction (B-doped ZnO, TiO_2)	Mechanochemical-calcination	500 °C calcination	Hexagonal ZnO, anatase TiO_2	Irregular spheroid (B-ZnO),	42.5 nm (composite)	2.89 (direct), 3.06 (indirect)	18.99	[56]

					spherical (composite)				
ZnO-Bi_2O_3	Type-II (n-ZnO, p-Bi_2O_3)	Co-precipitation	400 °C calcination	Hexagonal ZnO, tetragonal Bi_2O_3	Irregular microparticles/aggregates	29.6 ± 7.1 nm	3.13	-	[57]
α-Fe_2O_3/ZnTe	Type-II (α-Fe_2O_3, ZnTe)	Hydrothermal (2-step)	200 °C (Fe_2O_3), 120 °C (composite)	Rhombohedral α-Fe_2O_3, cubic ZnTe	Agglomerated spheres (Fe_2O_3), irregular spheres (ZnTe)	32.5 nm (Fe_2O_3), 40.4 nm (ZnTe)	2.13 (Fe_2O_3), 2.21 (ZnTe)	-	[58]
MnV_2O_6/$BiVO_4$	Heterojunction (MnV_2O_6, $BiVO_4$)	Hydrothermal	180 °C	Monoclinic $BiVO_4$, MnV_2O_6	Belt-like morphology	40.6 nm	1.95	77.35	[59]
SnO_2-decorated ZnO	Heterojunction (ZnO, SnO_2)	Green synthesis (*Olea europaea* extract)	550 °C calcination	Hexagonal ZnO, tetragonal SnO_2	Nanorods and spherical grains	6.45 nm (ZT20)	3.17 (ZT20)	25.3 (ZT20)	[60]
$Ni_{1-x}Mn_xWO_4$	Doped Metal Tungstate ($NiWO_4$, $MnWO_4$)	Hydrothermal	120 °C, 600 °C calcination	Monoclinic $NiWO_4$/$MnWO_4$	Monodispersed hexagonal crystals	26.84 nm	2.13	-	[61]
Mn_3O_4@ZnO	Heterojunction (Mn_3O_4, ZnO)	Sol–gel + Hydrothermal	95 °C hydrothermal	Hexagonal ZnO, tetragonal Mn_3O_4	ZnO nanorods/flower, thin sheets (hybrid)	-	-	-	[8]
$Mn_{0.5}Zn_{0.5}Fe_2O_4$/Fe_2O_3	Mixed oxide (ferrite, hematite)	Pechini Sol–gel	800 °C calcination	Cubic ferrite, hexagonal Fe_2O_3	Spherical shapes	80.6 nm	3.52, 4.20	62.7	[62]
(Co,Mn)(Co,Mn)$_2O_4$	Spinel (Co, Mn)	Sol–gel auto-combustion	750 °C calcination	Tetragonal spinel	Spherical, monodisperse	30 nm (XRD), 74 nm (SEM)	1.7	-	[63]
Fe_3O_4@MnO_2	Fe_3O_4-MnO_2 core–shell	Chemical coprecipitation	80 °C, N_2 atmosphere, RT overnight	Cubic Fe_3O_4 (JCPDS 19-0629), MnO_2 phases	Core–shell	TEM: 6.48 ± 1.65 nm; XRD: 7.24 nm	2.78	-	[64]
CMBNPs (Cu-Mn)	Cu-Mn bimetallic oxide	Biogenic (pumpkin seed extract)	90 °C reaction, 7000 rpm centrifugation	Tetragonal + orthorhombic phases	Spherical	TEM: 50 nm; SEM: 300 nm	-	-	[65]
CuO/TiO_2	CuO-TiO_2 nanocomposite	Ultrasonic processing	20 kHz, 1 h, drop casting at 120 °C	Monoclinic CuO, anatase + rutile TiO_2	Quasi-spherical	~20 nm	3.08 (CuO/TiO_2) vs. 3.28 (TiO_2)	-	[66]
CuTiNCs (CuO-TiO_2)	CuO-TiO_2 nanocomposite	Mycosynthesis (*Candida* sp.)	30 °C, 96 h, intracellular/extracellular	Monoclinic CuO, anatase TiO_2	Polygonal + spherical aggregates	15 to 75 nm	-	-	[67]

CuO/ZnO	p-n (CuO/ZnO)	Co-precipitation	55 °C precipitation, 400 °C calcination	Monoclinic CuO, hexagonal ZnO	Spherical/porous	18.9 nm	3.72	88.0	[55]
ZnO/NiO	p-n (ZnO/NiO)	Co-precipitation	55 °C precipitation, 400 °C calcination	fcc NiO, hexagonal ZnO	Spherical/porous	22.6 nm	3.69	79.3	[55]
CrZnO, RuZnO, Ba-ZnO	Cr, Ru, Ba-doped ZnO	Coprecipitation + pectinose	270 °C, 3 h stirring, 500 °C calcination	Hexagonal ZnO wurtzite	Oval, irregular	XRD: 21.22 to 34.38 nm	-	-	[68]
ZnO-CuO-PEG	ZnO-CuO with PEG coating	Hydrothermal + coprecipitation	180 °C, 15 h; PEG coating	Hexagonal ZnO, monoclinic CuO	Flower-like + nanorods	ZnO crystallite: 48.5 nm; CuO crystallite: 36.2 to 49.2 nm	-	-	[69]
Tri-component heterostructures									
Pt@CeO_2@MnO_2	Pt core/CeO_2 interlayer/MnO_2 shell	Sequential synthesis + PEG stabilization	$Ce(NO_3)_3$ in CTAB at 60 °C; $Mn(OAc)_2$ with PEG at RT	Cubic CeO_2 (JCPDS 00-043-1002), fcc Pt, amorphous MnO_2	Core–shell nanostructures	Pt: 48 ± 2 nm; CeO_2 shell: 10 ± 2 nm; overall: ~115 nm	-	-	[70]
B@FMZ/MTX	Bi_2S_3 nanorods core + Fe/Mn-doped ZIF-8 shell with MTX	Hydrothermal (Bi_2S_3) + ion deposition (ZIF-8)	Bi_2S_3: 180 °C, 4 h; ZIF-8: RT, 24 h; MTX loading overnight	Orthorhombic Bi_2S_3 (JCPDS 23-0677), ZIF-8	Core–shell with dodecahedral shell	Bi_2S_3 nanorods: 17.4 nm diameter; B@FMZ: 259 nm (DLS)	-	250	[71]
PIBD (PLGA@IR780-Bi-DTPA)	Bi-DTPA + IR780 in PLGA matrix	Double emulsification	Ultrasonic processor, 54 W, ice bath, 3 min	Amorphous	Spherical core–shell	250.7 ± 8.05 nm	-	-	[72]
ZnO/ZrO_2/rGO	ZnO-ZrO_2 on rGO sheets	Green synthesis (ginger extract)	70 °C, 3 h stirring, 120 °C drying	Hexagonal ZnO wurtzite, monoclinic + tetragonal ZrO_2	Spherical particles on rGO sheets	XRD: 13 nm; TEM: 12 nm; DLS: 149 nm	-	-	[73]
$BiVO_4$/Fe_3O_4@PDA	$BiVO_4$ + Fe_3O_4 NPs in PDA shell	Oil-in-water microemulsion + self-assembly	Toluene/water/SDS emulsion, 60 °C evaporation	Monoclinic $BiVO_4$, cubic Fe_3O_4	Spherical superparticles	$BiVO_4$: 7.12 nm; Fe_3O_4: 5.49 nm; SPs: 81.20 nm	-	-	[74]
Gd-Ti-FA-TA NPs	Gd-Ti-tannic acid-folate coordination polymer	Metal–organic coordination + PVP	RT stirring, 90 °C aging, 12 h	Amorphous	Spherical	224.7 ± 5.8 nm (DLS); 211.1 ± 14.3 nm (TEM)	2.0 (vs. TiO_2 3.3)	-	[75]
CuO/MgO/ZnO	Ternary mixed oxide	Green synthesis (*Costus pictus* extract)	80 °C stirring, 450 °C calcination (2 h)	Hexagonal ZnO, cubic MgO, monoclinic CuO	Flower-like	TEM: ~50 nm; XRD: 28.79 nm	-	87.742	[76]
TiO_2/Bi_2MoO_6/Ag	Ag-modified TiO_2/Bi_2MoO_6 Z-scheme	Hydrothermal +	TiO_2 NRs: 150 °C, 12 h; Bi_2MoO_6: 160	Rutile TiO_2, orthorhombic	Nanorods with	TiO_2 nanorods: ~200 nm	2.06	-	[77]

		photo-deposition	°C, 16 h; Ag: photo-deposition 30 to 60 min	Bi_2MoO_6, metallic Ag	nanosheets + Ag NPs	diameter; Ag: 3 to 5 nm			
MnNCs (MnO_2/CuO/NiO)	MnO_2-CuO-NiO nanocomposites	Solid combustion	300 °C, 30 min, urea + succinic acid fuel	Cubic MnO_2, cubic CuO, cubic NiO	Dumbbell, spherical, hexagonal	XRD: 15 to 20 nm; SEM: 61 to 131 nm	3.21 (MnO_2), 2.52 (MnNCs-2)	-	[78]
Dy_2O_3/ZnO-Au	Dy_2O_3-ZnO-Au ternary	Sonochemical + green (pomegranate extract)	60 W, 30 min, 600 °C calcination	Cubic Dy_2O_3, hexagonal ZnO, fcc Au	Spherical	85 to 90 nm	2.98	-	[79]
ZTB/CMCS	ZnO-TiO_2-Bi_2WO_6 in carboxymethyl chitosan	Hydrothermal + surface deposition	ZnO: 80 °C ultrasound; ZTB: 180 °C, 12 h; CMCS film: 50 °C drying	Hexagonal ZnO, anatase TiO_2, orthorhombic Bi_2WO_6	Microspheres with nanosheets	ZTB: 5100 ± 100 nm; ZnO: 5 ± 1 nm; TiO_2: 8 ± 2 nm	2.70	56.34	[80]
BWTO (Bi_2WO_6/TiO_2)	Bi_2WO_6/TiO_2 Z-scheme	In situ hydrothermal	240 °C (TiO_2), 160 °C (Bi_2WO_6), 12 to 24 h	Anatase TiO_2, orthorhombic Bi_2WO_6	2D nanosheets on TiO_2	TiO_2 nanosheets: 10 nm thick	3.30 (TiO_2), 2.90 (Bi_2WO_6), 3.17 (50BWTO)	22.30 (50BWTO)	[81]
Azl-MACO (Ag-Mo/CuO)	Ag, Mo-doped CuO with *Azadirachta indica* extract	Green biosynthesis	80 °C, pH 10, 2 h stirring, 500 °C calcination	Monoclinic CuO	Nanoflakes	XRD: 11.23 nm (Azl-MACO)	2.22	-	[82]
Ag_2O/CuO/ZnO	Ag_2O-CuO-ZnO ternary	Green synthesis (*Croton macrostachyus*)	45 to 60 °C stirring, calcination at 350 to 600 °C	Hexagonal ZnO, monoclinic CuO, cubic Ag_2O	Spherical, nanoflowers	XRD: 2.35 to 2.71 nm; TEM: 20 to 100 nm	2.42 to 2.47	-	[83]
$NiFe_2O_4$@Hap-Ag	$NiFe_2O_4$ core/HAp shell/Ag NPs	Hydrothermal + chemical reduction	$NiFe_2O_4$: 160 °C, 24 h; HAp coating: 160 °C, 24 h; Ag: $NaBH_4$ reduction	Inverse spinel $NiFe_2O_4$, hexagonal HAp, fcc Ag	Spherical core + rod-like HAp shell	$NiFe_2O_4$: 27.35 nm; composite: 43.59 nm	1.86 ($NiFe_2O_4$), 2.48 (composite)	-	[84]
CuO@AgO/ZnO	CuO-AgO-ZnO nanocomposite	Sol–gel	185 °C, 12 h, 600 °C calcination	Hexagonal ZnO, monoclinic CuO, cubic AgO	Spherical	ZnO: 105.85 nm; composite: 85.03 nm	-	-	[85]
Ag/$Sr_6Bi_2O_9$-α-Bi_2O_3	Ag-$Sr_6Bi_2O_9$-α-Bi_2O_3 ternary	MOF-derived (Bi-TMA) + photoreduction	Bi-MOF: 120 °C, 12 h; calcination: 600 °C, 5 h; Ag: photodeposition	Rhombohedral $Sr_6Bi_2O_9$, monoclinic α-Bi_2O_3, fcc Ag	Cuboidal rods + nanosheets + Ag nanodots	Ag nanodots: 3 to 5 nm	2.66 (Bi_2O_3), 2.97 ($Sr_6Bi_2O_9$)	91.8 (SBO-BO)	[86]

Bi_2MoO_6/Bi_5O_7I	Bi_2MoO_6-Bi_5O_7I Z-scheme	In situ solvothermal	160 °C, 4 to 10 h	Orthorhombic Bi_2MoO_6, orthorhombic Bi_5O_7I	Microrods + nanosheets	Bi_5O_7I rods: 200 to 800 nm × 2 to 8 µm; Bi_2MoO_6 nanosheets: 300 nm	2.77 (Bi_5O_7I), 2.67 (Bi_2MoO_6)	-	[87]
ZnO-NiO-CuO	ZnO-NiO-CuO ternary heterojunction	Hydrothermal	150 °C, 12 h, annealing 400 to 800 °C	Hexagonal ZnO, cubic NiO, monoclinic CuO	Mixed rod + spherical	XRD: 21 to 34 nm; SEM: increasing with annealing	2.55 to 2.92	-	[16]
CuO-ZnO-Co_3O_4	CuO-ZnO-Co_3O_4 ternary	Coprecipitation	RT, pH 7, 500 °C calcination	Monoclinic CuO, hexagonal ZnO, cubic Co_3O_4	Spherical	XRD: 13.6 to 26.73 nm; TEM: 18.1 nm	1.3	-	[88]
ZnO-Ag-MWCNTs	ZnO-Ag on MWCNTs	Impregnation-calcination	400 °C, 60 min	Hexagonal ZnO, fcc Ag, graphitic MWCNTs	Nanorods + NPs on CNTs	ZnO crystallite: 21.4 to 38.6 nm; Ag crystallite: 60.2 to 72.3 nm	-	-	[89]
ZMC (ZnO-MgO-CuO)	ZnO-MgO-CuO trimetallic	Green synthesis (*Artemisia abyssinica*)	70 °C, 1 h, 400 °C annealing	Hexagonal ZnO, cubic MgO, monoclinic CuO	Spherical, flower-like aggregates	XRD: 14.67 nm; TEM: 15.13 nm	-	-	[90]
$ZnFe_2O_4$@ZnO@CuO (Z3)	Fe^{2+}-doped $ZnFe_2O_4$ core/ZnO shell/CuO surface	Microwave-assisted solvothermal + reflux	200 °C, 1h (core); reflux (shell); 80 °C drying	$ZnFe_2O_4$ spinel, hexagonal ZnO, monoclinic CuO	Spheres (core–shell) + irregular NPs	Spheres: 113 nm; CuO: 55 nm	2.83 (Z3)	39 (Z3)	[91]
TiO_2/ZnO/chitosan	TiO_2-ZnO-chitosan ternary	Sol–gel + calcination	400 °C calcination (3 h)	Anatase TiO_2 (JCPDS 01-084-1286), hexagonal ZnO	Rough, cracked, porous	Crystallite: 13.92 to 17.82 nm	2.83 to 3.17	20.2 to 46.2	[92]
$Co_3O_4/ZnFe_2O_4$	Co_3O_4-$ZnFe_2O_4$ nanocomposite	Hydrothermal + mechanical grinding	CO: 200 °C, 12 h; ZFO: 180 °C, 24 h; 300 °C calcination	Cubic spinel Co3O4 (JCPDS 42-1467), cubic spinel $ZnFe_2O_4$ (JCPDS 22-1012)	Spherical NPs with agglomeration	CO: 19 nm; ZFO: 18 nm; composite: 15 to 20 nm	2.02 to 2.32	40.82 (0.8CO/0.2ZFO)	[93]
$ZnCdS/MoO_3$	ZnCdS-MoO_3 Z-scheme	Precipitation + calcination	ZnCdS: 180 °C, 24 h hydrothermal; MoO_3: 500 °C, 4 h calcination	Cubic ZnCdS, orthorhombic MoO_3 (PDF#35-609)	Spherical ZnCdS on polygonal MoO_3 nanosheets	-	2.19 (composite)	-	[94]

ZGF (ZnO/graphene/Fe_2O_3)	ZnO-graphene-Fe_2O_3 ternary	Solvothermal + annealing	80 to 90 °C, 600 °C annealing, 1 h	Hexagonal ZnO (JCPDS 36-1451), hexagonal α-Fe_2O_3 (JCPDS 33-0664)	Coral-like rough surface	Fe_2O_3: 16 to 28 nm; ZnO: 18 to 67 nm; graphene: 125 to 356 nm length	2.18	-	[95]
Ag_2CrO_4/Bi_2O_3-KBi_6O_9Br	Double Z-scheme (Ag_2CrO_4, Bi_2O_3, KBi_6O_9Br)	Microwave-assisted combustion-precipitation	Microwave combustion, 250 to 320 °C calcination	Monoclinic Bi_2O_3, cubic KBi_6O_9Br, orthorhombic Ag_2CrO_4	Bi_2O_3 needles, Ag_2CrO_4 spheres on surface	Ag_2CrO_4 NPs < 1 μm, Bi_2O_3 needles	2.10, 1.70	7.33	[96]
Ag/CeO_2/ZnO	Plasmonic/Defect-induced (Ag, CeO_2, ZnO)	Thermal decomposition	350 °C calcination	Hexagonal ZnO, cubic Ag, cubic CeO_2	ZnO nanorods with Ag and CeO_2 NPs	100 to 150 nm length (ZnO rods)	2.66	39.2	[97]
$CuCoO_2/SnO_2$	p-n/S-scheme (p-$CuCoO_2$, n-SnO_2)	Hydrothermal + Electrospinning + Drop-casting	120 °C hydrothermal, 500 °C calcination, 300 °C annealing	Rhombohedral $CuCoO_2$, rutile SnO_2	SnO_2 nanofibers decorated with $CuCoO_2$ NPs	52 nm ($CuCoO_2$), 25 to 50 nm (SnO_2 grains)	1.41 ($CuCoO_2$), 3.60 (SnO_2), 3.21 (comp)	29.0	[98]
AM-Ag/CuO/ZnO NC	Multi-material (Ag, CuO, ZnO)	Microwave-assisted green synthesis	Microwave irradiation, 300 to 400 °C calcination	FCC Ag, monoclinic CuO, wurtzite ZnO	Spherical to oval, mixed morphology	8 nm (XRD), 10.2 nm (TEM)	1.91	-	[99]
$CuCo_{0.5}Ti_{0.5}O_2$	Delafossite-type ($CuCo_{0.5}Ti_{0.5}O_2$)	Chemical method with PVA	pH 10, 400 °C calcination	Rhombohedral (3R) and hexagonal (2H) delafossite	Cu/Co NPs embedded in TiO_2 matrix	-	2.56	30.72	[100]
Cu_2O/ZnO/Ag_3PO_4	p-n-n (p-Cu_2O, n-ZnO, n-Ag_3PO_4)	Co-precipitation	300 to 400 °C calcination under nitrogen	Cubic Cu_2O, hexagonal ZnO, cubic Ag_3PO_4	Rod-like ZnO with Cu_2O and Ag_3PO_4 particles	26 to 43 nm	2.15 (for 15:75:10)	11.4	[101]
TiO_2/Fe_3O_4/BiOI	n-p (n-TiO_2, p-BiOI) with magnetic Fe_3O_4	Refluxing	96 °C reflux, 65 °C drying	Anatase/rutile TiO2, FCC Fe_3O_4, tetragonal BiOI	Spherical particles (TiO_2/Fe_3O_4/BiOI)	-	3.20 (TiO_2), 1.76 (BiOI)	30.4	[102]
Fe-Mo LDH/ZnO	Heterojunction (Fe-Mo LDH, ZnO)	Hydrothermal (2-step)	90 °C (ZnO), 90 °C (LDH/ZnO)	Hexagonal ZnO, Fe-Mo LDH	Flower-like LDH on ZnO nanorods	33.9 nm (ZnO)	1.91	27.99	[103]
Ag-$AgVO_3/Zn_{0.5}Mn_{0.5}Fe_2O_4$	Z-scheme/Plasmonic (Ag-$AgVO_3$,	Hydrothermal + Co-precipitation	18 °C ($AgVO_3$), 60 °C (composite)	Tetragonal Ag/$AgVO_3$, ferrite	$AgVO_3$ nanorods grafted with ferrite NPs	20 to 45 nm (composite)	1.5	5.5	[104]

	$Zn_{0.5}Mn0.5Fe_2O_4$)								
Fe/Cu/Ag	Trimetallic (Fe, Cu, Ag)	$NaBH_4$ reduction	$NaBH_4$ reduction, 25 °C drying	BCC Fe_0, cubic Ag, cubic Cu	Spherical, chain-like agglomerates (core–shell)	11.4 nm (XRD), 60 to 90 nm (TEM)	-	104.4	[15]
Mn/g-C_3N_4/ZnO (Mn/GZ)	Heterojunction (Mn-doped ZnO, g-C_3N_4)	Co-precipitation	560 °C calcination	Hexagonal ZnO, g-C_3N_4	ZnO NPs integrated with g-C_3N_4 sheets	10 to 15 nm (TEM)	1.9 (Mn/50GZ)	-	[105]
CuO/ZnO/CQDs@PAN	p-n + Carbon QDs (CuO, ZnO, CQDs on PAN)	Electrospinning + Hydrothermal	150 °C heat treat, 150 °C hydrothermal	Monoclinic CuO, hexagonal ZnO, graphite CQDs	Nanosheets with CQDs on fiber surface	CQDs ~2 to 5 nm	-	-	[106]
Cu_4O_3/ZrO_2/TiO_2	Multi-oxide heterojunction (Cu_4O_3, ZrO_2, TiO_2)	Hydrothermal	140 °C hydrothermal, 350 °C calcination	Tetragonal Cu_4O_3, monoclinic ZrO_2, rutile TiO_2	Nanospheres in porous matrix	19 ± 1 nm	2.91	-	[107]
Fe-doped ZnO/SnS	p-n (n-ZnO, p-SnS) with Fe-dopant	Hydrothermal	220 °C	Hexagonal ZnO, orthorhombic SnS	Nanorods (ZnO) with nanoparticle clouds (SnS/Fe)	6.2 nm (ZSF3)	2.28 (ZSF3)	-	[108]
CuO/Mn_3O_4/CeO_2 (CMCu)	Type-II (CuO, Mn_3O_4, CeO_2)	Hydrothermal	180 °C, 400 °C calcination	Monoclinic CuO, tetragonal Mn_3O_4, cubic CeO_2	Interacting NPs	5.69 nm (XRD), 24.8 nm (TEM)	2.44	-	[109]
NiO/Ag/TiO_2	p-n + Schottky (p-NiO, n-TiO_2, Ag)	Co-precipitation deposition	$NaBH_4$ reduction, 600 °C annealing	Rutile TiO_2	Irregular spherical TiO_2 with Ag/NiO NPs	150 to 200 nm (TiO_2), <3 nm (Ag)	2.50	14.3	[110]
α-Fe_2O_3-CeO_2@Au	Type-II + Plasmonic (α-Fe_2O_3, CeO_2, Au)	Hydrothermal + Green Au deposition	180 °C hydrothermal, 500 °C calcination	Rhombohedral α-Fe_2O_3, cubic CeO_2, FCC Au	Coral-like aggregates (NC), decorated with Au	6.9 nm (Fe_2O_3), 9.4 nm (CeO_2), 36.4 nm (NC@Au)	1.78	-	[111]
Ti/Co/Mn oxides with 5% CuO	TiO2-CuO(5%)@Co_3O_4 and TiO_2-CuO(5%)@Mn_2O_3	Sol–gel	RT hydrolysis, 140 °C drying, 600 °C calcination (2 h)	Tetragonal rutile TiO_2, monoclinic CuO, cubic Co_3O_4, cubic Mn_2O_3	Non-uniform microparticles, spherical, cylindrical	100 to 500 nm (Co_3O_4 composite); 100 to 300 nm (Mn_2O_3 composite)	2.56, 2.65	4.52 to 9.43	[112]
Fe/Al/La trimetallic oxide (FAL)	Fe-Al-La trimetallic oxide	Solution combustion	Urea as fuel, calcination at 700 °C, 4 h	Trigonal	Porous, wedge-shaped pores	Crystallite: 10 nm	1.97	50.15	[17]

Ag-Li-ZnO (ALZO)	Ag-Li co-doped ZnO	Sol–gel	60 to 80 °C reflux, 600 °C calcination (4 h)	Hexagonal ZnO wurtzite (JCPDS 36-1415), cubic Ag_2O	Needle-like, rod-shaped agglomerations	XRD: 28.71 nm (ALZO)	2.82 (ALZO)	14.53 (ALZO)	[113]
Cu/Cr/Ni trimetallic	Cu-Cr-Ni trimetallic oxide	Green synthesis (*Eryngium campestre* + *Froriepia subpinnata*)	20 to 70 °C, 3 to 296 min optimization	CuO, Cr_2O_3, NiO phases	Nano-plate	Crystallite: 6.95 to 11.9 nm; Plate thickness: 10.96 to 18.73 nm	-	-	[114]
Tetra-component heterostructures									
BBCD (Bi-Cu-S/DATS@BSA)	Cu-Bi sulfide nanodots + DATS in BSA matrix	In situ assembly at RT	Bi^{3+}/Cu^{2+} chelated BSA + DATS + TAA, aging	Poorly crystalline/amorphous Cu-Bi sulfide	Nanospheres with embedded nanodots	Spheres: 80 nm; nanodots: ~5 nm	-	-	[115]
$K_4Nb_6O_{17}$/α-Fe_2O_3/Fe_3N/g-C_3N_4	Quaternary: $K_4Nb_6O_{17}$, α-Fe_2O_3, Fe_3N, g-C_3N_4	One-step thermal pyrolysis	Precursors: Nb_2O_5, melamine ($C_3H_6N_6$), $K_3Fe(CN)_6$ (molar ratio 1:1:1.5). Temperature: Heated to 550 °C at 2 °C/min, held for 3 h, then cooled at 2 °C/min.	Tetragonal $K_4Nb_6O_{17}$, Rhombohedral α-Fe_2O_3, Hexagonal Fe_3N, Hexagonal g-C_3N_4	Nanoflake structure with layered sheets	A few hundred nm (from SEM)	2.75	-	[116]
Fe-Ce-Co@biochar	Multi-metal on biochar (Fe, Ce, Co, biochar)	Pyrolysis + Reduction	550 °C pyrolysis (biochar), $NaBH_4$ reduction	Amorphous carbon, Fe, Ce, Co NPs	NPs dispersed on biochar matrix	~20 nm (TEM)	2.38	33.6	[117]
Zn-Cd-Mo-S (ZCM_5S)	Quaternary metal sulfide: ZnS/CdS/MoS_2 double heterojunction	One-step mild hydrothermal self-assembly	90 °C, 270 min; CAM, VC, HT, HDTMA, TAA as ligands/templates	Cubic zinc blende CdS + sphalerite ZnS + MoS_2 (low content)	Mesoporous nanospheres	~100 nm diameter	2.53	113	[118]
Ag_3VO_4/$Zn_3(VO_4)_2$/$Zn_2V_2O_7$/ZnO (50% Ag_3VO_4/Zn-V-O)	Quaternary heterojunction: Ag_3VO_4 + $Zn_3(VO_4)_2$ + $Zn_2V_2O_7$ + ZnO	Microwave hydrothermal + calcination + in situ precipitation	Step 1: 160 °C, 30 min (microwave); Step 2: 700 °C, 2 h (calcination); Step 3: RT precipitation	Monoclinic Ag_3VO_4 + orthorhombic $Zn_3(VO_4)_2$ + monoclinic $Zn_2V_2O_7$ + hexagonal ZnO	Nanosheets coated with NPs	Ag_3VO4 NPs: 80 to 250 nm; Zn-V-O nanosheets: <350 nm length	2.48	-	[119]
ZnO/SnO_2/CeO_2/CuO (ZSCC)	Quaternary metal oxide: ZnO + SnO_2 + CeO_2 + CuO	Shallow chemical precipitation with	pH 9, stirring 4 h at RT, dried at 80 °C/3 h, calcined at 600 °C/4 h	Hexagonal ZnO + tetragonal SnO_2 + cubic CeO_2 +	Mixed morphologies: rice-like ZnO, rod-like SnO_2,	ZnO: 65 nm; SnO_2 rods: 80 nm length, 25 nm diam.;	2.54 (composite)	-	[120]

		CTAB surfactant		monoclinic CuO	hexagonal CeO_2, spherical CuO	TEM: 30 to 90 nm			
Ag/BiOBr@Bi_2MoO_6/ZnO/g-C_3N_4	Quaternary heterojunction: Ag (plasmonic) + BiOBr + Bi_2MoO_6 + ZnO + g-C_3N_4	Multi-step: calcination + solvothermal + hydrothermal + photo-assisted deposition	ZnO/g-C_3N_4: 550 °C/2 h; BiOBr@Bi_2MoO_6: 160 °C/8 to 12 h; Composite: 160 °C/20 h; Ag deposition: 2 h light irradiation	Hexagonal ZnO + tetragonal BiOBr + orthorhombic Bi_2MoO_6 + g-C_3N_4 + metallic Ag	Flower-like microspheres (2–3 μm) with embedded BiOBr nanosheets, ZnO particles, Ag NPs dispersed	Ag NPs: 4 to 5 nm (TEM)	2.64	75.71	[121]
CeO_2/Co_3O_4/Ag/Ag_3PO_4	Quaternary S-scheme: CeO_2/Co_3O_4 nanoflowers + Ag + Ag_3PO_4	Electrospinning + calcination + precipitation	Electrospinning: 17 to 18 kV, 14 cm distance, 0.3 mL/h; Calcination: 550 °C/3 h; Precipitation: RT under light	Cubic CeO_2 + cubic Co_3O_4 + cubic Ag_3PO_4 + metallic Ag	Nanoflowers decorated with Ag_3PO_4 NPs	Nanoflowers: nanometer diameter; Ag_3PO_4 NPs distributed on surface	2.1	-	[122]
ZnO-PbO-CdO-CuO (ZPCC)	Quaternary metal oxide: ZnO + PbO + CdO + CuO	One-pot chemical method with PVP	80 °C, 2 h stirring; NaOH added; acetic acid for growth control; dried 120 °C/2 h	Hexagonal ZnO + tetragonal PbO + cubic CdO + monoclinic CuO	Tiny nanospheres composed of nanorods; heterogeneous morphology	XRD crystallite: 22.3 nm; TEM: mixed spheres and rods	2.30	-	[123]
Au-Ti-Mg-Al-Cu HEMDMHs	High-entropy/Mixed-dimensional (Au, $Ti_3C_2T_x$ MXene, Mg-Al-Cu LDH)	In situ growth on MXene + In situ AuNC synthesis	200 °C (LDH/MXene), 280 °C calcination	Mg-Al-Cu(O) LDH, $Ti_3C_2T_x$ MXene	LDH nanosheets on MXene, with AuNCs (<3 nm)	AuNCs 2.64 ± 1.04 nm	-	135.4	[124]
Zr Al Fe Co Ni LDH (layered double hydroxide)	Quinary LDH (Zr-Al-Fe-Co-Ni)	Bottom-up co-precipitation	Molar ratio Zr:Al:Fe:Co:Ni = 0.1:0.5:0.4:2:2; metal salt solutions in distilled water; 2 M NaOH added dropwise with stirring until pH 10; suspension stirred overnight at RT; centrifuged and washed with distilled water until pH 7; precipitate dried at 50 °C for 24 h	LDH structure with typical LDH diffraction peaks at 11.3°, 22.8°, 34.3°, 39.5°, 46.2°, and 61° corresponding to 003, 006, 012, 015, 018, and 110 planes	Aggregated, layered structure; interlayer distance 7.81 Å	4.2 nm (XRD); ~300 nm (DLS)	-	45.4	[125]

Table 2. Comprehensive comparison of synthesis strategies for mono-, bi-, tri-, and tetra-metallic heterostructures: key characteristics, advantages, and limitations.

Heterostructure	Synthesis Strategy	Typical Architecture	Key Characteristics/Control Parameters	Advantages	Limitations/Challenges	Ref.
Monometallic	Sol–gel and seeded growth	Core–shell NPs	Hydrolysis kinetics, precursor/core ratio, calcination temperature	Precise shell thickness control; intimate core–shell contact	High temp. can cause sintering; residual organics	[18,19]
	Hydrothermal/solvothermal	Crystalline NPs, nanorods	Temperature, pressure, solvent, surfactant, duration	High crystallinity; controlled morphology; reduced defects	Requires autoclave; batch-to-batch variability	[18,22]
	Co-precipitation	NPs	pH, supersaturation, stirring rate, capping agents	Simple, rapid, scalable, low-cost	Broad size distribution; aggregation; less crystalline	[23]
	Green synthesis	Surface-functionalized NPs	Plant extract type, concentration, temperature, pH	Eco-friendly, biocompatible, mild conditions	Batch variability; complex mechanism; less control over size/shape	[24]
Bimetallic	Photodeposition	Decorated NPs, core–shell	Light intensity, duration, precursor order, hole scavengers	Surfactant-free; intimate contact; selective deposition	Limited to photoactive supports; UV light required	[20,26]
	Chemical reduction/seed-mediated	Core–shell, decorated NPs	Reducing agent strength/concentration, pH, stabilizer (e.g., PVP)	Low-temp.; precise size control; epitaxial growth possible	Risk of galvanic replacement; homogeneous nucleation	[27]
	Impregnation and reverse micelle	Encapsulated clusters	Micelle size, precursor concentration, thermal treatment	Sub-5 nm clusters; prevents sintering; high dispersion	Multi-step; removal of surfactant; may require high-temperature calcination	[25]
	Electrochemical deposition	Decorated NPs on conductive oxides	Deposition potential, pulse duration, electrolyte composition	Ultrafast; no reducing agents; good for electrodes	Limited to conductive/semiconducting substrates	[28]
Trimetallic	Sequential deposition/mask-assisted	Heterotrimers (e.g., Pt-Pd-Au)	Masking material (e.g., SiO_2), etching, sequential reduction	Highest precision; spatially resolved domains; epitaxial interfaces	Highly complex, multi-step; difficult to scale; low yield	[21]
	Total-synthesis framework	Oligomers (e.g., M-Pt-Fe_3O_4)	Chemoselective reactions, ligand exchange, sequential assembly	Precise control over number, size, and arrangement of each component	Labor-intensive; requires careful optimization of each coupling step	[31]
	One-pot competitive reactions	Compositional gradients, alloys	Kinetic control (precursor reactivity, temperature), microfluidic reactors	Simpler, faster, potentially scalable	Less architectural precision; risk of alloying/phase mixing at interfaces	[32]
	Thermal decomposition and selective etching	Hollow, yolk-shell	Decomposition kinetics, etching agent selectivity	Unique hollow/yolk-shell architectures	Requires careful control to avoid structural collapse	[33]
Tetrametallic	Total-synthesis framework	Heterotetramers (e.g., M_xS-Au-Pt-Fe_3O_4)	Iterative chemoselective coupling	Ultimate architectural precision; multi-domain control	Extremely complex, multi-step; scalability is a major hurdle	[31]
	Multi-step deposition on ternary oxides	Quaternary heterojunctions	Solvothermal + chemical/photoreduction	More scalable than total synthesis; leverages pre-formed complex oxides	Less control over spatial arrangement of the 4th component	[36]
	High-entropy alloy/encapsulation	Multi-element alloys in shells	Rapid quenching, co-reduction, atomic layer deposition	Unique catalytic properties; high stability	Phase separation; achieving precise stoichiometry is difficult	[34]

	and chemical vapor deposition

4. Comparative Analysis: The 'Interface' in Biological Applications

The biological efficacy of metal–metal oxide heterostructured NPs fundamentally derives from the physicochemical properties of the interface—the nanoscale junction where distinct materials meet and create synergistic electronic, catalytic, and surface interactions [126]. This section examines how interface complexity evolves from monometallic systems through bimetallic, trimetallic, and tetrametallic architectures, and critically evaluates whether increasing compositional complexity translates to proportional therapeutic gains. By organizing the analysis according to mechanism of action (ROS generation, ion release kinetics, plasmonic enhancement, and magnetic targeting), we trace how interface engineering modulates antimicrobial and anticancer performance across the complexity spectrum.

The central hypothesis guiding this comparative analysis is that well-designed heterointerfaces create synergistic mechanisms unavailable to single-component systems: enhanced charge separation that amplifies ROS production, controlled ion reservoirs that sustain antimicrobial action, plasmonic hot e^- injection that extends photoactivation into the visible and near-infrared (NIR) spectrum, and multifunctional platforms that integrate imaging, targeting, and therapy. However, this hypothesis must be tested against quantitative evidence, asking whether the incremental efficacy gains justify the increased synthetic complexity, potential toxicity, and reproducibility challenges inherent in higher-order systems.

4.1. Antimicrobial Activity: Mechanisms Across Complexity Levels

4.1.1. Monometallic Mechanisms: Establishing the Baseline

Monometallic NPs and single metal oxides establish the mechanistic foundation upon which heterostructured systems build. Each material exhibits characteristic antimicrobial pathways that define its baseline efficacy and limitations.

- Ag (ion release and membrane disruption): Metallic Ag NPs exert antimicrobial effects through sustained Ag^+ ion release, which disrupts bacterial membrane integrity, interferes with respiratory chain enzymes, and binds to DNA, preventing replication [127]. The ion-release mechanism provides continuous antimicrobial action independent of light activation, making Ag a versatile component for combination systems. In Ag/ZnO heterostructures, the presence of Ag islands enhances both surface interaction with bacterial membranes and contributes additional ROS generation when photoactivated, demonstrating early evidence of interfacial synergy [127].
- Au (plasmonic photothermal effects and membrane interaction): Au NPs exhibit strong SPR in the visible to NIR spectrum, enabling photothermal conversion that raises local temperatures sufficient to disrupt bacterial membranes and denature proteins [128].
- Pt (catalytic ROS generation in composites): Pt NPs exhibit catalytic activity that enhances ROS generation when integrated into composite architectures [129].
- ZnO (photocatalytic ROS generation): ZnO operates primarily through photogenerated e^-–h^+ pair formation under UV irradiation, producing ROS including hydroxyl (•OH) radicals and superoxide anions ($\bullet O_2^-$) that oxidize bacterial membrane lipids and proteins [127,130,131]. The wide bandgap (~3.37 eV) restricts photoactivation to UV wavelengths, limiting applicability in deep-tissue or visible-light scenarios. ZnO also exhibits direct membrane interaction through electrostatic attraction to negatively charged bacterial surfaces, contributing to its antimicrobial action even in dark

conditions, though with substantially reduced efficacy compared to photoactivated states [127].

- TiO_2 (photocatalytic e^-–h^+ pair generation): TiO_2 shares ZnO's photocatalytic ROS generation mechanism via e^-–h^+ pair formation, with a similar UV-activation requirement (bandgap ~3.2 eV). When coupled with plasmonic noble metals such as Au or Pt, TiO_2 exhibits enhanced visible-light activity through surface plasmon resonance (SPR)-mediated hot e^- injection and reduced e^-–h^+ recombination [128,132]. This plasmonic enhancement represents a critical interface-driven improvement that extends TiO_2's utility beyond UV-only applications.
- Iron oxides (FeO, Fe_2O_3, Fe_3O_4; Fenton and Fenton-like ROS generation): Iron oxide NPs catalyze Fenton and Fenton-like reactions, converting hydrogen peroxide (H_2O_2) into highly reactive •OH radicals in the presence of Fe^{2+}/Fe^{3+} redox cycling [133]. Copper-doped ferrite systems (Cu@Fe) demonstrated exceptional antimicrobial potency with a MIC of 1 μg/mL against methicillin-resistant *Staphylococcus aureus* (MRSA), causing membrane rupture and intracellular ROS accumulation [133]. The magnetic properties of Fe_3O_4 enable magnetic separation and targeted delivery, adding functional versatility beyond antimicrobial action alone.
- CuO (Cu^{2+} ion release and oxidative stress): CuO NPs release Cu^{2+} ions that induce oxidative stress and membrane damage in bacterial cells [134].
- NiO (ROS generation and membrane interaction): NiO has been reported in mixed oxide composites for ROS generation and membrane interaction, though explicit monometallic MIC values and ion-release kinetics are not comprehensively documented in the available literature [135]. Its role in heterostructures appears supportive rather than dominant, contributing to overall oxidative stress mechanisms.

In summary, monometallic systems establish clear mechanistic pathways (ROS generation, ion release, photothermal effects) but face inherent limitations: UV-only activation for ZnO and TiO_2, high required doses for CuO, and single-mechanism action that bacteria can potentially resist through adaptive responses. These limitations motivate the design of heterostructured interfaces that combine multiple mechanisms and reduce individual material doses.

4.1.2. Bimetallic Dual-Action Synergy: Interface-Driven Enhancement

Bimetallic heterostructures introduce interfacial electronic interactions that create synergistic antimicrobial effects exceeding the sum of individual components. The interface serves as a site for enhanced charge separation, controlled ion release, and plasmonic coupling, enabling dual-mechanism action that reduces required doses and mitigates resistance.

- Ag–ZnO (enhanced e^-–h^+ separation and ion reservoir): Ag–ZnO represents one of the most extensively studied bimetallic antimicrobial systems, with the Ag/ZnO interface providing both electronic and chemical synergy. Comparative studies demonstrate that ZnO–Ag heterostructures exhibit significantly stronger antimicrobial activity than ZnO–Au or undoped ZnO, with the activity order ZnO–Ag >> ZnO–Au ~ ZnO [127,131]. This superiority arises from multiple interfacial mechanisms: (i) Enhanced ROS generation under photoactivation: The Ag/ZnO interface reduces e^-–h^+ recombination by trapping photogenerated electrons in Ag islands, prolonging the lifetime of holes that generate ROS at the ZnO surface. (ii) Sustained Ag^+ ion release: Ag serves as a reservoir for continuous ion release, providing antimicrobial action in both light and dark conditions. (iii) Improved bacterial membrane interaction: Ag islands enhance surface contact with bacterial membranes, facilitating both ROS delivery and ion penetration. Quantitative evidence for this synergy comes from

upconversion nanoparticle-based systems (UCNP@ZnO:Co/Ag) that achieved >99.9% bacterial kill under NIR irradiation, with >2 to 5-fold ROS enhancement and >2-fold increase in Ag^+ release upon irradiation compared to dark controls [136]. This photo-triggered dual-action mechanism demonstrates how interface engineering can create stimuli-responsive antimicrobial platforms with on-demand activation, reducing off-target toxicity.

- Ag–Cu and Ag–CuO (Z-scheme heterostructures for ROS amplification): Ag–Cu and Ag–CuO interfaces form Z-scheme heterostructures where the Ag_2O–Cu_2O interface promotes efficient charge separation and ROS formation (Figure 7) [137]. The Z-scheme mechanism allows both materials to maintain strong redox potentials—Cu_2O generates e^- with high reducing power while Ag_2O produces h^+ with strong oxidizing ability—by recombining less-useful charge carriers at the interface and preserving the most reactive species for ROS generation. Hydrothermal Ag–CuO nanohybrids demonstrated antimicrobial and antibiofilm activity with MIC values of 4 to 12 mg/mL and MBC values of 2 to 24 mg/mL against *E. coli* and *C. albicans* [13]. While these values remain relatively high compared to optimized systems, the dual ion-release mechanism (Ag^+ and Cu^{2+}) provides complementary antimicrobial pathways that reduce the likelihood of bacterial resistance compared to single-ion systems.

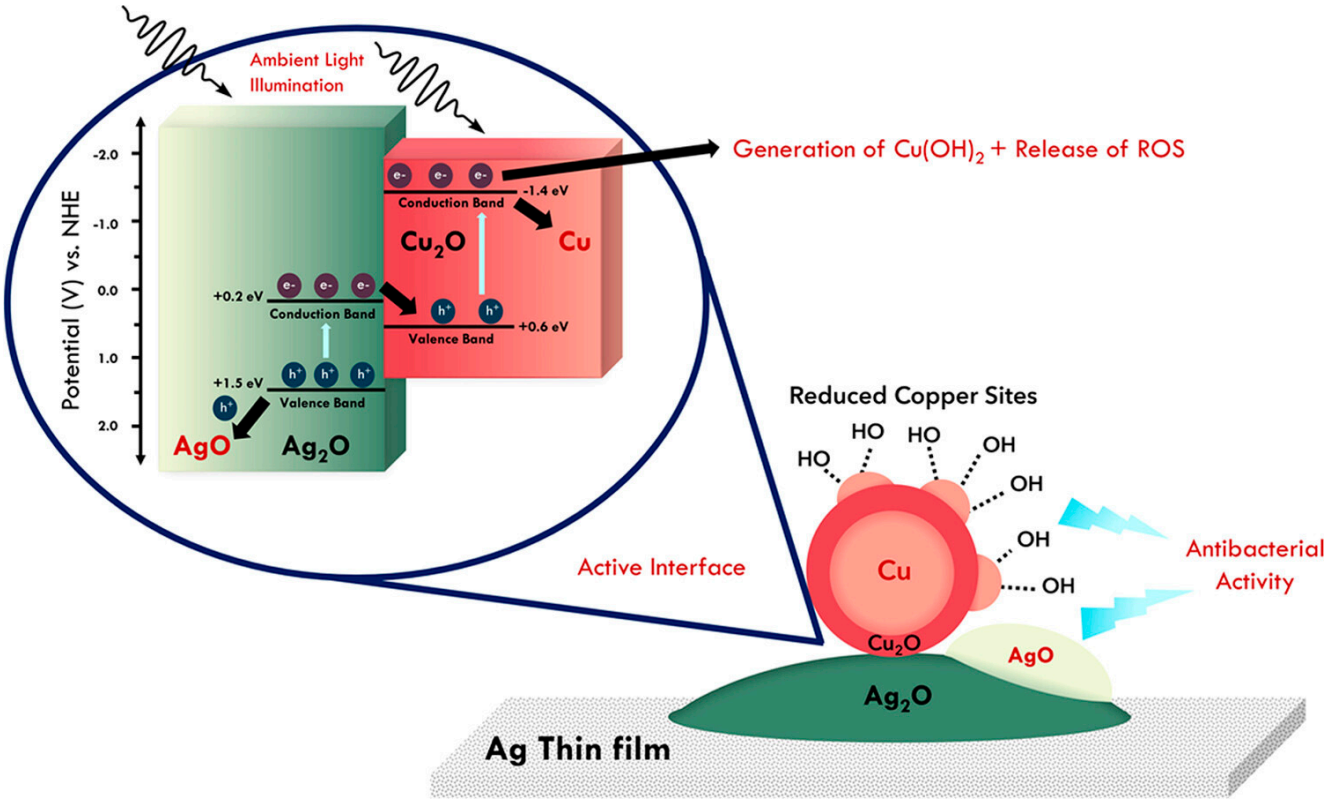


Figure 7. Schematic illustration of the proposed mechanism for the Ag–Cu interface in boosting antibacterial efficacy. Reproduced from [137].

- ZnO–CuO (combined ROS and ion effects with reduced doses): ZnO–CuO heterostructures combine the photocatalytic ROS generation of ZnO with the Cu^{2+} ion release and oxidative stress mechanisms of CuO. A 75 wt% ZnO–CuO composite exhibited substantially improved activity against *S. aureus* with MIC = 0.625 mg/mL and MBC = 2.5 mg/mL, and demonstrated MBC values of 0.3125 to 1.25 mg/mL against multidrug-resistant isolates [138]. These values represent a significant dose reduction compared to monometallic CuO systems, highlighting the efficacy gains achievable through interface engineering. The ZnO–CuO interface likely facilitates e^-

transfer from CuO to ZnO under illumination, reducing e^-–h^+ recombination in ZnO and enhancing ROS production, while simultaneously enabling controlled Cu^{2+} release. This dual mechanism creates a more hostile environment for bacteria, attacking multiple cellular targets (membrane, proteins, DNA) simultaneously and reducing the probability of adaptive resistance.

- Fe_3O_4–ZnO and Cu@Fe (magnetic targeting plus ROS/ion action): Magnetic oxide heterostructures integrate Fenton-like ROS generation and ion release with magnetic targeting and separation capabilities. Copper-containing ferrite NPs (Cu@Fe) achieved an exceptionally low MIC of 1 μg/mL against MRSA, causing membrane rupture and intracellular ROS accumulation in vitro and reducing bacterial organ burden in mouse infection models [133]. The study reported an 'excellent drug safety profile' in vivo, suggesting favorable selectivity for bacterial cells over mammalian tissues. The Cu@Fe interface enables synergistic Fenton-like ROS generation (from Fe) and Cu^{2+}-mediated oxidative stress, while the magnetic properties allow for targeted delivery to infection sites and potential recovery/reuse of the NPs. This represents a critical advantage for clinical translation: magnetic guidance can concentrate antimicrobial NPs at the infection site, reducing systemic exposure and off-target effects.
- Au–TiO_2 and Pt–TiO_2 (plasmonic enhancement of photocatalytic ROS): Noble metal decoration of TiO_2 creates plasmonic heterostructures that extend photoactivation into the visible and NIR spectrum. The Au/TiO_2 and Pt/TiO_2 interfaces enable: (i) SPR-mediated hot-electron injection: Plasmonic excitation of Au or Pt generates energetic electrons that inject into the TiO_2 conduction band, initiating ROS generation without requiring UV light. (ii) Enhanced visible-light absorption: The plasmonic metal extends the absorption spectrum, enabling solar or indoor-light activation. (iii) Reduced e^-–h^+ recombination: The metal acts as an e^- sink, prolonging h^+ lifetime for ROS generation. Fe_3O_4@SiO_2@Au NPs demonstrated this plasmonic enhancement in both antimicrobial and anticancer contexts, with strong T2 magnetic resonance imaging (MRI) contrast enabling imaging-guided therapy [128]. The silica interlayer prevents direct Fe_3O_4–Au contact that could quench plasmonic effects, illustrating the importance of interface engineering at the nanoscale.

In summary, a central advantage of bimetallic heterostructures is dose reduction: by combining 2 antimicrobial mechanisms, lower concentrations of each component can achieve equivalent or superior efficacy compared to high-dose monometallic systems. This dose reduction directly addresses toxicity concerns, as many metal ions (Ag^+, Cu^{2+}) exhibit concentration-dependent cytotoxicity to mammalian cells. The Cu@Fe system's 1 μg/mL MIC against MRSA, combined with reported in vivo safety, exemplifies this principle [133]. Similarly, the photo-triggered activation of UCNP@ZnO:Co/Ag systems provides spatial and temporal control over antimicrobial action, minimizing off-target effects [136].

4.1.3. Trimetallic and Tetrametallic Multi-Mechanism Enhancement: Diminishing Returns or Synergistic Leap?

Trimetallic and tetrametallic systems represent the frontier of interface complexity, integrating 3 or 4 distinct materials to create multi-mechanism antimicrobial platforms. The critical question is whether the addition of 3rd and 4th components provides proportional efficacy gains or encounters diminishing returns due to increased interfacial complexity, potential phase segregation, and synthetic irreproducibility.

- TiO_2–MgO–Au (SPR tuning for visible-light activation): Biosynthesized TiO_2–MgO–Au trimetallic NPs demonstrated enhanced antimicrobial activities attributed to

visible-light activation via Au plasmonic enhancement and improved ROS generation [139]. The addition of MgO to the Au–TiO_2 system may serve multiple roles: (i) pH buffering: MgO can neutralize acidic byproducts of ROS generation, maintaining optimal pH for sustained photocatalytic activity. (ii) Surface area enhancement: MgO can increase surface area and provide additional adsorption sites for bacterial attachment. (iii) Electronic modulation: MgO may alter the band structure of TiO_2, potentially improving charge separation.

- Se/ZnO/CuO (multi-mechanism synergy combining selenium, zinc, and copper): Trimetallic Se/ZnO/CuO nanoalloys fabricated using *Nitraria retusa* extract exhibited antimicrobial activities, with the study reporting multi-mechanism synergy combining Se, ZnO, and CuO actions [140]. Se contributes unique antimicrobial mechanisms, including: (i) Redox cycling: Se can undergo redox reactions that generate ROS. (ii) Protein modification: Se can modify bacterial proteins through selenylation. The combination of Se (redox cycling), ZnO (photocatalytic ROS), and CuO (Cu^{2+} ion release) creates a 3-pronged attack on bacterial cells.
- Ag on $ZnFe_2O_4$@Cu_2S (rapid multi-mechanism killing): Ultrasmall Ag quantum dots (QDs) deposited on $ZnFe_2O_4$@Cu_2S hybrid systems achieved 99.99% killing of *E. coli*, *S. aureus*, and other strains at 175 μg/mL within 40 min [141]. Mechanistic studies using radical scavengers attributed bactericidal activity to large •OH radical production and membrane/ion-channel disruption. This system integrates: (i) Ag QDs: Enhanced Ag^+ ion release due to high surface-to-volume ratio and quantum confinement effects. (ii) $ZnFe_2O_4$: Magnetic targeting and Fenton-like ROS generation. (iii) Cu_2S: Cu^{2+} ion release and potential plasmonic effects in the NIR. The 99.99% kill rate within 40 min represents exceptional kinetics, suggesting strong synergy among the 3 metal components. The rapid action may reduce the opportunity for bacterial adaptive responses and biofilm formation. However, the 175 μg/mL concentration is substantially higher than the 1 μg/mL MIC achieved by bimetallic Cu@Fe against MRSA [133], raising questions about whether the trimetallic complexity provides net advantages over optimized bimetallic systems.

In summary, trimetallic and tetrametallic systems often incorporate structural stabilizers (e.g., silica shells, mesoporous supports) that enhance stability and enable reusability. FePt@HMSN systems, for example, use HSMNs to encapsulate FePt NPs, preventing aggregation and corrosion while providing high surface area for drug loading [132]. The silica support also enables surface functionalization for targeting ligands, creating multifunctional theranostic platforms. Magnetic heterostructures (Fe_3O_4-based systems) enable recovery and reuse through magnetic separation, addressing cost and environmental concerns. However, few studies systematically report reusability metrics (e.g., percent activity retention over multiple cycles) for antimicrobial applications, focusing instead on catalytic or theranostic reuse. Table 3 presents a comprehensive comparison of bi-, tri-, and tetra-heterostructures for antimicrobial activity reported in the literature. The lack of systematic, head-to-head comparisons of mono-, bi-, tri-, and tetra-metallic heterostructures against the same bacterial strains under identical conditions represents a critical gap in the literature. Without such data, it remains unclear whether trimetallic systems provide proportional efficacy gains or encounter diminishing returns due to interfacial complexity, phase segregation, and synthetic variability.

Table 3. Comprehensive comparison of bi-, tri-, and tetra-heterostructures for antimicrobial activity.

Heterostructure	Tested Microorganisms (Gram +/−)	Key Results	Key Outcomes	Ref.
Bi-component heterostructures				
Bi_2O_3/MoO_3 (BOMO)	*Streptococcus pyogenes* (+), *Staphylococcus aureus* (+), *Escherichia coli* (−)	Strong antibacterial activity; BOMO-5 showed greater potential than pure Bi_2O_3.	BOMO-5 nanocomposite exhibits superior antibacterial activity due to synergistic effects and enhanced ROS generation.	[49]
Ag-TiO_2/Bi_2MoO_6 (TBMA)	*E. coli* (−), *Streptomyces albus* (+)	TBMA45 completely inactivated *E. coli* and significantly inhibited *S. albus* after 200 min.	Silver modification and Z-scheme heterojunction enable rapid interfacial charge transfer, enhancing photocatalytic disinfection under visible light.	[77]
Bi_2WO_6/TiO_2 (BWTO)	*E. coli* (−), *S. aureus* (+)	50BWTO (0.35 mg/mL) inhibited 99.80% of *E. coli*; (0.5 mg/mL) inhibited 99.33% of *S. aureus* after 10 min under LED light.	Z-scheme heterojunction promotes efficient charge separation and ROS generation, leading to rapid bacterial inactivation under mild LED light.	[142]
CuO/TiO_2	Sulfate-reducing bacteria (SRB)	Photocatalytic deactivation of SRB; 20%-CuO composite showed the highest activity under visible light (decay constant 1.38 min^{-1}).	CuO incorporation narrows the bandgap and reduces charge recombination, enabling effective visible-light-driven disinfection of problematic SRB in oil industry applications.	[66]
CuO/TiO_2	*E. coli*, *Salmonella typhimurium*, *S. aureus*	ZOI (mm) at 20 mg/mL: 14.34 (*E. coli*), 11.32 (*S. typhimurium*), 9.63 (*S. aureus*). Active against streptomycin-resistant strains. MIC: 1.25 to 5 mg/mL.	Mycosynthesized CuO/TiO_2 shows broad-spectrum activity against both foodborne and antibiotic-resistant phytopathogens, offering a green alternative for agricultural and food safety applications.	[143]
Bi_2MoO_6/Bi_5O_7I (BM/BI)	*E. coli* (−)	BM/BI-3 completely inactivated *E. coli* (10^8 CFU/mL) under 90 min visible light irradiation.	Z-scheme heterojunction enhances charge separation, generating $\bullet O_2^-$ and •OH radicals that damage cell membranes, release intracellular components, and trigger apoptosis.	[87]
Ag, Cu, Co@SiO_2 nanohybrids	*S. aureus* (+), *Streptococcus pneumoniae* (+), MRSA (+), *E. coli* (−), *Klebsiella pneumoniae* (−), *Pseudomonas aeruginosa* (−)	MIC: 12.25 to 1560 µg/mL; MBC: 197 to 3125 µg/mL. The trimetallic nanohybrid showed the best synergistic activity. ZOI at 100 mg/mL: up to 32 mm.	Multimetallic nanohybrids demonstrate superior synergistic antibacterial activity compared to monometallic counterparts, with trimetallic formulation showing highest potency and broad-spectrum coverage.	[144]
Tri-component heterostructures				
CuO/MgO/ZnO	*S. aureus* (+), *E. coli* (−), *Streptococcus mutants* (+), *P. aeruginosa* (−)	ZOI (mm) at 10 mg/disk: 10.33 ± 0.58 (*S. aureus*), 4.27 ± 0.58 (*E. coli*), 14.00 ± 1.00 (*S. mutants*), 23.33 ± 2.08 (*P. aeruginosa*). Better than individual NPs.	Mixed oxide NPs provide larger surface area and enhanced stability, leading to improved antibacterial activity against *P. aeruginosa*, suggesting potential for biomedical applications.	[76]
Dy_2O_3/ZnO-Au (Dy/ZnO-AuNCs@PF)	*Acinetobacter baumannii* (−), *S. aureus* (+), *Proteus mirabilis* (−)	MIC (mg/mL): 5 (*A. baumannii*), 5 (*S. aureus*), 2.5 (*P. mirabilis*). MBC (mg/mL): 80, 40, 20, respectively.	Au NPs significantly enhance catalytic and antibacterial performance. The nanocomposite shows excellent antibacterial activity against both Gram-positive and Gram-negative strains.	[79]

ZnO-TiO_2-Bi_2WO_6/CMCS (ZTB/CMCS)	*E. coli* (−), *S. aureus* (+)	Antibacterial rate >99.999% against both *E. coli* and *S. aureus* after 24 h at 37 °C.	Edible nanocomposite film combines high antimicrobial activity with photocatalytic ethylene degradation, extending banana shelf life in hot-humid environments through multiple protective mechanisms.	[80]
Bi_2SiO_5/$CuBi_2O_4$ (BSO/CBO)	Antibiotic-resistant *E. coli* (−)	BSO/CBO-3 completely inactivated antibiotic-resistant *E. coli* (10^7 CFU/mL) within 2.5 h under visible light. Effectively destroyed tetracycline-resistant genes.	Oxygen vacancies and Z-scheme heterojunction enhance light absorption and charge separation, enabling effective removal of antibiotic-resistant bacteria and their resistance genes from water.	[50]
$BiVO_4$/Bi_2WO_6/WO_3 (BBW)	*E. coli* (−)	Showed significant antibacterial capability against *E. coli*.	Ternary heterojunction with cascade energy band alignment accelerates electron-hole separation, enhancing photocurrent and enabling effective visible-light-driven antibacterial activity with good biocompatibility.	[145]
MnO_2/CuO/NiO (MnNCs)	*E. coli* (−), *K. pneumoniae* (−), *S. aureus* (+), *S. pyogenes* (+)	ZOI (mm) at 75 µg/mL: MnNCs-2: 24 (*E. coli*), 26 (*K. pneumoniae*), 22 (*S. aureus*), 24 (*S. pyogenes*). Good antibacterial efficacy.	Doping MnO_2 with CuO and NiO creates synergistic effects, enhancing antibacterial activity against both Gram-positive and Gram-negative pathogens.	[78]
Ag_2O/CuO/ZnO	*E. coli* (−), *Bacillus cereus* (+), *Salmonella typhi* (−), *S. aureus* (+), *C. albicans* (fungus)	ZOI (mm) at 75 µg/mL for Ag_2O/CuO/ZnO (1:1:1): 23.33 ± 0.56 (*E. coli*), 19.66 ± 0.58 (*B. cereus*), 22.83 ± 0.76 (*S. typhi*), 23.83 ± 0.58 (*S. aureus*), 21.33 ± 0.58 (*C. albicans*).	The ternary nanocomposite shows enhanced antimicrobial activity due to synergistic effects between metal oxides, with smaller particle size (2.35 nm) contributing to better performance.	[83]
Cu/Cr/Ni oxide	*E. coli* (−), *S. aureus* (+)	MIC: 12.5 to 25 µg/mL; MBC: 12.5 to 50 µg/mL against *E. coli* and *S. aureus*.	Optimized green synthesis produces trimetallic NPs with excellent antibacterial activity at low concentrations, offering an eco-friendly alternative for biomedical applications.	[146]
$NiFe_2O_4$@HAp-Ag	*P. aeruginosa* (−), *K. pneumoniae* (−), *S. aureus* (+), *B. cereus* (+)	MIC: 400 to 1600 µg/mL; MBC: 400 to 3200 µg/mL. ZOI at 2000 µg/mL: up to 13 mm (*K. pneumoniae*). Good antibacterial effect.	Magnetically recyclable nanocomposite combines antibacterial silver with biocompatible hydroxyapatite, enabling easy separation and reuse while maintaining potent antimicrobial activity.	[84]
CuO@AgO/ZnO (CAZ)	*S. aureus* (+), *P. aeruginosa* (−)	Under NIR light (808 nm), CAZ (200 µg/mL) achieved 97.22% (*S. aureus*) and 97.13% (*P. aeruginosa*) bactericidal rates. Disrupted *S. aureus* biofilm.	Photothermal therapy (PTT) combined with the intrinsic antibacterial activity of copper and silver enables rapid bacterial killing and biofilm disruption, promoting wound healing with good biocompatibility.	[85]
CuO-Fe_2O_3-MgO	*S. aureus* (+), *E. coli* (−)	ZOI (mm) at 400 mg/mL: G2 sample: 28 (*S. aureus*), 24 (*E. coli*). More active against Gram-positive *S. aureus*.	Glycine concentration influences particle size and antibacterial activity, with smaller particles showing enhanced bacterial inhibition, particularly against Gram-positive strains.	[147]

ZnO:NiO:CuO	*E. coli* (−), *P. aeruginosa* (−), *S. aureus* (+), *Bacillus subtilis* (+)	ZOI (mm) at 2 mg/mL: ZNC (1:1:2) showed 15 (*E. coli*), 15 (*P. aeruginosa*), 17 (*S. aureus*), 10 (*B. subtilis*). More effective against Gram-negative strains.	Ternary heterojunction with optimized molar ratios enhances charge separation and photocatalytic activity, with antibacterial efficacy dependent on crystallite size and bandgap.	[148]
Ag/$Sr_6Bi_2O_{9-\alpha}$–Bi_2O_3 (Ag/SBO-BO)	*Vibrio cholerae* (−)	96.5% inactivation of *V. cholerae* within 40 min under light irradiation. Biocompatible (hemolysis < 5%).	MOF-derived hierarchical heterostructure with silver plasmonic enhancement enables S-scheme charge transfer, producing ROS that effectively inactivate waterborne pathogens with excellent biocompatibility.	[86]
CuO-ZnO-Co_3O_4	*E. coli* (−), *Klebsiella* (−), *Pseudomonas* (−), *Salmonella* (−), *S. aureus* (+), *Candida* (fungus)	ZOI (mm) at 16 mg: 12 (*E. coli*), 15 (*Klebsiella*), 13 (*Pseudomonas*), 13 (*Salmonella*), 14 (S. aureus). Antifungal ZOI at 16 mg: 14 mm (*Candida*).	Co-precipitation synthesis yields a nanocomposite with reduced crystallite size (18.1 nm) and a narrow bandgap (1.3 eV), showing promising antibacterial and antifungal activity against multiple pathogens.	[88]
ZnO-MgO-CuO (ZMC)	*St. pneumoniae* (+), *P. aeruginosa* (−), *E. coli* (−), *S. aureus* (+)	ZOI (mm) at 200 μg/mL: 33 ± 0.14 (*St. pneumoniae*), 34 ± 0.04 (*P. aeruginosa*), 31 ± 0.11 (*E. coli*), 35 ± 0.03 (*S. aureus*). MIC: 5 to 10 μg/mL.	Green-synthesized trimetallic NPs show superior antibacterial activity compared to standard drugs, supported by molecular docking studies confirming strong binding to bacterial protein targets.	[90]
Tetra-component heterostructures				
ZnO-PbO-CdO-CuO (ZPCC)	*B. subtilis* (+), *S. aureus* (+), *E. coli* (−), *P. aeruginosa* (−)	MIC (μg/mL): *B. subtilis*: 9 (light), 11 (dark); *S. aureus*: 11 (light), 13 (dark); *E. coli*: 13 (light), 17 (dark); *P. aeruginosa*: 15 (light), 19 (dark). MBC (μg/mL): *B. subtilis*: 11 (light), 13 (dark); *S. aureus*: 13 (light), 15 (dark); *E. coli*: 15 (light), 19 (dark); *P. aeruginosa*: 17 (light), 21 (dark). ZOI: 15 to 25 mm range depending on condition.	Quaternary ZPCC demonstrated excellent photoinduced antibacterial activity due to synergistic effects of multiple metal oxides. The lower band gap (2.30 eV) enabled efficient electron excitation and ROS generation under visible light. SEM revealed bacterial cell wall disruption and damage. ZPCC outperformed all binary counterparts (ZnO-CuO, CdO-CuO, PbO-CuO).	[123]
Ag_2O/CuO/ZnO-MWCNT (MWCNTs@ACZ-NC)	*S. aureus* (+), *E. coli* (−)	ACZ-NC showed higher activity than MWCNTs@ACZ-NC. ZOI (mm) at 1 mg/mL: ACZ-NC: 22.5 (*S. aureus*), 18.3 (*E. coli*).	MWCNT incorporation slightly reduces direct antibacterial contact while improving overall multifunctionality.	[4]
Zr Al Fe Co Ni LDH	*B. subtilis* (+), *S. aureus* (+), *St. pneumoniae* (+), *Listeria monocytogenes* (+), *E. coli* (−), *Haemophilus influenza* (−), and *Aspergillus* spp., *Mucor indicus*, *Penicillium notatum*, *C. albicans*	MIC range: 4 to 166.7 μg/mL (best among all tested LDHs). MBC range: 4 to 166.7 μg/mL. ZOI at 1000 μg: up to 32.33 mm against *S. aureus* and *St. pneumoniae*. Antifungal MIC: as low as 21 μg/mL against *Mucor* sp. Biofilm inhibition: 95.13% (*S. aureus*), 92.73% (*St. pneumoniae*), 85.80% (*E. coli*),	Zirconium incorporation significantly enhanced antimicrobial efficacy. Zirconium ions disrupt negatively charged bacterial cell walls through electrostatic interactions. UV illumination further enhanced photo-activation. The growth curve showed OD600 reduced to 0.49 vs. control 2.00. Demonstrated broad-spectrum	[125]

	73.37% (*Mucor* sp.). Protein leakage at 1.0 mg/mL: 191.98 μg/mL.	activity against bacteria, fungi, and biofilm.

4.2. Anticancer and Theranostic Applications: From Passive Carriers to Active Multimodal Platforms

4.2.1. Monometallic to Bimetallic Transition: Integrating Imaging and Therapy

Monometallic NPs exhibit cytotoxicity through ROS generation, ion release, or photothermal effects, but function primarily as passive carriers or single-mechanism therapeutic agents. Bimetallic heterostructures transform these materials into active theranostic platforms that integrate imaging, targeting, and therapy within a single nanoparticle architecture.

Monometallic systems such as Ag, CuO, and Au NPs demonstrate anticancer activity through mechanisms analogous to their antimicrobial action: (i) Ag NPs: Induce oxidative stress and apoptosis in cancer cells through Ag^{+} ion release and ROS generation, but lack selectivity and exhibit dose-dependent toxicity to normal cells [149]. (ii) CuO NPs: Release Cu^{2+} ions that disrupt mitochondrial function and induce apoptosis [150]; Ag–CuO nanohybrids produced dose-dependent toxicity and apoptosis in HCT-116 colon cancer cells [13]. (iii) Au NPs: Provide photothermal therapy (PTT) through plasmonic heating, but lack intrinsic imaging contrast and require high laser powers for effective therapy [151]. The primary limitation of monometallic systems is their single functionality: they provide either therapy or imaging, but not both, and lack targeting mechanisms to concentrate at tumor sites, resulting in high systemic doses and off-target toxicity. Bimetallic heterostructures overcome monometallic limitations by integrating complementary functionalities at the interface:

- Fe_3O_4–ZnO (magnetic targeting plus hyperthermia and photodynamic therapy (PDT)): Fe_3O_4–ZnO heterostructures combine the magnetic targeting and hyperthermia capabilities of Fe_3O_4 with the photodynamic ROS generation of ZnO. External magnetic fields can guide Fe_3O_4–ZnO NPs to tumor sites, concentrating the therapeutic dose while reducing systemic exposure. Upon NIR or UV irradiation, ZnO generates ROS for PDT, while magnetic hyperthermia (alternating magnetic field-induced heating of Fe_3O_4) provides a complementary thermal ablation mechanism. This dual-therapy approach attacks cancer cells through both oxidative and thermal stress, reducing the likelihood of resistance.
- Ag–Au (PTT plus imaging capabilities): Ag–Au bimetallic NPs combine the broad-spectrum antimicrobial and cytotoxic effects of Ag with the plasmonic photothermal properties of Au. The Ag–Au interface enables tunable plasmonic resonance across visible to NIR wavelengths by varying the Ag:Au ratio and nanoparticle morphology (core–shell, alloy, or Janus structures). This tunability allows optimization for specific laser wavelengths used in clinical PTT (typically 808 nm or 1064 nm NIR lasers that penetrate tissue with minimal absorption by water and hemoglobin).
- Au–Fe_3O_4 (MRI contrast plus PTT and targeting): Au–Fe_3O_4 heterostructures integrate MRI contrast (Fe_3O_4), PTT (Au), and magnetic targeting in a bimetallic platform. The interface between Au and Fe_3O_4 is critical for maintaining both magnetic and plasmonic properties: direct contact can lead to magnetic quenching or plasmonic damping, necessitating careful interface engineering (e.g., silica interlayers or controlled oxidation states).
- FePt@HMSN (NIR PTT with low dark cytotoxicity): FePt NPs supported on HMSN exhibited strong NIR absorption at 1064 nm and effective photothermal killing of HeLa cells with low dark cytotoxicity [132]. The system demonstrated synergistic

photothermal and chemotherapeutic effects when loaded with topotecan, a topoisomerase inhibitor. The hollow mesoporous structure provides: (i) High drug-loading capacity: The hollow core and mesoporous shell enable loading of hydrophobic chemotherapeutics. (ii) Controlled release: Drug release can be triggered by NIR-induced heating, providing on-demand therapy. (iii) Magnetic properties: FePt exhibits ferromagnetism, enabling magnetic targeting and potential MRI contrast (though relaxivity values are not reported in the study). The 1064 nm activation wavelength is particularly advantageous for deep-tissue therapy, as this wavelength falls in the 'second NIR window' (1000 to 1350 nm) with minimal tissue absorption and scattering.

- IR780-Loaded Fe_3O_4 (IRFes; magnetic field-guided targeted PTT): IRFes combined magnetic targeting with NIR PTT and fluorescence imaging (Figure 8) [152]. External magnetic field guidance concentrated IRFes at 4T1 tumor sites in mice, and subsequent 808 nm laser irradiation achieved tumor ablation. The system also provided NIR fluorescence imaging capability through the IR780 dye, enabling real-time visualization of nanoparticle accumulation at tumor sites. This represents a complete theranostic workflow: magnetic targeting → NIR fluorescence imaging confirmation → laser-guided PTT.

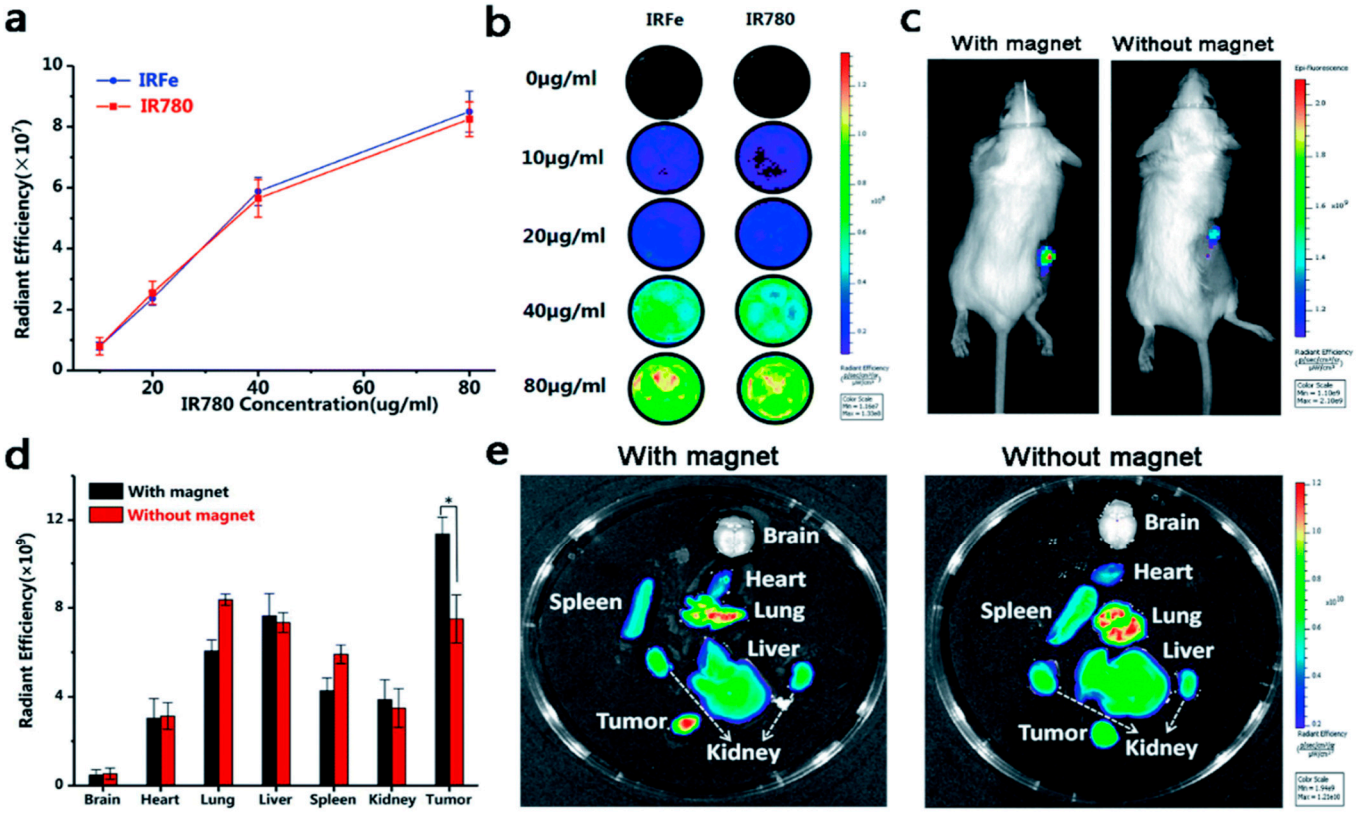


Figure 8. (**a**) In vitro NIR fluorescence images and (**b**) intensity profiles of IR780 and IRFes. (**c**) In vivo NIR fluorescence imaging of tumors 24 h after IRFes injection, comparing conditions with and without magnetic targeting. (**d**) Quantified average NIR fluorescence signals in organs and tumors (statistically significant differences indicated). (**e**) Ex vivo NIR fluorescence images of harvested organs and tumors. Reproduced from [152].

In summary, bimetallic theranostic platforms provide: (i) Dual functionality: Simultaneous imaging and therapy within a single nanoparticle. (ii) Reduced systemic toxicity: Magnetic or active targeting concentrates NPs at tumor sites, reducing required systemic doses. (iii) Stimuli-responsive therapy: Photo- or magnetic-triggered activation provides

spatial and temporal control, minimizing off-target effects. (iv) Therapeutic windows: Low dark toxicity with substantial increases upon activation demonstrates selectivity for irradiated tumor regions.

4.2.2. Trimetallic and Tetrametallic Multimodal Theranostics: Comprehensive Platforms

Trimetallic and tetrametallic systems extend bimetallic theranostic concepts by integrating additional imaging modalities or therapeutic mechanisms, creating comprehensive platforms capable of multimodal imaging, targeted delivery, and combination therapy.

- Fe_3O_4@SiO_2@Au (MRI-guided chemo/NIR photothermal therapy): Fe_3O_4@SiO_2@Au core–shell NPs represent a sophisticated trimetallic theranostic platform integrating MRI, PTT, and chemotherapy [128]. The architecture consists of: (i) Fe_3O_4 core: Provides strong T2 MRI contrast for tumor imaging and magnetic targeting. (ii) SiO_2 interlayer: Prevents direct Fe_3O_4–Au contact that could quench plasmonic effects, provides biocompatibility, and enables surface functionalization for drug loading. (iii) Au shell: Enables NIR photothermal therapy through plasmonic heating. Quantitative anticancer data demonstrate the therapeutic window: Fe_3O_4@SiO_2@Au exhibited low dark cytotoxicity (~10 to 15% cell death) in 2 colon cancer cell lines, increasing to ~43 to 50% cell death under 808 nm laser irradiation [128]. This 3- to 5-fold increase in cytotoxicity upon laser activation demonstrates spatial and temporal control over therapy, minimizing off-target effects. The strong T2 MRI contrast enables real-time imaging to guide laser application to tumor sites, creating a closed-loop theranostic system.
- A study [71] successfully constructed methotrexate-loaded Bi2S3-coated with Fe/Mn-bimetallic doped ZIF-8 nanocomposites (B@FMZ/MTX) for synergistic PTT, chemodynamic therapy (CDT), and chemotherapy in cancer treatment (Figure 9). B@FMZ NPs demonstrated a strong PTT effect under 808 nm laser irradiation, with the temperature rising to 52 °C at 1 mg/mL concentration within 10 min. They also showed excellent photothermal stability over 3 laser on/off cycles, with a photothermal conversion efficiency of 54%. This intense PTT effect is attributed to the Bi_2S_3 nanorods. The B@FMZ NPs enhanced the decomposition of H_2O_2 in the tumor microenvironment (TME), leading to the generation of toxic •OH radicals via a Fenton-like reaction. This significantly improved the CDT effect, which was further enhanced by NIR laser irradiation. The B@FMZ/MTX NPs exhibited a prominent drug release efficiency of 87.25% at pH 5.5 under NIR laser irradiation, significantly higher than at pH 7.4. This pH- and laser-responsive drug release mechanism enhances the effectiveness of chemotherapy. B@FMZ NPs intensified the CT signal in a concentration-dependent manner, indicating their potential as effective CT contrast agents due to the high X-ray attenuation coefficient of Bi_2S_3 nanorods. In vivo studies confirmed strong CT signals in tumor-bearing mice after intratumoral injection. The NPs showed promising T_2-weighted MRI contrast enhancement, with an r^2 value of 5.38 $mg^{-1}s^{-1}$, attributed to the paramagnetic properties of iron ions. In vivo MRI also showed an intense signal in the tumor region after nanoparticle administration.

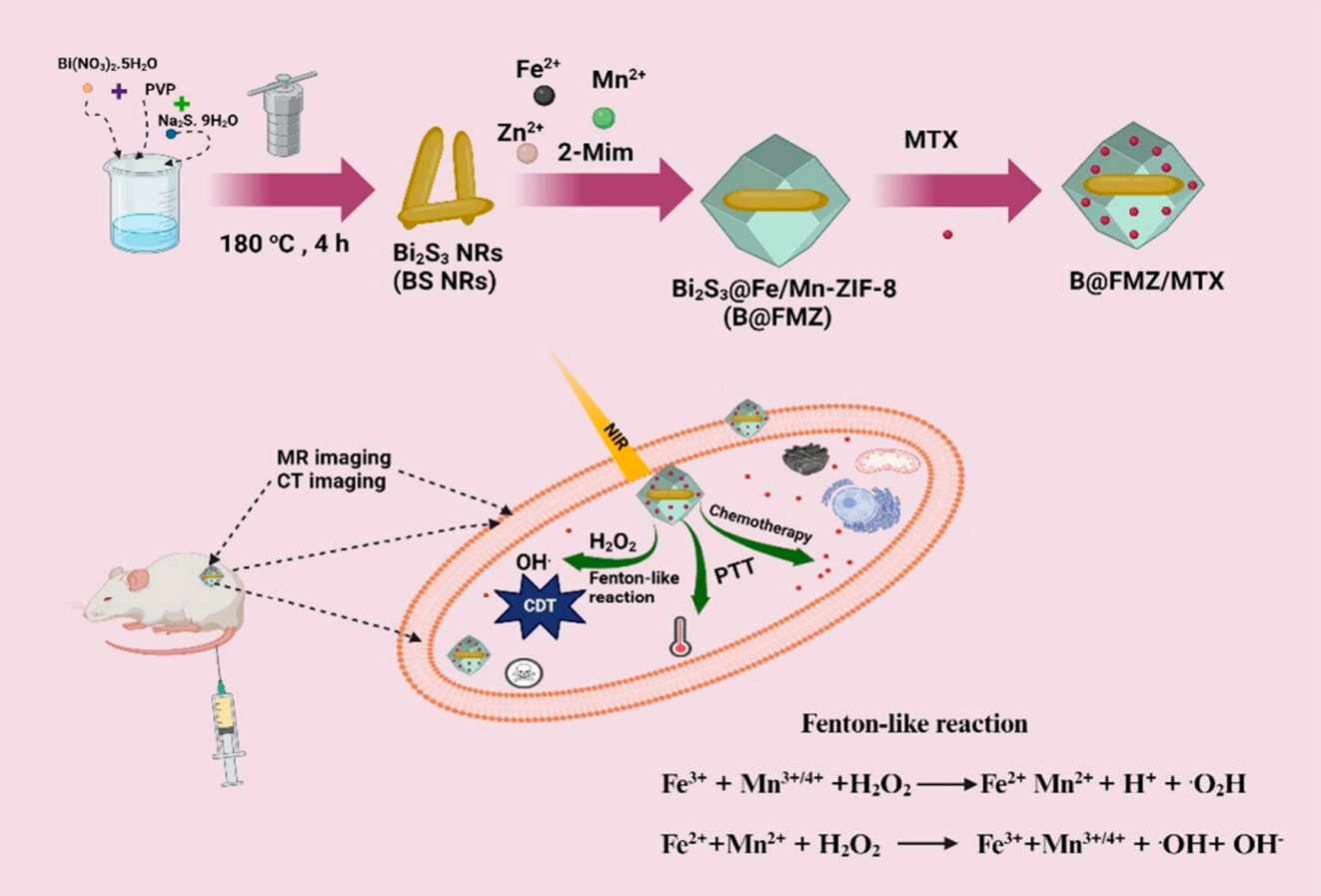


Figure 9. Schematic illustration of B@FMZ/MTX NPs for multimodal imaging-guided synergistic cancer therapy (CDT/PTT/chemotherapy). Reproduced from [71].

- Addition of Au for PTT, X-ray imaging, and drug delivery: Au's high atomic number (Z = 79) provides strong X-ray attenuation, enabling computed tomography (CT) imaging in addition to plasmonic PTT [153]. This represents a 'quadruple-modality' theranostic platform (MRI, CT, PTT, magnetic targeting) within a trimetallic nanoparticle. However, the synthesis and characterization complexity increases substantially, and the available literature does not provide systematic in vivo tumor reduction data comparing trimetallic systems to bimetallic controls.

The theoretical advantage of trimetallic and tetrametallic theranostic systems is the integration of multiple imaging modalities (MRI, CT, fluorescence, photoacoustic) with multiple therapeutic mechanisms (PTT, PDT, chemotherapy, immunotherapy) and targeting capabilities (magnetic, ligand-mediated, pH-responsive). This comprehensive approach could enable: (i) Preoperative imaging: Tumor detection and staging using MRI/CT. (ii) Intraoperative guidance: Real-time fluorescence or photoacoustic imaging during surgery. (iii) Targeted therapy: Magnetic or ligand-mediated accumulation at tumor sites. (iv) Combination therapy: Simultaneous PTT, PDT, and chemotherapy to overcome resistance. (v) Post-treatment monitoring: MRI/CT assessment of tumor response. While the theoretical advantages are compelling, in vivo tumor reduction data for trimetallic and tetrametallic systems are limited in the available literature [132,139,140].

The lack of in vivo data for trimetallic systems contrasts with the more extensive in vivo validation of bimetallic platforms (e.g., IRFes achieving 4T1 tumor ablation [152]), suggesting that the increased complexity of trimetallic systems may pose translational challenges. The rationale for trimetallic and tetrametallic theranostic systems is to create 'all-in-one' platforms that eliminate the need for multiple separate imaging and

therapeutic agents, reducing: (i) Patient burden: Single injection instead of multiple contrast agents and therapeutics. (ii) Pharmacokinetic complexity: Unified biodistribution instead of coordinating multiple agents with different clearance rates. (iii) Regulatory complexity: Single formulation instead of multiple drug approvals.

However, these advantages must be weighed against: (i) Synthetic complexity: Reproducible synthesis of multi-component NPs with controlled composition and interface quality. (ii) Characterization challenges: Comprehensive physicochemical and biological characterization of complex systems. (iii) Potential toxicity: Cumulative toxicity of multiple metal components. (iv) Regulatory uncertainty: Lack of clear regulatory pathways for multi-component nanomedicines.

4.2.3. Comparative Summary

The primary advantage of a bi-heterostructure is the interface created between 2 different materials. This interface fundamentally alters electronic properties. (i) Schottky junctions and charge separation: In systems like TiO_2/Au [44] and Au-Bi_2O_3 (ABO) [43], the metal-semiconductor interface forms a Schottky junction. Under excitation (light or ultrasound), this junction acts as an e^- trap, preventing the rapid recombination of e^-'s and h^+'s. This separation allows the charge carriers more time to participate in redox reactions with water and oxygen, leading to a significant increase in the generation of cytotoxic ROS. For ABO, this resulted in a 7-fold increase in therapeutic efficacy [43]. (ii) LSPR: Noble metals like Au and Ag exhibit LSPR, where they strongly absorb light at specific wavelengths (e.g., NIR). In Au-Bi_2O_3 [43] and PLGA@IR780-Bi-DTPA (PIBD) [72], this property is harnessed for PTT, converting light into lethal heat. In the case of PIBD, this heat generation also served to alleviate tumor hypoxia, thereby enhancing the effectiveness of concurrent radiotherapy [72]. (iii) Dual apoptotic pathways: Bi-heterostructures like ZnO-Ag [46] combine the distinct biological effects of 2 metals. The study showed that while Ag or ZnO alone had little effect at 10 μg/mL, the combination resulted in >93% cancer cell death, likely due to the dual induction of apoptosis and ROS [46].

Tri-heterostructures introduce a 3rd component, adding layers of functionality that enable complex, multi-stage therapeutic strategies. (i) High surface area for drug delivery: The introduction of porous materials like metal–organic frameworks (MOFs) in B@FMZ/MTX [71] or mesoporous shells in Pt@CeO_2@MnO_2 [70] creates a high surface area (e.g., 250 m^2/g for B@FMZ) for loading high quantities of chemotherapeutic drugs like DOX or MTX. (ii) TME-responsive 'smart' release: The outermost layer of a tri-heterostructure can be engineered to degrade specifically in the TME. For example, the MnO_2 shell in Pt@CeO_2@MnO_2 [70] and the ZIF-8 shell in B@FMZ/MTX [71] are pH-sensitive. This ensures that the drug is preferentially released at the tumor site (pH 5.5), minimizing systemic toxicity. The B@FMZ/MTX system achieved an impressive drug release of 87.25% at pH 5.5 with NIR, compared to only 19.97% at pH 7.4 [71]. (iii) Architectural amplification of PTT: The unique 3D flower-like 'superstructure' of BiCuOS nanoflowers [45] is a prime example of how morphology dictates function. The vertical arrangement of 2D nanoplates acts as multiple 'laser-cavity mirrors,' trapping and internally reflecting NIR light. This architecture dramatically increases the material's absorption cross-section, leading to a high photothermal conversion efficiency of 45.5%, which is crucial for effective PTT [45].

Tetra-heterostructures represent the pinnacle of nanoplatform engineering, integrating multiple functional ions and molecules into a single, cohesive particle to achieve a 'pro-theranostic' effect. (i) Multi-modal imaging and targeting: The Gd-Ti-FA-TA NPs [75] incorporate Gd^{3+} for MRI, a NIR dye (cypate) for optical imaging, and folic acid for active tumor targeting. This allows for non-invasive, real-time tracking of nanoparticle biodistribution, ensuring that therapy is only activated once maximum accumulation at the

tumor site is confirmed. (ii) On-demand activation by external triggers: This is the defining feature of a tetra-heterostructure. The Gd-Ti-FA-TA NPs themselves are relatively non-toxic (IC_{50} of 263 μg/mL). However, coordination with Ti^{4+} narrows the material's band gap to 2.04 eV [75]. This allows it to be activated by the low-energy Cerenkov radiation emitted from a clinically used radiopharmaceutical (^{18}FDG). This radionuclide-stimulated dynamic therapy (RaST) triggers a burst of cytotoxic ROS only at the tumor site, turning a diagnostic tracer into a therapeutic trigger and achieving precise, controlled cancer cell killing [75].

In summary, the available evidence suggests that optimized bimetallic systems may represent the optimal balance between enhanced functionality and practical translation feasibility. These systems achieve exceptional efficacy (1 μg/mL MIC, >99.9% kill rates, >2 to 5× ROS enhancement) with manageable synthetic complexity and emerging in vivo validation. Trimetallic and tetrametallic systems should be pursued only when they provide unique, clinically relevant advantages—such as multimodal imaging capabilities or combination therapies that cannot be achieved with bimetallic platforms—and when the increased synthesis complexity, potential toxicity, and regulatory challenges can be justified by proportional gains in therapeutic efficacy (Table 4). The future depends on moving beyond proof-of-concept demonstrations to rigorous comparative studies, comprehensive in vivo validation, and systematic assessment of the risk-benefit balance across the complexity spectrum. Only through such evidence-based evaluation can the promise of synergistic interfaces be translated into clinical and environmental applications that improve human health and sustainability.

Table 4. Comprehensive comparison of bi-, tri-, and tetra-heterostructures for anticancer activity.

Heterostructure	Key Components	Anticancer Strategy/Mechanism	Key Result(s)	Key Outcomes/Findings	Ref.
Bi-component heterostructures					
TiO_2/Au	Au NPs + TiO_2 NWs	Chemo-dynamic therapy (Enhanced ROS)	HELA: Cell viability reduced to ~6.9% at 48 μg/mL (41% improvement over TiO_2). MCF7: Cell viability reduced to ~6.3% at 48 μg/mL (43% improvement).	Decoration of TiO_2 NWs with Au NPs significantly enhances anticancer activity, making the nanocomposite a promising candidate for inhibiting cancer cell growth.	[44]
ZnO-Ag	Ag NPs + ZnO NPs	Apoptosis/ROS	HELA: ~93.1% cell death at 10 μg/mL (LC_{50} = 7.63 μg/mL). HCT-116: ~93.7% cell death at 10 μg/mL (LC_{50} = 7.39 μg/mL).	The bimetallic composite shows high anticancer activity at low concentrations (10 μg/mL), making it suitable for cancer treatment with enhanced purity via laser ablation.	[46]
Au@Pt NPs	Au + Pt (alloy/core–shell)	Chemotherapy (via DOX)	HeLa IC_{50}: DOX/Au@Pt (6.94 μg/mL) vs. free DOX (14.32 μg/mL). HepG2: 3-fold higher cell death than free DOX at 20 μg/mL.	DOX-loaded bimetallic NPs show a 3-fold increase in apoptosis and pH-responsive release, making them a potential supplement for cervical and hepatocellular cancer therapy.	[154]

Au-Bi_2O_3 (ABO)	Au NRs + Bi_2O_3	Sonodynamic/photothermal/immunogenic cell death	4T1: ~8.2% cell viability (ABO + US + NIR); ~7x more effective than additive individual effects.	The metal-sensitized sonocatalyst triggers immunogenic cell death, reverses the immunosuppressive TME, and significantly suppresses tumor development both in vitro and in vivo.	[43]
Cu-Mn (CMBNPs)	Cu + Mn (alloy)	DNA damage/genotoxic Stress	HT-29 IC_{50}: 115.2 μg/mL. Significant inhibition of cell migration and increase in DNA tail length (Comet assay).	Green-synthesized bimetallic NPs show dose-dependent cytotoxicity, inhibit cancer cell migration, and cause significant DNA damage, offering a clean, eco-friendly anticancer agent.	[65]
$BiVO_4$/Fe_3O_4@PDA SPs	$BiVO_4$ NPs + Fe_3O_4 NPs (in PDA shell)	Radiotherapy/PTT	KB: Clonogenic survival of only 2.1% (SPs + X-ray + NIR), demonstrating strong synergy.	Integrating multiple imaging modalities (CT/PA/MR) and therapeutic strategies (RT/PTT) into a single superparticle provides sensitive multimodal imaging and superior synergistic tumor therapy.	[74]
Pd-Pt NPs	Pd + Pt (alloy)	Autophagy modulation	LS180 IC_{50} (24 h): 46 to 90 μg/mL. SW480 IC_{50} (24 h): 320 to 436 μg/mL. Significant impact on Beclin-1, LC3, and P62 gene expression.	Green-synthesized NPs induce cell death through autophagy modulation, with effects dependent on concentration, time, and cell line characteristics.	[47]
Mn_3O_4-Ag_2S Janus NPs	Mn_3O_4 + Ag_2S (Janus)	PTT/CDT	4T1 IC_{50} (24 h): 263 μg/mL (ATP assay). Significant temperature increase (to ~59 °C under a 1064 nm laser for PTT.	The Janus nanostructure enables T1-MRI contrast, PTT in the NIR-II window, and TME modulation via Fenton-like activity, showing potential for cancer theranostics.	[47]
PLGA@IR780-Bi-DTPA (PIBD)	IR780 (photosensitizer) + Bi-DTPA (radiosensitizer) (in PLGA)	PTT-enhanced radiotherapy	In vitro (4T1): 3.24% cell viability; 94.3% apoptosis rate (PIBD + X-ray + NIR). In vivo: Complete tumor elimination (volume recorded as 0).	PTT from IR780 alleviates tumor hypoxia, enhancing radiotherapy efficacy. The targeted nanodrug enables multi-modality imaging (PA, NIRF, CT) and provides a safe, efficient theranostic method.	[72]
Tri-component heterostructures					
BiCuOS nanoflowers	Bi_2O_3 nanoplates + CuS base + S (oxychalcogenide)	Chemo-PTT (via DOX)/ROS	Hep-2: DOX-loaded nanoflowers + NIR resulted in only 8.2% cell viability. PCE of 45.5%.	The flower-like superstructures act as laser-cavity mirrors, enhancing PCE. They show excellent biocompatibility and synergistic chemo-photothermal anticancer activity.	[45]
Bi_2S_3@Fe/Mn-ZIF-8 (B@FMZ/MTX)	Bi_2S_3 core + Fe/Mn-ZIF-8 shell + MTX (drug)	PTT/CDT/chemotherapy	HepG2: ~19% cell viability (81% apoptosis) at 200 μg/mL (B@FMZ/MTX + NIR). Drug release	The core–shell structure enables dual-modal imaging (MRI/CT)-guided synergistic therapy (PTT/CDT/chemo). PTT enhances CDT efficacy by intensifying •OH production.	[71]

			efficiency is 87.25% at pH 5.5 with NIR.		
$Pt@CeO_2@MnO_2$	Pt core + CeO_2 interlayer + MnO_2 shell + DOX (drug)	PTT/PDT/chemotherapy	HepG-2: <10% cell viability at 200 μg/mL (DOX-loaded + NIR). PCE of 80%. DOX release up to 80% in TME-mimicking conditions.	The multi-layer structure allows for TME-responsive drug release, enhanced PDT via oxygen generation, and efficient PA imaging-guided trimodal synergistic therapy.	[70]
TNT/$CuFe_2O_4$/Zn-Fe MMO	Titanate nanotubes + $CuFe_2O_4$ + Zn-Fe MMO	Inorganic anticancer agent (cellular uptake)	PC-3 IC_{50}: 29.8 ± 0.6 μg/mL. Dose-and time-dependent cytotoxicity confirmed by membrane damage and ultrastructural changes.	The ternary nanocomposite is highly taken up by PC-3 cells via clathrin-mediated endocytosis, showing potential as a promising inorganic anticancer agent for prostate cancer.	[155]
ZnO/ZrO_2/rGO nanocomposites	ZnO NPs + ZrO_2 NPs + rGO sheets	Oxidative Stress/Apoptosis	A549 IC_{50}: 12 μg/mL (vs 40 μg/mL for ZnO NPs). MCF7 IC_{50}: 10 μg/mL (vs. 47 μg/mL). ~3.5-fold higher efficacy than pure ZnO.	Green-synthesized nanocomposite shows enhanced anticancer efficacy and improved biocompatibility, mediated by oxidative stress (ROS generation and GSH depletion).	[73]
Tetra-component heterostructures					
Gd-Ti-FA-TA NPs	Gd^{3+} + Ti^{4+} + tannic acid + folic acid + cypate (dye)	Radionuclide-stimulated dynamic therapy (RaST)	4T1 IC_{50} (24 h, ATP): 263 μg/mL. NPs + ^{18}FDG (RaST) significantly potentiated cell death to ~30% viability.	The 'pro-theranostic' platform allows MRI/NIR fluorescence imaging of drug delivery. RaST activates cytotoxic ROS generation, providing a strategy for image-guided, externally triggered precision cancer therapy.	[75]
$K_4Nb_6O_{17}$/α-Fe_2O_3/Fe_3N/g-C_3N_4	$K_4Nb_6O_{17}$, α-Fe_2O_3, Fe_3N, g-C_3N_4	Photocatalytic generation of ROS under visible light, leading to cancer cell death (apoptosis).	IC_{50} (U87-MG, 45 min): 1 mg/mL. Cell viability reduced by ~50% at IC_{50} concentration under visible light.	The photocatalyst exhibits minimal toxicity in darkness but shows significant, concentration-dependent anticancer efficacy under visible light. This is attributed to ROS generation, confirmed by DHE staining, which showed intense green fluorescence in treated cells.	[116]

5. Comparative Analysis: The 'Interface' in Photocatalytic Dye Degradation

The efficacy of photocatalytic dye degradation hinges fundamentally on 2 interrelated challenges that plague single-component metal oxide semiconductors: wide band gaps that restrict photoactivation to the UV spectrum, and rapid e^-h^+ recombination that drastically reduces quantum efficiency. These limitations confine monometallic oxides to UV-only operation and yield disappointingly low degradation rates, rendering them impractical for real-world wastewater treatment under solar irradiation. The strategic engineering of interfaces—whether metal-semiconductor Schottky junctions, plasmonic metal-oxide contacts, or multi-component heterojunctions—has emerged as the principal mechanism to overcome these fundamental constraints. This section critically examines how increasing interface complexity, from monometallic to bimetallic, trimetallic, and

tetrametallic systems, progressively addresses band gap and recombination limitations, and evaluates whether the performance gains justify the added synthetic complexity.

5.1. Monometallic: Fundamental Limitations

5.1.1. Wide Band Gaps and UV-Only Activation

Monometallic metal oxides, despite their chemical stability and low cost, suffer from intrinsic band gap energies that severely restrict their photocatalytic utility. The archetypal photocatalyst TiO_2 exhibits a band gap of 3.2 eV [156], confining photoactivation to wavelengths below ~388 nm—a mere 3 to 5% of the solar spectrum. Under these constraints, bare TiO_2 demonstrates baseline pseudo-first-order rate constants as low as $k = 0.0141\ min^{-1}$ for rhodamine B degradation [157], reflecting the fundamental mismatch between its electronic structure and the solar emission profile.

ZnO, another widely studied n-type semiconductor, presents a similarly restrictive band gap of 3.14 eV [158]. Under visible light irradiation, pristine ZnO achieves only 55.5% dye degradation over 120 min with a pseudo-first-order rate constant of $k = 0.008\ min^{-1}$ [158]—a performance level inadequate for practical industrial effluent treatment. The visible-light inactivity stems directly from the insufficient photon energy to promote valence band electrons across the 3.14 eV gap, leaving the vast majority of solar photons unutilized.

Other monometallic oxides exhibit comparable or even wider band gaps. CuO-coupled TiO_2 systems show modest improvements ($k \approx 0.0341\ min^{-1}$) [157], while SnO_2/TiO_2 composites reach $k \approx 0.0327\ min^{-1}$ [157], yet these remain far below the performance thresholds required for rapid, visible-light-driven degradation. The fundamental issue is clear: without interface engineering to enable sub-band-gap excitation or charge transfer pathways, monometallic oxides remain trapped in the UV regime.

5.1.2. Rapid e^-–h^+ Recombination: The Nanosecond Barrier

Even when photogenerated, e^-–h^+ pairs in monometallic oxides recombine on nanosecond timescales, drastically reducing the population of charge carriers available for ROS generation. Time-resolved photoluminescence (TRPL) measurements reveal that pristine ZnO exhibits charge carrier lifetimes of approximately 5.2 ns [159]—a window far too brief for efficient migration to surface active sites and subsequent redox reactions with adsorbed dye molecules and dissolved oxygen. This rapid recombination manifests as intense photoluminescence emission, a direct spectroscopic signature of wasted excitation energy. The consequence is a severe bottleneck: even if UV photons successfully generate e^-–h^+ pairs, the majority recombine before participating in catalytic chemistry. The net result is low quantum efficiency and sluggish degradation kinetics. For instance, bare ZnO's $k = 0.008\ min^{-1}$ reflects not only limited light absorption but also the overwhelming dominance of recombination over productive charge separation.

The recombination problem is not unique to ZnO. Across the family of monometallic oxides (TiO_2, CuO, Fe_2O_3, WO_3, SnO_2, $BiVO_4$, Bi_2O_3, CeO_2, MnO_2, NiO, Co_3O_4), the absence of built-in electric fields or interfacial charge-separation mechanisms results in carrier lifetimes in the low nanosecond range. Without spatial separation of e^- and h^+, recombination outcompetes surface reactions, and photocatalytic efficiency remains disappointingly low.

In summary, the dual constraints of wide band gaps and rapid recombination render monometallic metal oxides largely impractical for solar-driven wastewater treatment. Degradation times exceeding 120 min for moderate dye concentrations, coupled with UV-only activation, translate to high energy costs and limited throughput. The baseline performance of TiO_2 and ZnO underscores the urgent need for interface engineering strategies that simultaneously extend light absorption into the visible spectrum and suppress

recombination. The following sections demonstrate how bimetallic, trimetallic, and tetrametallic interfaces systematically address these limitations.

5.2. Bimetallic Heterostructures: Schottky Barriers and Plasmonic Enhancement

5.2.1. Schottky Barrier Mechanism: The Electron Sink

The introduction of a metal-semiconductor interface fundamentally alters the charge carrier dynamics by creating a Schottky barrier—a rectifying junction that acts as an e^- sink [160]. When a noble metal (e.g., Au, Ag, Pt, Pd) is deposited onto a metal oxide semiconductor, the difference in work functions drives e^- transfer from the oxide conduction band to the metal until Fermi level equilibration is achieved [160]. This process creates a depletion region in the semiconductor and an upward band bending at the interface, establishing a built-in electric field that facilitates e^- migration toward the metal.

Upon photoexcitation, e^- promoted to the oxide conduction band are rapidly captured by the metal NPs, where they accumulate due to the Schottky barrier's rectifying nature [161]. This spatial separation of e^- (in the metal) and h^+ (in the oxide valence band) drastically prolongs charge carrier lifetimes, reducing recombination rates and increasing the population of carriers available for surface redox reactions. The metal acts as a reservoir for e^-, which can subsequently participate in multi-electron reduction in dissolved oxygen to generate $\bullet O_2^-$ radicals, while the h^+ remaining in the oxide valence band oxidize water or hydroxyl ions to produce •OH radicals. The net effect is a substantial enhancement in ROS generation and, consequently, dye degradation efficiency [161,162].

5.2.2. Plasmonic Enhancement: LSPR

Beyond the Schottky barrier effect, noble metal NPs (particularly Au and Ag) introduce an additional mechanism: LSPR. When the size and shape of metal NPs are tuned to match visible wavelengths, incident photons excite collective oscillations of conduction electrons, generating intense local electromagnetic fields and hot e^-–h^+ pairs within the metal. These plasmonic hot e^- can be injected over the Schottky barrier into the oxide conduction band, effectively enabling sub-band-gap photoactivation and extending the photocatalyst's spectral response into the visible and even NIR regions [163,164].

Ag NPs typically exhibit LSPR peaks around 400 to 440 nm [165], while Au NPs resonate at 520 to 560 nm [166], depending on size, shape, and dielectric environment. This plasmonic absorption overlaps substantially with the solar spectrum, allowing bimetallic systems to harvest visible photons that would otherwise pass through monometallic oxides without effect. The combination of Schottky electron sinking and plasmonic hot e^- injection creates a synergistic enhancement far exceeding the sum of individual contributions.

5.2.3. Charge Carrier Separation Evidence

The mechanistic claims of Schottky barrier and plasmonic enhancement are supported by multiple lines of spectroscopic and electrochemical evidence.

- TRPL: TRPL measurements provide direct quantification of charge carrier lifetimes. The increase from 5.2 ns (ZnO) to 10 ns (Ag-Ag_2O-ZnO) [159] and from 27.6 ns (ZnO) to 32.3 ns (CuFeO$_2$-ZnO) [167] demonstrates that bimetallic interfaces suppress recombination by spatially separating e^- and h^+. A longer charge-carrier lifetime directly benefits photocatalysis because photogenerated e^-'s and h^+'s must survive long enough to migrate to the catalyst surface and participate in redox reactions with adsorbed dyes, water, and dissolved oxygen; if recombination occurs first, the excitation energy is lost as photoluminescence or heat and no ROS are formed. Extending the lifetime from ~5.2 ns to ~10 ns therefore roughly doubles the probability that

carriers reach surface-active sites, increasing the steady-state population available for superoxide and hydroxyl radical generation and, consequently, the dye degradation rate [159]. These lifetime extensions correlate directly with the observed rate constant improvements, establishing a clear structure-property relationship.

- Ultrafast electron transfer: Ultrafast transient absorption spectroscopy reveals that plasmonic charge transfer occurs on femtosecond to picosecond timescales. Ag@AgCl cubic cage photocatalysts exhibited plasmon-induced e^- transfer in ≤150 fs [168], demonstrating that hot e^- injection from plasmonic metals to semiconductors is ultrafast and can outcompete competing relaxation pathways. This ultrafast transfer is critical for efficient plasmonic photocatalysis, as it ensures that hot e^- are harvested before they thermalize within the metal.
- Photoluminescence quenching: Steady-state photoluminescence spectra consistently show reduced emission intensity in bimetallic systems compared to bare oxides, indicating suppressed radiative recombination [169]. While specific photoluminescence quenching percentages are not uniformly reported across the literature, the qualitative trend is clear: metal decoration or heterojunction formation quenches photoluminescence, signaling improved charge separation.
- Photocurrent and EIS: Bimetallic photocatalysts typically exhibit increased photocurrent densities and decreased charge transfer resistance (Rct) in EIS measurements, both indicative of enhanced charge separation and transport [170]. Although the supplied literature does not consistently report standardized photocurrent values (mA/cm^2) or Rct values with units, the qualitative trends support the Schottky barrier and plasmonic enhancement mechanisms.

5.2.4. Case Studies

- Au-TiO_2 (solar-driven plasmonic photocatalysis): Au-decorated TiO_2 exemplifies the power of plasmonic enhancement. Under solar irradiation, Au-TiO_2 nanocomposites improved methyl orange degradation from 35% (bare TiO_2) to 82% [171]—a 2.3-fold increase in degradation efficiency. The improvement is attributed to Au NPs' dual role: (i) Schottky barrier formation that captures photoexcited electrons from TiO_2, and (ii) LSPR-induced hot e^- injection that enables visible-light activation. The Au LSPR peak around 520 to 560 nm overlaps with the solar spectrum's maximum intensity, allowing efficient harvesting of visible photons and subsequent charge injection into TiO_2's conduction band.
- Ag-TiO_2 (ultrahigh visible-light activity): Ag-decorated TiO_2 systems demonstrate even more dramatic enhancements. Ag@TiO_2 nanorods exhibit strong LSPR absorption at approximately 520 nm and achieve ultrahigh rhodamine B degradation rates under visible light [172]. The plasmonic hot e− generated in Ag NPs are injected into TiO_2 on sub-picosecond timescales, initiating multi-step photocatalytic decay pathways that involve both direct hot e^- driven reduction and conventional semiconductor band-edge processes. When integrated into ternary architectures, the enhancement becomes even more pronounced. A heterostructured g-C_3N_4/Ag-TiO_2 nanocomposite exhibited an apparent reaction rate constant 13.16 times that of bare TiO_2 for rhodamine B degradation under visible LED light [173]—a remarkable 13-fold improvement. This system combines the Schottky barrier at the Ag-TiO_2 interface with the type-II heterojunction between g-C_3N_4 and TiO_2, creating a cascade e^- transfer pathway that further suppresses recombination (Figure 10).

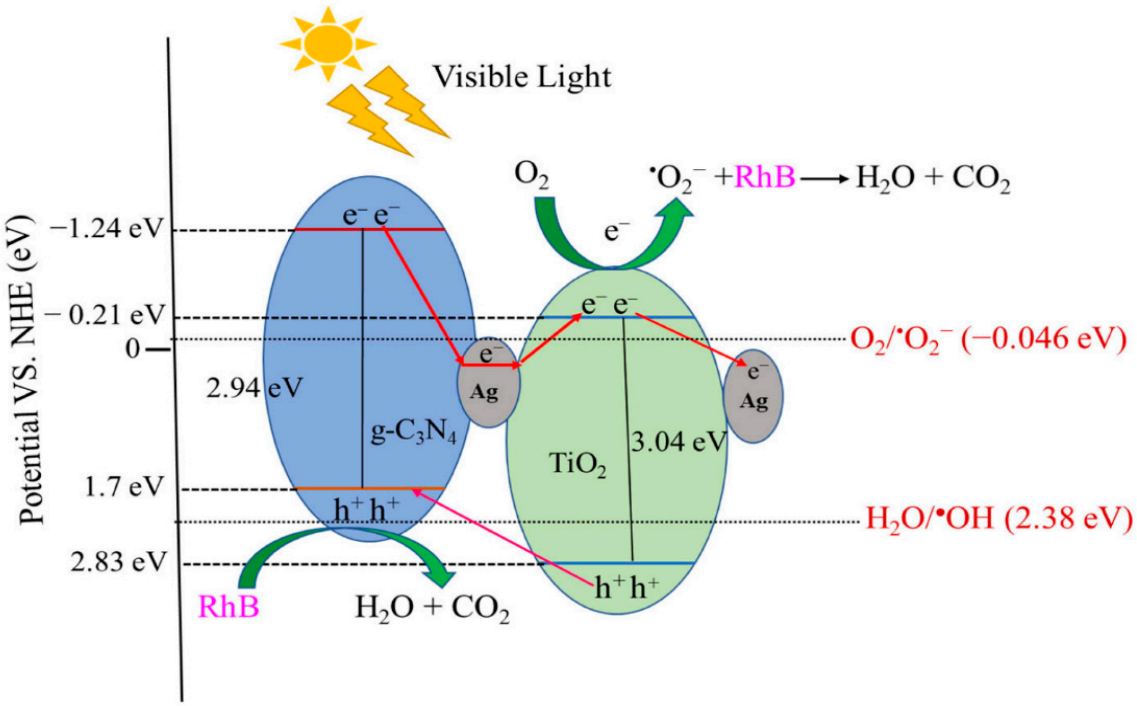


Figure 10. Schematic diagram depicting the visible-light photodegradation mechanism of the g-C_3N_4/Ag–TiO_2 heterostructure nanocomposite. Reproduced from [173].

- Pt-TiO_2 (the e^- sink paradigm): Pt, with its high work function and excellent e^- accepting properties, serves as an archetypal e^- sink in bimetallic photocatalysts. A Pt-doped TiO_2 system embedded in a MOF structure achieved 98.97% rhodamine B degradation in just 30 min [174]. The study attributes this exceptional performance to Pt NPs acting as e^- traps that prolong charge separation and facilitate multi- e^- reduction of oxygen to $\bullet O_2^-$ radicals. Scavenger studies confirmed that $\bullet O_2^-$ and conduction-band e^-'s are the dominant reactive species, consistent with the Schottky barrier mechanism directing e^-'s to Pt sites where oxygen reduction occurs.
- Ag-ZnO (dramatic rate enhancements): Ag-ZnO systems provide some of the most compelling quantitative evidence for bimetallic synergy. An Ag-Ag_2O-ZnO nanocomposite heterostructure achieved 97.3% methylene blue, 91.1% methyl orange, and 94.8% rhodamine B degradation within 60 min under visible light [159]. Critically, TRPL measurements revealed that the composite increased charge carrier lifetime from approximately 5.2 ns (pure ZnO) to approximately 10 ns—a 2-fold improvement that directly correlates with the enhanced photocatalytic performance. This lifetime extension provides quantitative evidence that the Ag-Ag_2O-ZnO interface effectively suppresses recombination.
- An even more dramatic enhancement was observed in Ag_2O-impregnated ZnO nanorods (designated ZAO25). This system achieved approximately 96.24% methylene blue degradation in 30 min with a pseudo-first-order rate constant $k \approx 0.24848$ min^{-1} [175]—approximately 26.75 times faster than pristine ZnO ($k = 0.008$ min^{-1}). The study revealed a 2-step visible-light photocatalytic mechanism involving in situ growth of metallic Ag from Ag_2O under irradiation, forming a ZnO/Ag^0/Ag_2O heterojunction structure. This dynamic interface evolution creates multiple charge transfer pathways and plasmonic hot spots, resulting in the exceptional rate enhancement.
- Au/Pd-ZnO (bimetallic plasmonic synergy): Bimetallic Au/Pd NPs supported on ZnO demonstrate that combining 2 plasmonic metals can yield synergistic effects beyond single-metal systems. Au/Pd-ZnO nanocomposites were reported to be approximately 5.4 times more efficient at degrading methylene blue than pure ZnO under

visible light irradiation [176]. The dual-metal system benefits from complementary LSPR peaks (Au at ~520 to 560 nm, Pd with weaker but broader plasmonic response) and potentially enhanced Schottky barrier effects due to the bimetallic alloy's modified work function. This study illustrates that even within bimetallic systems, compositional tuning can optimize charge separation and light harvesting.

- $CuFeO_2$-ZnO (oxide-oxide heterojunctions): Not all bimetallic enhancements require noble metals; oxide-oxide heterojunctions can also dramatically improve performance through band alignment and built-in electric fields. A $CuFeO_2$-ZnO heterostructure achieved 100% methylene blue degradation with a pseudo-first-order rate constant $k = 0.272 \pm 0.002$ min^{-1} under sunlight [167]—approximately 16 times faster than bare ZnO. TRPL analysis revealed charge carrier lifetimes of 32.3 ns for the heterostructure compared to 27.6 ns for ZnO and only 0.85 ns for $CuFeO_2$, indicating that the interface suppresses recombination in both components. The p-type $CuFeO_2$ and n-type ZnO form a p-n heterojunction with a built-in electric field that drives e^-–h^+ separation, analogous to the Schottky barrier mechanism but achieved through oxide band alignment rather than metal-semiconductor contact.
- ZnO/$CuMoO_4$ (moderate heterojunction enhancement): A ZnO/$CuMoO_4$ composite demonstrated 93.4% dye degradation in 120 min with $k = 0.025$ min^{-1} [158]—a 3-fold improvement over pristine ZnO ($k = 0.008$ min^{-1}). While more modest than the plasmonic systems, this oxide-oxide heterojunction illustrates that even non-plasmonic bimetallic interfaces can significantly enhance performance through improved charge separation. The type-II band alignment between ZnO and $CuMoO_4$ facilitates e^- transfer from $CuMoO_4$ to ZnO and h^+ transfer in the opposite direction, spatially separating charge carriers and reducing recombination.
- Other metal oxide-metal oxide heterojunctions: Additional oxide-oxide bimetallic systems reported in the literature include TiO_2-ZnO, ZnO-CuO, TiO_2-WO_3, and $BiVO_4$-WO_3 heterojunctions. These systems leverage type-II or Z-scheme band alignment to drive charge separation. For example, SnO_2/TiO_2 composites exhibited $k \approx 0.0327$ min^{-1} [157], while CuO/TiO_2 reached $k \approx 0.0341$ min^{-1} [157]—modest but measurable improvements over bare TiO_2 ($k = 0.0141$ min^{-1}). These results underscore that interface engineering, whether through metal-semiconductor Schottky barriers or oxide-oxide heterojunctions, is the key to overcoming monometallic limitations.

In summary, the bimetallic interface thus represents a transformative advance over monometallic systems, simultaneously addressing both the band gap and recombination limitations through Schottky barriers and plasmonic effects.

5.3. Trimetallic and Tetrametallic: Cascade Mechanisms and Multi-Plasmon Effects

5.3.1. Broadening Light Absorption: Multi-Plasmon Effects

While bimetallic systems successfully extend light absorption into the visible range, trimetallic and tetrametallic architectures offer the potential for even broader spectral coverage through multi-plasmon effects. The addition of a second plasmonic metal (e.g., Pt to Au-TiO_2, or Au to Ag-ZnO) creates multiple LSPR peaks that can span the visible and NIR regions. Each metal contributes its characteristic plasmon resonance, and in some cases, plasmonic coupling between adjacent metal NPs generates new hybrid modes with enhanced local field intensities.

For example, a ternary NiO/Ag/TiO_2 system achieved 93.15% methylene blue degradation within 60 min under visible light [110]. While NiO itself is not plasmonic, its p-type character creates a p-n heterojunction with n-type TiO_2, and the Ag NPs provide plasmonic enhancement. The combination of heterojunction-driven charge separation and

plasmonic hot e^- injection results in superior performance compared to binary Ag/TiO_2 or NiO/TiO_2 systems.

Similarly, $Ag@Cu_xO/ZnO$ ternary heterostructures demonstrated enhanced textile effluent degradation under sunlight [177]. These systems combine the plasmonic effects of Ag or Au with the p-n heterojunction between p-type Cu_xO and n-type ZnO, creating a dual-mechanism enhancement. The plasmonic metal extends light absorption into the visible range, while the p-n junction provides a built-in electric field for charge separation. This synergy enables efficient degradation of complex industrial effluents containing multiple dyes and organic pollutants.

5.3.2. Multi-Step Charge Transfer: The 'e^- Highway'

The defining advantage of trimetallic and tetrametallic systems is the creation of cascade e^- transfer pathways—'e^- highways' that direct charge carriers through multiple interfaces in a stepwise manner, drastically reducing the probability of recombination (Figure 11) [178]. In a ternary system, e^-'s can be transferred sequentially from 1 component to the next, with each interface acting as a checkpoint that prevents back-transfer and recombination.

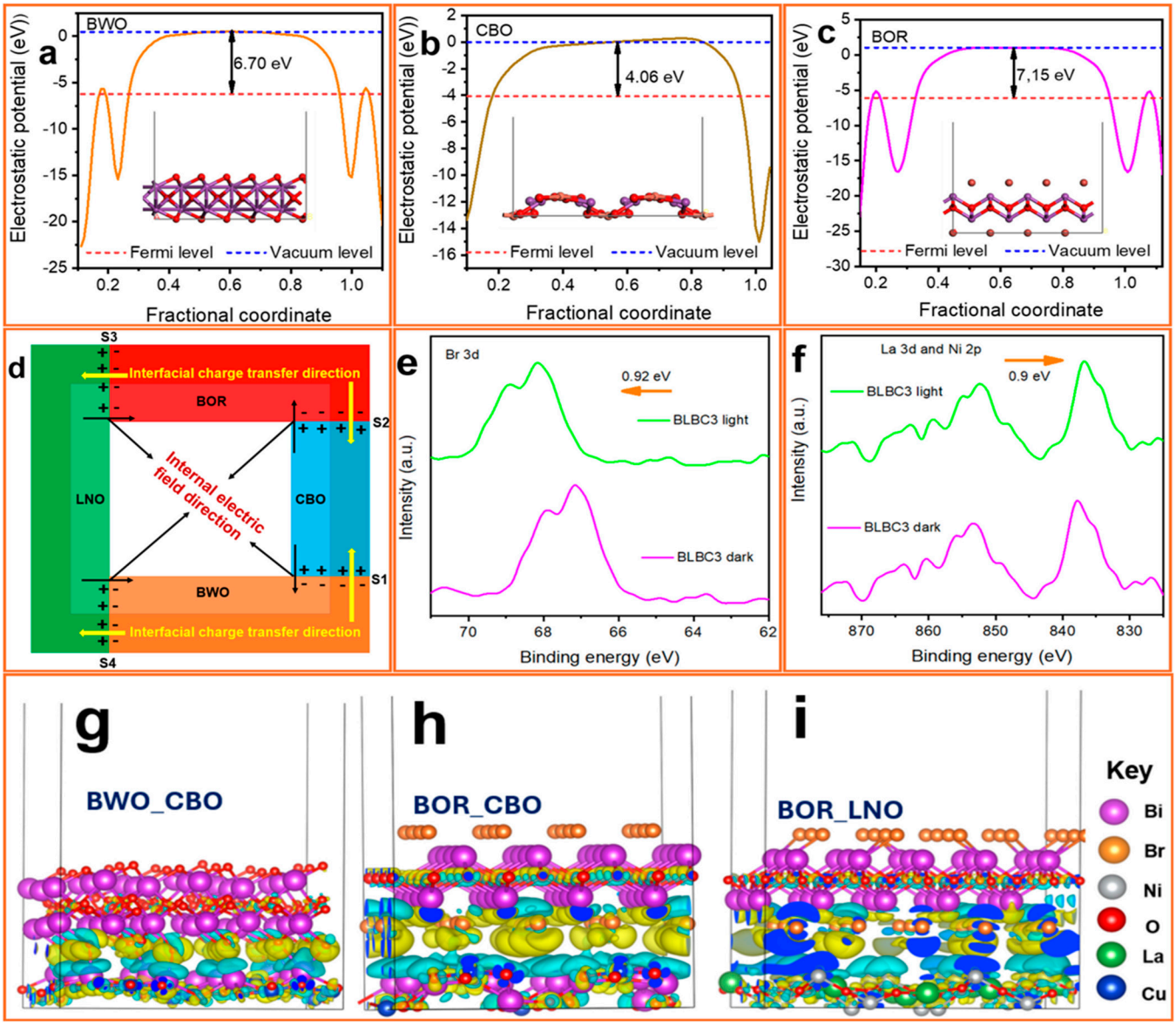


Figure 11. The analysis of the band structure and charge transfer is presented. The work functions, calculated using Density Functional Theory, are shown for (**a**) Pristine Bi_2WO_6 (BWO), (**b**) CBO, and (**c**) BOR. Diagram (**d**) depicts the charge transfer pathway within the quadruple S-scheme heterojunction from a top view. High-resolution XPS spectra are provided for (**e**) Br 3d, (**f**) La 3d and Ni 2p. Finally, 3D charge density difference diagrams are illustrated for the (**g**) BWO-CBO, (**h**) BOR-CBO, and (**i**) BOR-LNO interfaces; in these diagrams, yellow regions indicate electron accumulation, light blue regions signify electron depletion, and navy-blue regions represent holes. Reproduced from [178].

A compelling example is the Fe_3O_4@MoS_2@Au nanocomposite, which achieved 98.95% methylene blue degradation under green light (540 nm) with a pseudo-first-order rate constant $k = 3.8 \times 10^{-3}$ min^{-1} [179]—2.7 times faster than Fe_3O_4@MoS_2 without Au. The ternary architecture creates a cascade: (i) Au NPs generate plasmonic hot e^-'s under green light, (ii) these hot e^-'s are injected into the MoS_2 conduction band, and (iii) e^-'s subsequently transfer to Fe_3O_4, which also provides magnetic separability for catalyst recovery. Each step in this cascade is energetically favorable, and the spatial separation across three components minimizes recombination. The result is efficient visible-light-driven degradation at wavelengths (540 nm) where monometallic oxides are completely inactive.

Graphene and rGO are frequently employed as e^- conducting supports in trimetallic systems, serving as 'e^- highways' that facilitate rapid e^- transport away from the semiconductor [180]. Metal-metal oxide NPs deposited on graphene sheets benefit from graphene's exceptional electron mobility (>10,000 cm_2/Vs), which allows photoexcited e^-'s to delocalize across the extended π-conjugated network, further suppressing recombination. Graphene acts as an e^- sink and transport medium, complementing the Schottky barriers and plasmonic effects of the metal-oxide interfaces [180].

5.3.3. Enhanced Surface-Active Sites and Adsorption Capacity

Trimetallic and tetrametallic surfaces offer a greater diversity of active sites compared to bimetallic systems, potentially improving adsorption and catalytic turnover for complex dye molecules [35]. Industrial textile effluents often contain mixtures of dyes with varying chemical structures (azo dyes, triphenylmethane dyes, anthraquinone dyes), each requiring different adsorption and degradation pathways. Multi-metal surfaces provide a heterogeneous catalytic environment with multiple types of active sites—metal NPs for e^- mediated reduction, oxide surfaces for h^+-mediated oxidation, and interfacial sites for cooperative redox processes.

The Ag@Cu_xO/ZnO, for instance, demonstrated effective degradation of industrial textile effluents containing multiple dyes [177]. The presence of 3 distinct components (noble metal, copper oxide, zinc oxide) creates a versatile catalytic surface capable of adsorbing and degrading a broad range of organic pollutants. This versatility is particularly valuable for real-world applications, where wastewater composition is complex and variable.

5.3.4. Reusability and Stability

A critical practical consideration for photocatalysts is their stability and reusability over multiple degradation cycles. Trimetallic and tetrametallic systems often exhibit excellent cycle stability, retaining >97% of their initial activity after 4 to 5 cycles. For example, the Ag-Ag_2O-ZnO composite maintained stable performance over 5 cycles [159], while the $CuFeO_2$-ZnO heterostructure retained approximately 97% activity after 4 cycles [167].

The enhanced stability of multi-component systems may arise from several factors: (i) the presence of multiple interfaces distributes mechanical and chemical stress, reducing the likelihood of structural degradation; (ii) magnetic components (e.g., Fe_3O_4) enable

facile magnetic separation and recovery, minimizing catalyst loss; and (iii) the cascade charge transfer mechanisms reduce the accumulation of reactive intermediates that can cause photocorrosion. The Fe_3O_4@MoS_2@Au system, for instance, benefits from magnetic separability, allowing rapid recovery and reuse without centrifugation or filtration [179].

5.4. Comparative Kinetic Analysis: Quantifying the Benefits of Increasing Complexity

The progression from monometallic to bimetallic to trimetallic systems is best illustrated through direct kinetic comparisons for the same dye under similar conditions. For ZnO-based systems degrading methylene blue: (i) Monometallic ZnO: k = 0.008 min^{-1} (baseline) [158]; bimetallic ZnO/$CuMoO_4$: k = 0.025 min^{-1} (3× enhancement) [158]; bimetallic $CuFeO_2$-ZnO: k = 0.272 ± 0.002 min^{-1} (16× enhancement) [167]; bimetallic Ag_2O-ZnO (ZAO25): k ≈ 0.24848 min^{-1} (26.75× enhancement) [175]; bimetallic Au/Pd-ZnO: 5.4× more efficient than ZnO [176].

For TiO_2-based systems degrading rhodamine B: (i) Monometallic TiO_2: k = 0.0141 min^{-1} (baseline) [157]; bimetallic Pt-MOF/TiO_2: 98.97% degradation in 30 min [174]; ternary g-C_3N_4/Ag-TiO_2: 13.16× rate enhancement vs. TiO_2 [173]. These comparisons reveal a clear trend: bimetallic systems consistently outperform monometallic oxides by factors of 3× to 26.75×, with the highest enhancements observed in plasmonic Ag-ZnO systems. Trimetallic systems (e.g., g-C_3N_4/Ag-TiO_2) can achieve even greater enhancements (13.16×) through cascade charge transfer mechanisms [173].

The fold-improvement progression from monometallic to bimetallic systems is dramatic: Modest heterojunctions (oxide-oxide): 3× improvement (ZnO/$CuMoO_4$) [158], Schottky barrier systems (metal-oxide): 5 to 16× improvement (Au/Pd-ZnO [176], $CuFeO_2$-ZnO [167]), and plasmonic systems (noble metal-oxide): 13 to 27× improvement (Ag_2O-ZnO [175], g-C_3N_4/Ag-TiO_2) [173]. The highest enhancements are achieved when Schottky barriers and plasmonic effects operate synergistically, as in the Ag_2O-ZnO system (26.75×) [175]. This system benefits from both the Schottky barrier at the Ag-ZnO interface and the LSPR of Ag NPs, plus the p-n heterojunction between p-type Ag_2O and n-type ZnO. The combination of 3 charge-separation mechanisms (Schottky, plasmonic, p-n junction) yields exceptional performance.

Trimetallic systems show further improvements, though the incremental gains are more modest. The Fe_3O_4@MoS_2@Au system achieved a 2.7× enhancement over the bimetallic Fe_3O_4@MoS_2 [179], while the NiO/Ag/TiO_2 ternary outperformed binary Ag/TiO_2 and NiO/TiO_2 systems [110]. These results suggest that while trimetallic systems do provide additional benefits, the gains are not always proportional to the added complexity.

A critical distinction must be drawn between dye decolorization and true mineralization, because the 2 are frequently conflated in the photocatalytic literature summarized in Table 5. Decolorization reflects only the disappearance of the chromophore (typically via cleavage of azo (N=N), triphenylmethane, or anthraquinone chromogenic groups) and is measured spectrophotometrically as the decline in absorbance at λ_{max}; it therefore overestimates treatment efficacy, since colorless aromatic intermediates (e.g., substituted anilines, phenols, naphthalenols, and sulfonated aromatic amines) can persist and, in several cases, be more toxic or mutagenic than the parent dye. Mineralization, by contrast, requires complete conversion of organic carbon to carbon dioxide and water (with heteroatoms released as NO_3^-, SO_4^{2-}, or NH_4^+) and can only be verified by total organic carbon (TOC) removal, chemical oxygen demand (COD) abatement, or ion chromatography, supported by intermediate identification via chromatography techniques and by toxicity assessment of the treated solution (e.g., Microtox, Daphnia, or zebrafish assays). Within the studies tabulated here, only a minority report TOC or COD removal alongside decolorization (e.g., Ni/g-C_3N_4/ZnO, ~67.45% TOC removal, and NiO/Ag/TiO_2, ~92.91% TOC removal [105,110]), and the high decolorization percentages (90 to 100%) reported for most

systems therefore cannot be equated with detoxification. This gap has direct implications for real effluent treatment: partially degraded dye solutions may retain aromatic amine by-products that are carcinogenic or mutagenic, and the ecotoxicological studies discussed in Section 6.2 show that photocatalyst-derived transformation products and leached metal ions can themselves exert residual toxicity [181,182]. Accordingly, future benchmarking of heterostructured photocatalysts should report decolorization, TOC/COD mineralization, identified intermediates and degradation pathways, and post-treatment toxicity in parallel (ideally in real wastewater matrices rather than model dye solutions) so that catalytic performance is evaluated in terms of environmental safety rather than color removal alone [183–185].

In summary, the interface (whether a Schottky barrier, plasmonic contact, or heterojunction) is the key to unlocking the photocatalytic potential of metal oxide semiconductors. By engineering interfaces that suppress recombination and extend light absorption, researchers have transformed photocatalytic dye degradation from a laboratory curiosity into a viable technology for industrial wastewater treatment. The challenge moving forward is to optimize these interfaces for maximum performance while maintaining synthetic simplicity, cost-effectiveness, and long-term stability.

Table 5. Comprehensive comparison of bi-, tri-, and tetra-heterostructures for dye degradation.

Heterostructure	Dye(s) Tested	Degradation (%)	Time (min)	Catalyst DOSE	Dye concentration	pH	Light Source	Rate Constant (min^{-1})	Key Outcomes	Ref.
Bi-component heterostructures										
B-ZnO/TiO_2 (5% B doping)	Methylene blue	95	15	0.6 g/L	15 mg/L	11	Natural sunlight	0.0319	$•O_2^-$ and •OH main ROS; reusable 5 cycles	[56]
ZnO-Bi_2O_3 (10 mol% Bi_2O_3)	Reactive orange 16	48.5	200	1.0 g/L	100 mg/L	7	UV + H_2O_2	0.008	Synergistic effect, 300% and 33% higher than individual oxides	[57]
Mn_3O_4@ZnO (1:3 ratio)	Methylene blue, methyl orange, malachite green	94.59, 89.99, 97.40	240, 240, 70	0.05 g/L	1.87×10^{-5} M, 2.44×10^{-5} M, 5.48×10^{-5} M	-	UV light	0.00851, 0.00458, 0.0301	Mn_3O_4 as a co-catalyst enhances charge separation	[8]
$Fe_{0.5}Mn_{0.5}Co_2O_4$/Fe_2O_3	Rhodamine B, Congo red	100 (both)	50	1.0 g/L	20 mg/L	8, 3	UV + H_2O_2	0.0414, 0.0342	reusable 4 cycles	[62]
$Mn_{0.5}Zn_{0.5}Fe_2O_4$/Fe_2O_3	Rhodamine B, Congo red	100 (both)	50	1.0 g/L	20 mg/L	8, 3	UV + H_2O_2	0.0475, 0.0303	reusable 4 cycles	[62]
α-Fe_2O_3/ZnTe	Congo red, methyl orange, methylene blue	97.9, 84, 73	60	0.2 g/L	100 ppm	-	Light (>200 nm)	-	Degradation efficiency was improved in comparison to bare hematite	[58]
ZnO-SnO_2 (1:1 molar ratio)	Methylene blue	82.45	120	0.1 g/L	10 ppm	-	Visible light	0.0072	-	[186]
$Ni_{1-x}Mn_xWO_4$ (Mn-doped)	Methyl orange	99.06	70	0.5 g/L	50 ppm	5	Visible light	0.067	Total organic content removal:	[61]

									67.45%; reusable for 6 cycles	
Tri-component heterostructures										
Mn/g-C_3N_4/ZnO (Mn/50GZ)	Eriochrome black T, methyl orange	100, 98	50, 70	2.0 g/L	10 mg/L	-	Sunlight	0.027 (EBT)	Reusable over 5 cycles	[105]
Ni/g-C_3N_4/ZnO (Ni/60GZ)	Eriochrome black T, methyl orange	100, 98	60, 90	2.0 g/L	10 mg/L	-	Sunlight	0.022 (EBT)	Reusable over 5 cycles	[105]
NiO/Ag/TiO_2 (1% loading)	Methylene blue	93.15	60	1.0 g/L	5 mg/L	-	Visible light	0.0312	Total organic content removal 92.91%; reusable for 3 cycles	[110]
α-Fe_2O_3-CeO_2@Au	Rose Bengal	88.9	120	50 mg/L	20 mg/L	7	Visible light	0.0179	Reusable 4 cycles	[111]
Cu_4O_3/ZrO_2/TiO_2	Everzol yellow 3RS	91.41	100	1.0 g/L	40 ppm	3	Sunlight	-	Reusable 4 cycles with 93% efficiency	[107]
Fe/Cu/Ag (5:1:0.2)	Methyl orange	100	1	0.2 g/L	10 mg/L	3 to 4.5	RT	0.6663	Complete degradation in 1 min	[15]
Tetra-component heterostructures										
Ag-$AgVO_3$/$Zn_{0.5}Mn_{0.5}Fe_2O_4$	Rhodamine B	99.9	240	1.0 g/L	20 mg/L	2	Visible light + H_2O_2	-	High chemical oxygen demand	[104]
CuO/ZnO/CQDs@PAN	Methylene blue	99.56	240	2.5 g/L	10 mg/L	-	Natural sunlight	-	Reusable with 96.55% after 3 cycles	[106]
Ag_3VO_4/$Zn_3(VO_4)_2$/$Zn_2V_2O_7$/ZnO (50% Ag_3VO_4/Zn-V-O)	Rhodmine B, methyl orange, orange II, methylene blue	95%, 50%, 78%, 100%	25 to 300 (varies by dye)	30 mg/50 mL	10 mg/L	6.0 to 8.0	Solar light	-	•OH and O_2^- are main active species	[119]
ZnO/SnO_2/CeO_2/CuO (ZSCC)	Methylene blue	91%	120	-	-	-	Visible light	-	91% vs. 78 to 88% for individual oxides	[120]
Ag/BiOBr@Bi_2MoO_6/ZnO/g-C_3N_4	Direct red 23	81%	110	15 mg/100 mL	10 mg/L	7.0	Near-visible/UV	0.0158	Molecular dynamics simulations showed an adsorption energy of −57.3 kcal/mol·atom	[121]
CeO_2/Co_3O_4/Ag/Ag_3PO_4	Methylene blue	93%	80	1 g/L	4 ppm	9.0 (opt.)	Blue LED	0.0349	4.8× faster than CeO_2/Co_3O_4; 4-cycle stability	[122]
ZnO-PbO-CdO-CuO (ZPCC)	Fast green, rose Bengal	93%, 94%	120	30 mg/50 mL	20 mg/L	-	Sunlight	0.046, 0.051	*Caenorhabditis elegans* toxicity study showed that degraded dyes are non-toxic	[123]

6. Toxicity, Stability, and Environmental Considerations

6.1. Biocompatibility and Complexity-Dependent Toxicity

The biocompatibility of metal-metal oxide heterostructures exhibits a complex relationship with structural complexity, as evidenced by extensive in vitro and in vivo studies. Monometallic systems often demonstrate concentration-dependent cytotoxicity, with ZnO NPs showing significant toxicity in human dermal fibroblast cells through mechanisms involving free radical formation and zinc ion release [187]. In aquatic toxicity assessments using *Oreochromis mossambicus* fish and Swiss Albino mice, pristine ZnO NPs exhibited substantial toxicity, though modification with divalent ions (Mg, Ca, Sr, Ba) significantly reduced these effects, with ZnCaO nanomaterials demonstrating the lowest toxicity attributed to Ca^{2+} ions enhancing body growth metabolism [188].

Bimetallic heterostructures present a nuanced toxicity profile. Ag-CuO nanocomposites synthesized via green methods exhibited outstanding antiproliferative activity against A549 lung cancer cells with an IC_{50} of 2.8 ± 0.05 μg/mL, while simultaneously demonstrating dose- and time-dependent growth reduction in marine microalgae *Tetraselmis suecica*, indicating potential ecotoxicological concerns [189]. Similarly, Ag-ZnO/AgO nanocomposites showed concentration-dependent cytotoxicity in HaCaT keratinocytes, with cell viability decreasing to 60% at 100 μg/mL after 24 h, while in vivo zebrafish embryo studies revealed 100% mortality at 100 μg/mL and developmental abnormalities including pericardial edema and spinal curvature at sublethal concentrations [181].

Trimetallic and tetrametallic systems generally exhibit enhanced biocompatibility when properly engineered. The trimetallic CuO/Ag/NiO composite supported on silica NPs demonstrated improved stability and reduced toxicity compared to individual metal oxides, attributed to synergistic interactions and the protective silica matrix [190]. However, complexity does not universally guarantee safety; multicomponent TiO_2-based nanomaterials decorated with Ag, Au, Pt, and Pd showed varying toxicity profiles, with Ag-containing formulations exhibiting the highest toxicity due to Ag^+ ion release, while Au and Pt modifications demonstrated superior biocompatibility [191]. A structure-activity assessment of multicomponent metal oxide nanomaterials revealed that toxicity depends not solely on compositional complexity but on specific metal combinations, surface chemistry, and ion release kinetics [192].

The magnetic α-Fe_2O_3/Fe_3O_4 heterostructure nanorods demonstrated excellent biocompatibility with LO_2 and HepG2 cells, maintaining cell viability above 80% at concentrations up to 200 μg/mL after 24 h, illustrating that iron oxide-based bimetallic systems can achieve favorable biocompatibility profiles [193]. In contrast, the trimetallic Fe-Mn-Sn oxide heterostructure, while exhibiting exceptional catalytic performance, requires careful toxicity assessment given the presence of multiple metal species with distinct biological interactions [194].

6.2. Metal Ion Leaching and Ecotoxicological Impacts

Metal ion leaching represents a critical environmental and health concern for heterostructures, with dissolution kinetics varying significantly across different metal oxide systems. CuO and CoO NPs exhibited dramatic dissolution behavior, with CuO and CoO showing over 77.7% dissolution in artificial lysosomal fluid (pH 5.5) after 48 h, while Co_3O_4, NiO, and TiO_2 NPs demonstrated substantially lower dissolution rates of 0.2%, 2.0%, and 0.3%, respectively [195]. This pH-dependent dissolution is particularly relevant for biological systems, where acidic microenvironments in lysosomes and endosomes can accelerate ion release. In neutral phosphate-buffered saline, all tested NPs showed less

than 5.4% dissolution, highlighting the importance of environmental pH in governing leaching behavior [195].

Ag ion leaching from Ag-containing heterostructures poses significant ecotoxicological risks. Uncoated Ag/Fe_2O_3 NPs exhibited Ag dissolution of 7 ± 1.7% (ion-selective electrode) and 8.6 ± 0.5% (diffusive gradients in thin films technique), while silica-coated counterparts showed reduced leaching of 2.8 ± 1.4% and 5.4 ± 0.5%, respectively, demonstrating that surface passivation can substantially mitigate ion release [196]. The ecotoxicological consequences of Ag leaching are exemplified by Ag-CuO nanocomposites, which induced dose- and time-dependent growth inhibition in marine microalgae *T. suecica*, with microalgae serving as sensitive bio-indicators of environmental contamination [189].

Zn ion release from ZnO-based heterostructures significantly impacts aquatic ecosystems. Released Zn^{2+} ions can profoundly alter water properties and directly influence underwater ecosystems, particularly fish populations, with accumulation in fish tissues posing health risks to both aquatic organisms and humans through bioaccumulation in the food chain [188]. The incorporation of divalent ions such as Ca^{2+} into ZnO lattices reduced toxicity by modulating Zn ion release kinetics and providing beneficial metabolic effects, with ZnCaO nanomaterials demonstrating lower toxicity to fish and mice compared to pristine ZnO [188].

The skin sensitization potential of metal ions released from oxide NPs has been quantitatively assessed using the KeratinoSens™ assay. CuO and CoO NPs induced luciferase activity with $EC_{1.5}$ values of 1.38 and 316.57 μM, respectively, classifying them as sensitizers, with $CuCl_2$ and $CoCl_2$ showing similar dose-dependent effects, confirming that metal ion release is the major factor triggering sensitization responses [195]. In vivo studies using BALB/c mice exposed to metal oxide NPs (CoO, Co_3O_4, CuO, NiO, TiO_2) at 25%, 50%, and 100% concentrations resulted in stimulation index values less than 2.7, indicating moderate sensitization potential [195].

The environmental fate of leached metal ions extends beyond immediate toxicity. Ag-ZnO/AgO nanocomposites demonstrated that photocatalytic degradation products, while effectively mineralizing organic pollutants, must be assessed for residual toxicity, as the NPs themselves exhibited 100% mortality in zebrafish embryos at 100 μg/mL, raising concerns about the environmental safety of both the nanomaterials and their transformation products [181]. The photocatalytic degradation of 3-methyl-4-nitrophenol over Ag/AgCl-decorated/[MOYI]-coated/ZnO nanostructures included comprehensive in vivo toxicity assessment of photoproducts, revealing that while parent pollutants were effectively degraded, the nanomaterial-solution system required careful monitoring for residual toxicity [182].

Beyond catalytic performance, the practical environmental applicability of multicomponent heterostructures is constrained by 3 interconnected drawbacks that must be addressed before translation. First, the cost and scalability of reproducible multi-step synthesis remain prohibitive: mask-assisted growth, total-synthesis coupling, and thermal decomposition–etching are labor-intensive, low-yield, and difficult to scale beyond laboratory quantities [21,31,33]. Second, metal-ion leaching poses ecotoxicological risks, since CuO and CoO dissolve by over 77.7% in acidic lysosomal fluid within 48 h [195], Ag leaching from Ag/Fe_2O_3 is only partially suppressed by silica coating (~7 to 8.6% reduced to ~2.8 to 5.4%) [196], and released Zn^{2+} can bioaccumulate through aquatic food chains [188]. Third, long-term photocorrosion threatens operational durability, as pristine ZnO undergoes self-oxidation under UV and acidic conditions [187,188], and even protective architectures such as triple-shelled Ag@Fe_3O_4@SiO_2@TiO_2 are required to prevent Ag photocorrosion [197]. These risks are interdependent—protective shells that mitigate leaching and photocorrosion add synthesis steps and cost, while higher compositional complexity

intended to improve performance simultaneously increases the number of leachable metal species. Consequently, environmental deployment of these materials requires life-cycle and ecotoxicological assessment alongside catalytic benchmarking, rather than performance optimization alone.

6.3. Stability and Photocorrosion Behavior

Photocorrosion represents a fundamental challenge for metal oxide photocatalysts, with monometallic oxides exhibiting pronounced susceptibility under operational conditions. ZnO NPs are particularly vulnerable to photocorrosion in acidic environments, where photogenerated holes oxidize the ZnO lattice itself rather than target pollutants, leading to Zn ion release and structural degradation [188]. This self-oxidation process is accelerated under UV irradiation and acidic pH conditions, limiting the long-term stability and reusability of pristine ZnO photocatalysts [187].

Noble metal decoration significantly enhances photocorrosion resistance through multiple mechanisms. The Au-Fe_3O_4 heterostructure demonstrated exceptional stability across multiple catalytic cycles, with the Au component serving as an e^- sink that facilitates charge separation and reduces h^+ accumulation on the oxide surface, thereby minimizing self-oxidation [198]. Similarly, M@Cu_xO/ZnO (M = Ag, Au) heterostructured nanocomposites exhibited enhanced photocatalytic stability under sunlight, with the noble metal components preventing photocorrosion through efficient e^- transfer and surface passivation effects [177]. The fine structural tuning of metal-metal oxide heterostructures, including control over metal cluster size and distribution, proved critical for optimal photocatalytic enhancement and stability, with well-dispersed noble metal NPs providing superior protection against photocorrosion compared to aggregated structures (Figure 12) [199].

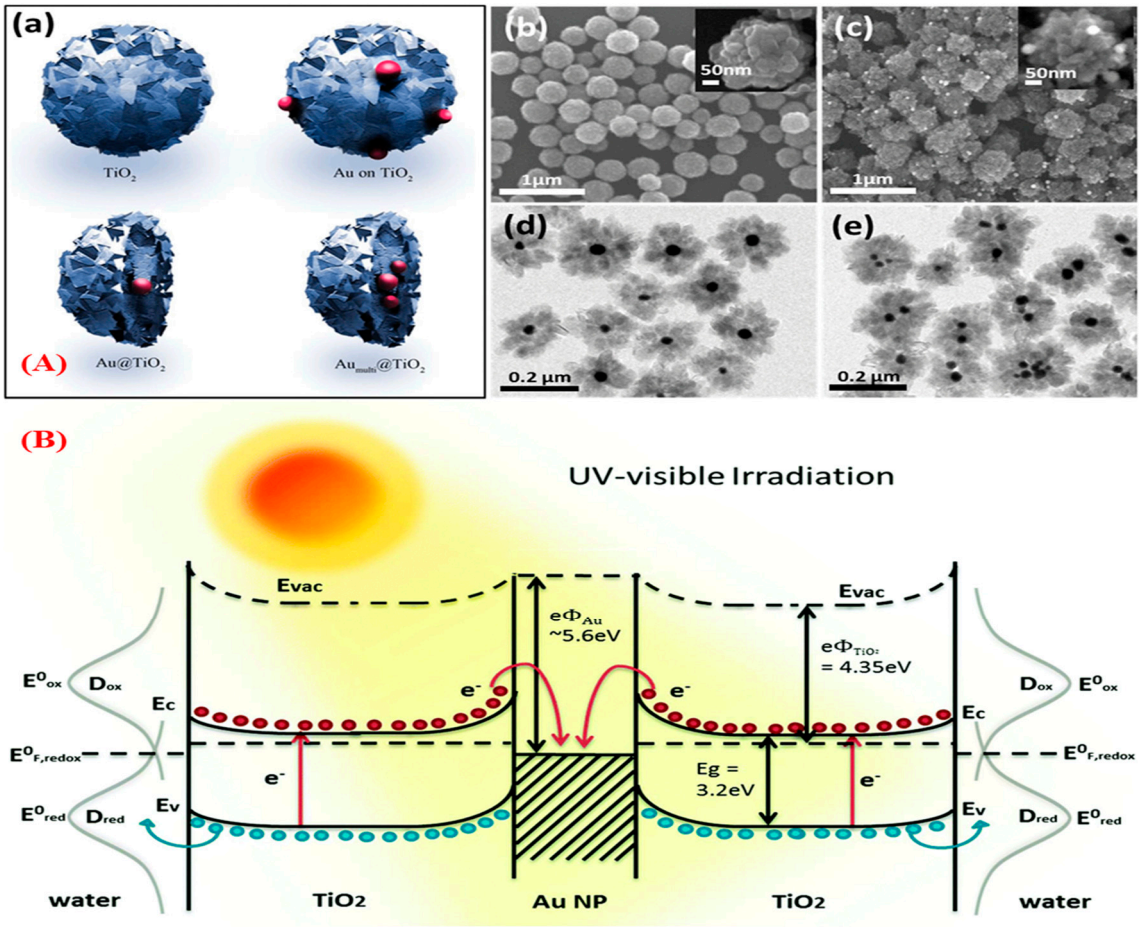


Figure 12. (**A**) (**a**) illustrates 4 distinct configurations of TiO_2 nanospheres, synthesized either with or without Au NPs, and featuring Au NPs either on the surface or confined within the structure. SEM images show (**b**) plain TiO_2 nanospheres and (**c**) TiO_2 nanospheres with surface-loaded Au NPs. The insets provide higher magnification views of each sample. TEM images in (**d**–**e**) reveal Au@TiO_2 structures (where Au NPs are spatially confined) displaying both single and multiple cores. (**B**) Proposed mechanism for photocatalysis and the corresponding energy band diagram of Au@TiO_2 nanospheres under sunlight exposure. Reproduced from [199].

Shell passivation strategies offer robust protection against photocorrosion in complex heterostructures. The triple-shelled Ag@Fe_3O_4@SiO_2@TiO_2 photocatalyst demonstrated remarkable stability, maintaining high photocatalytic activity for degradation of organic pollutants and reduction in hexavalent chromium ions across multiple cycles, with the silica interlayer preventing direct contact between the Ag core and the TiO_2 shell, thereby eliminating Ag photocorrosion [197]. The ternary $BaTiO_3$/MoO_3/Ag heterostructure exhibited highly efficient and reusable photocatalytic performance, with the multi-component architecture providing mutual protection against photocorrosion through synergistic charge transfer pathways [200].

Core–shell architectures with protective oxide shells demonstrate superior stability compared to bare metal oxides. The Au-embedded CuO_x-CeO_2 core/shell nanospheres exhibited exceptional sinter-resistance and stability, with the CeO_2 shell preventing sintering of the Au and CuO components even under harsh reaction conditions, while maintaining high catalytic activity [201]. The Pd@CeO_2 hollow core–shell nanocatalyst achieved aggregation- and leaching-resistant properties, with the CeO_2 shell providing a protective barrier that prevented Pd leaching and nanoparticle aggregation across multiple catalytic cycles, demonstrating the effectiveness of shell passivation in enhancing long-term stability [202].

Zeta potential measurements provide quantitative indicators of colloidal stability and resistance to aggregation. Ag-CuO nanocomposites exhibited remarkable stability at −21.5 mV, indicating sufficient electrostatic repulsion to prevent agglomeration in aqueous media [189]. The CuO-Co_3O_4 bimetallic system showed zeta potential values of −24.2 mV for CuO, 46.6 mV for Co_3O_4, and −38.8 mV for the composite, suggesting overall stability and resistance to aggregation, with the composite exhibiting enhanced stability compared to individual components [203]. XRD analysis of recycled catalysts confirmed structural stability, with no change in peak positions after multiple catalytic cycles, indicating preservation of crystalline structure and absence of phase transformations [203].

6.4. Reusability and Recyclability in Catalytic Applications

Quantitative reusability data reveal significant variations in catalytic stability across different heterostructure complexities. The Au-Fe_3O_4 bifunctional heterostructure demonstrated excellent magnetic recyclability for nitrophenol reduction, with the magnetic Fe_3O_4 component enabling facile separation via external magnetic fields [198]. The triple-shelled Ag@Fe_3O_4@SiO_2@TiO_2 photocatalyst exhibited highly efficient and recyclable performance, maintaining robust activity across multiple cycles for both organic pollutant degradation and hexavalent chromium reduction, with the multi-layered architecture preventing catalyst deactivation [197].

Bimetallic systems show variable reusability profiles depending on composition and synthesis methods. The Cu@ZnO and Ag@ZnO nanocomposites synthesized via green methods demonstrated ultra-rapid catalytic effects with recyclable properties, though the study emphasized rapid kinetics over long-term cycling stability [204]. The CuO-Co_3O_4 bimetallic NPs underwent 4 catalytic cycles for 4-nitrophenol reduction, with conversion percentage decreasing slightly from 88.99% to 85.02% after the 4th cycle, representing a

4.5% activity loss and demonstrating good retention of catalytic performance. Recovery was achieved through centrifugation and thorough washing with deionized water and ethanol, indicating straightforward regeneration procedures [203].

Trimetallic systems with magnetic components offer superior recyclability through magnetic separation. The trimetallic CuO/Ag/NiO composite supported on silica NPs demonstrated enhanced stability and reusability for hydrogen production applications, with the silica support providing structural integrity and preventing metal leaching [190]. The trimetallic Fe-Mn-Sn oxide heterostructure derived from MOFs exhibited exceptional catalytic degradation of organic pollutants with notable stability across multiple cycles, attributed to the synergistic interactions between the 3 metal oxide components and the hierarchical porous structure inherited from the MOF precursor [194].

The ternary $BaTiO_3/MoO_3/Ag$ heterostructure demonstrated highly efficient and reusable photocatalytic applications, with the multi-component system maintaining activity across multiple cycles without significant degradation [200]. The Ag-decorated and silica-capped magnetite NPs ($Ag@SiO_2@Fe_3O_4$) exhibited effective antibacterial activity with excellent reusability, as the magnetic core enabled rapid separation and the Si-Ag architecture remained stable across multiple use cycles [205].

Magnetic separation emerges as the preferred recovery method for heterostructures containing magnetic components. The magnetic α-Fe_2O_3/Fe_3O_4 heterostructure nanorods can be readily separated from reaction media using external magnetic fields, facilitating reuse without significant material loss [193]. The $Pd@CeO_2$ hollow core–shell nanocatalyst, while not magnetically separable, demonstrated aggregation- and leaching-resistant properties that enabled recovery through simple centrifugation without catalyst deactivation [202].

6.5. Surface Functionalization for Toxicity Mitigation

Silica coating represents the most extensively studied and effective strategy for toxicity reduction across diverse metal and metal oxide NPs. Hermetic encapsulation of nano-Ag with a ~2 nm thin SiO_2 layer completely blocked toxicity against *E. coli* growth, with 7.8 wt% and 9.5 wt% SiO_2-coated nano-Ag showing bacterial growth nearly identical to controls (no particles) and pure SiO_2, while lower SiO_2 content (1.4 wt% and 1.9 wt%) provided only partial protection [206]. The mechanism involves preventing direct cell contact and blocking Ag^+ ion release, as confirmed by dissolution studies showing 2.8 ± 1.4% Ag dissolution for SiO_2-coated Ag/Fe_2O_3 compared to 7 ± 1.7% for uncoated NPs [196].

Quantitative toxicity reduction through silica coating has been demonstrated across multiple cell lines and nanoparticle types. Surface passivation of Fe_3O_4/SiO_2 NPs with amino- or sulfonate-silanes significantly reduced toxicity, with bare NPs causing strong viability reduction at 2.5 and 5 nM concentrations, while passivated NPs showed no toxicity signs [207]. Bare NPs induced high membrane damage measured by LDH leakage, whereas passivated NPs caused only slight increases, with statistical significance at $p < 0.05$. Additionally, bare NPs led to significant ROS generation and greater mitochondrial membrane potential perturbation compared to passivated NPs, with surface passivation reducing iron ion release by 2-fold in acidic conditions [207].

Silica coating of ZnO NPs provides dramatic toxicity reduction through multiple mechanisms. Engineering safer-by-design silica-coated ZnO nanorods reduced DNA damage by over 3-fold compared to uncoated nanorods, with coated nanorods showing no DNA damage at concentrations up to 10 μg/mL, similar to pure medium controls [208]. At 20 μg/mL, DNA damage remained much lower than with uncoated nanorods, with statistical significance at $p < 0.01$ and $p < 0.001$. This protective effect is attributed to inhibiting ZnO dissolution and minimizing direct cellular contact [208]. Similarly, SiO_2-coated

ZnO NPs maintained cell viability above 75% across all incubation times, compared to uncoated ZnO, which reduced viability to 31% at 30 μg/mL [209].

Polymer-based surface modifications offer complementary toxicity mitigation strategies. Poly-L-lysine coating of Au-Fe_3O_4 NPs resulted in less than 10% cytotoxicity at concentrations up to 100 μg/mL in BT-474 and MDA-MB-231 cells, compared to 40% and 60% growth inhibition when internalized NPs were triggered by NIR laser [210]. PEGylation combined with silica coating provided synergistic benefits, with NPFe@FeO_x@SiO_2-PEG showing increased viability on 1BR3G cells and retaining 100% cell viability on CCD112-CoN cells at 24 h, compared to NPFe@FeO_x@SiO_2, which caused viability to decrease below 10% [211].

The thickness and completeness of protective coatings critically determine toxicity mitigation efficacy. Thicker SiO_2/ZnO NPs revealed reduced enzyme leakage, decreased peroxide production, and less oxidative stress compared to bare ZnO or thinner SiO_2/ZnO NPs, moderating toxicity by restricting free radical formation, Zn ion release, and decreasing surface contact with cells [187]. Silica shells of approximately 2 nm thickness around 5 nm Au cores (total particle size ~9 nm) exhibited much smaller cytotoxicity than polymer-coated NPs, showing negligible perturbation on gene expression patterns of lung and skin epithelial cells [212].

Multi-component coating strategies demonstrate enhanced protection. Polymer-based surface modifications of hollow porous iron oxide NPs using chitosan, PEG, and alginate enhanced biocompatibility, with polymer-coated NPs showing 2 to 3% hemolysis compared to 4 to 5% for uncoated, and cell viability exceeding 80% for both coated and uncoated at 100 μg/mL across 3 normal cell lines [213]. Cytotoxicity against cancer cells was 29% for polymer-coated vs. 38% for uncoated at 100 μg/mL, indicating selective toxicity enhancement toward cancer cells while protecting normal cells [213].

The protective mechanisms of surface functionalization extend beyond simple physical barriers. Native Fe_3O_4@MSN induced 40% cell death at 100 μg/mL, while PEG or DMPC coatings reduced this to 5% and 30%, respectively, in MTT assays, with none of these NPs showing toxicity in mice 4 days after intravenous injection of a 40 mg/kg dose [214]. The surface composition strongly influences dispersion and interaction with cell membranes, with PEG coatings reducing protein corona formation and subsequent cellular uptake, thereby decreasing cytotoxicity through reduced cellular exposure rather than altered intracellular dissolution [215].

TiO_2 shell coatings provide an alternative passivation strategy for ZnO NPs. The ZnO/TiO_2 core/shell structure moderated toxicity by curtailing Zn ion release and decreasing the contact area of ZnO cores with biological systems [216]. The selection of coating material depends on the specific application requirements, with silica offering superior biocompatibility for biomedical applications, while TiO_2 coatings may provide additional photocatalytic functionality alongside toxicity reduction [216].

7. Limitations and Future Directions

The exploration of mono-, bi-, tri-, and tetra-metal-metal oxide heterostructures for biological applications such as antimicrobial and anticancer therapies, as well as dye degradation, presents both promising opportunities and notable limitations. These heterostructures leverage the unique properties of metal oxides, such as high surface area, catalytic activity, and biocompatibility, to enhance their effectiveness in these applications. However, challenges such as toxicity, stability, and scalability remain significant barriers to their widespread adoption. Future research directions focus on overcoming these limitations through innovative synthesis methods and comprehensive understanding of their mechanisms.

- Standardization of synthesis protocols: Lack of standardized synthesis protocols and comparative studies evaluating the influence of synthesis parameters on nanoparticle properties and performance, especially for multi-component systems. Develop and validate standardized, reproducible synthesis protocols for mono-, bi-, tri-, and tetra-metal oxide heterostructures; conduct systematic comparative studies to correlate synthesis parameters with structural and functional outcomes. Standardization is essential to ensure reproducibility, scalability, and reliable benchmarking across studies, which is currently limited by diverse and non-uniform methods [123,178].
- Comprehensive interface characterization: Insufficient in-depth characterization of interfacial structures, defect states, and phase purity in complex heterostructures, limiting mechanistic understanding of charge transfer. Employ advanced spectroscopic, microscopic, and computational techniques (e.g., HR-TEM, XPS, DFT) to elucidate interface chemistry, defect types, and heterojunction architectures in multi-metal oxide systems. Detailed interface characterization is critical to unravel synergistic effects and optimize charge separation mechanisms, which remain underexplored in many studies [178,217].
- Mechanistic insights across complexity levels: Limited mechanistic studies comparing charge transfer and reactive species generation across mono-, bi-, tri-, and tetra-metal oxide heterostructures under standardized conditions. Conduct systematic mechanistic investigations using photoluminescence, radical trapping, and DFT calculations across heterostructure complexities to establish universal or distinct charge transfer pathways. Understanding how heterostructure complexity influences functional mechanisms is key to rational design but is currently fragmented and speculative [178,217,218].
- Comparative biological efficacy benchmarking: Scarcity of direct comparative evaluations of antimicrobial and anticancer efficacy across different heterostructure complexities with standardized biological assays. Design studies that systematically compare biological activities (MIC, IC_{50}) of mono-, bi-, tri-, and tetra-metal oxide NPs using uniform cell lines and microbial strains, including toxicity assessments on normal cells. Benchmarking biological efficacy is necessary to identify optimal compositions and ensure safety, which is currently hindered by inconsistent testing and limited toxicity data [90,219,220].
- Long-term stability and recyclability: Insufficient data on long-term operational stability, recyclability, and durability of heterostructured NPs under realistic environmental and biological conditions. Perform extended cyclic photocatalytic and biological activity tests under simulated real-world conditions; investigate structural and functional stability post-reuse. Stability and recyclability are critical for practical applications but are often only superficially addressed, limiting translation potential [221].
- Real-world environmental application testing: Predominant focus on model dyes and controlled lab conditions, with limited studies on complex real wastewater matrices and pollutant mixtures. Evaluate photocatalytic and antimicrobial performance in real wastewater samples containing mixed pollutants; assess degradation pathways and toxicity of by-products. Realistic testing is essential to validate environmental applicability and safety, which is currently underreported [183–185].
- Influence of green synthesis on functional performance: Underexplored impact of green synthesis parameters on nanoparticle morphology, stability, charge transfer efficiency, and biocompatibility, especially in multi-component systems. Investigate how different plant extracts and green synthesis conditions affect physicochemical properties, charge dynamics, and biological responses; standardize green synthesis protocols. Green synthesis offers sustainability and biocompatibility benefits but

shows variability affecting performance, necessitating systematic evaluation [90,222,223].

- Toxicity and biocompatibility assessments: Limited comprehensive in vivo toxicity and biocompatibility studies for multi-metal oxide heterostructured NPs, impeding clinical and environmental safety evaluations. Conduct detailed in vivo toxicity, biodistribution, and immunogenicity studies; develop standardized biocompatibility assays for green and chemically synthesized NPs. Safety profiles are crucial for biomedical applications but remain inadequately addressed, especially for complex heterostructures [219,220,223].
- Correlation of structural/morphological features with function: Incomplete quantitative correlation between particle size distribution, morphology heterogeneity, defect density, and functional performance across heterostructure types. Utilize advanced imaging and statistical analyses to correlate precise structural parameters with photocatalytic and biological activities; develop predictive models. Establishing structure-function relationships enables targeted design but is limited by inconsistent morphological characterization [217,222].
- Scalability and economic feasibility: Lack of studies addressing the scalability, cost-effectiveness, and industrial feasibility of synthesizing multi-metal oxide heterostructured NPs. Investigate scalable synthesis methods, cost analysis, and life-cycle assessments; optimize synthesis for industrial production without compromising performance. Practical deployment requires scalable and economical processes, which are rarely discussed in current research [123,178,183].

While the potential of metal-metal oxide heterostructures in antimicrobial, anticancer, and dye degradation applications is significant, the path to clinical and industrial adoption is fraught with challenges. Addressing these challenges through innovative synthesis, comprehensive toxicity studies, and regulatory navigation will be crucial. Additionally, exploring the integration of these NPs with existing technologies and therapies could further enhance their applicability and effectiveness.

8. Conclusive Remarks

The analysis of metal-metal oxide heterostructures has fundamentally shifted the paradigm of nanomaterial design from single-component simplicity towards interface-driven complexity. This review critically examines the trajectory from mono- to tetra-metallic systems, evaluating whether the increasing synthesis investment yields proportional gains in antimicrobial, anticancer, and photocatalytic performance. The evidence clearly establishes that the heterointerface is the true site of functional synergy. Bimetallic systems, through the creation of Schottky barriers and plasmonic effects, consistently transcend the inherent limitations of monometallic oxides (namely, wide band gaps and rapid charge recombination), delivering dramatic enhancements in ROS generation and dye degradation kinetics. They represent a transformative step forward, achieving a compelling balance between enhanced functionality and synthetic tractability.

However, the progression to tri- and tetra-metallic heterostructures reveals a more complex landscape. While these higher-order systems offer the prospect of all-in-one theranostic platforms and cascade charge-transfer 'highways', the current literature provides insufficient evidence to claim that their performance gains are universally proportional to their added complexity. A critical gap persists: the absence of systematic, standardized comparative studies that rigorously benchmark multi-component systems against their simpler counterparts under identical conditions. Too often, the narrative of 'the more, the better' is assumed rather than proven, obscuring the point at which diminishing returns or insignificant synthesis challenges emerge.

The future of this field, therefore, centers on a deliberate shift from empirical exploration to rational, evidence-based design. We theorize that the most impactful next-generation materials will not necessarily be the most complex, but rather those with optimally engineered interfaces tailored for a specific function. For many applications, a well-designed bimetallic heterojunction may represent the rational peak of the cost–benefit curve. The pursuit of tri- and tetra-metallic heterostructures should be reserved for applications demanding unique, clinically or environmentally relevant functionalities (such as multimodal imaging or synergistic therapy combinations) that are demonstrably unattainable with simpler designs. By embracing rigorous comparative analysis and focusing on the quality of the interface over the quantity of components, the field can successfully translate the immense promise of synergistic heterostructures into real-world technologies that safeguard human health and remediate our environment.

Author Contributions: Conceptualization, R.G., A.H.S., M.A., M.C. and A.V.; writing—original draft preparation, R.G., A.H.S., M.A., M.C., A.V., S.D. and U.T.K.; writing—review and editing, R.G., A.H.S., M.A., M.C., A.V., S.D. and U.T.K.; supervision, A.V. All authors have read and agreed to the published version of the manuscript.

Funding: This research received no external funding.

Institutional Review Board Statement: Not applicable.

Informed Consent Statement: Not applicable.

Data Availability Statement: No new data were created or analyzed in this study. Data sharing is not applicable to this article.

Acknowledgments: During the preparation of this work, the authors used Grammarly Pro in order to improve the readability and sentence structure. After using this tool/service, the authors reviewed and edited the content as needed and take full responsibility for the content of the publication.

Conflicts of Interest: Author Manohar Aele was employed by the company ModernaTX, and Author Muralikrishna Cherukuru was employed by the company Ingenus Pharmaceuticals. All the authors declare that the research was conducted in the absence of any commercial or financial relationships that could be construed as a potential conflict of interest.

Abbreviations

The following abbreviations are used in this manuscript:

NPs	Nanoparticles
e^-	Electron
h^+	Hole
LSPR	Localized surface plasmon resonance
MIC	Minimum inhibitory concentration
MBC	Minimum bactericidal concentration
ROS	Reactive oxygen species
HR-TEM	High-resolution transmission electron microscopy
XRD	X-ray diffraction
XPS	X-ray photoelectron spectroscopy
ICP-AES	Inductively coupled plasma atomic emission spectroscopy
UV	Ultraviolet
BET	Brunauer–Emmett–Teller
CO	Carbon monoxide
rGO	Reduced graphene oxide
RT	Room temperature
EDX	Energy-dispersive X-ray spectroscopy
SAED	Selected area electron diffraction

STEM	Scanning transmission electron microscopy
FE-SEM	Field-emission scanning electron microscopy
EIS	Electrochemical impedance spectroscopy
FTIR	Fourier-transform infrared spectroscopy
XAS	X-ray absorption spectroscopy
XANES	X-ray absorption near-edge structure
EXAFS	Extended X-ray absorption fine structure
JCPDS	Joint Committee on Powder Diffraction Standards
NIR	Near-infrared
•OH	Hydroxyl
$\bullet O_2^-$	Superoxide anions
SPR	Surface plasmon resonance
MRSA	Methicillin-resistant *Staphylococcus aureus*
H_2O_2	Hydrogen peroxide
QDs	Quantum dots
PTT	Photothermal therapy
PDT	Photodynamic therapy
MRI	Magnetic resonance imaging
MOFs	Metal–organic frameworks
RaST	Radionuclide-stimulated dynamic therapy
TRPL	Time-resolved photoluminescence
Rct	Charge transfer resistance

References

1. Bongomin, F.; Gago, S.; Oladele, R.; Denning, D. Global and Multi-National Prevalence of Fungal Diseases—Estimate Precision. *J. Fungi* **2017**, *3*, 57. https://doi.org/10.3390/jof3040057.
2. Sharaf, M.; Mohammed, E.J.; Farahat, E.M.; Alrehaili, A.A.; Alkhudhayri, A.; Ali, A.M.; Zahra, A.A.; Zakai, S.A.; Elkelish, A.; AlHarbi, M.; et al. Biocide Syntheses Bee Venom-Conjugated ZnO@αFe2O3 Nanoflowers as an Advanced Platform Targeting Multidrug-Resistant Fecal Coliform Bacteria Biofilm Isolated from Treated Wastewater. *Microbiol. Res.* **2023**, *14*, 1489–1510. https://doi.org/10.3390/microbiolres14040102.
3. Wang, L.; Yang, F.; Gong, J.; Chen, W.; Zheng, Y.; Chen, X.; Hu, W.; Li, Y.; Yang, K.; Wang, Z.; et al. Acid-Responsive Bimetallic Peroxide Composite Nanoplatform for Synergistic Therapy of Drug-Resistant Bacterial Infections via Inducing Oxidative Stress and Disrupting Bacterial Energy Metabolism. *ACS Appl. Mater. Interfaces* **2025**, *17*, 60361–60375. https://doi.org/10.1021/acsami.5c17878.
4. Lone, A.L.; Rehman, S.U.; Haq, S.; Shahzad, N.; Al-Sadoon, M.K.; Shahzad, M.I.; Razzokov, J.; Shujaat, S.; Samad, A. Unveiling the Physicochemical, Photocatalytic, Antibacterial and Antioxidant Properties of MWCNT-Modified Ag2O/CuO/ZnO Nanocomposites. *RSC Adv.* **2025**, *15*, 1323–1334. https://doi.org/10.1039/D4RA08466G.
5. Periyasamy, A.P. Recent Advances in the Remediation of Textile-Dye-Containing Wastewater: Prioritizing Human Health and Sustainable Wastewater Treatment. *Sustainability* **2024**, *16*, 495. https://doi.org/10.3390/su16020495.
6. Geetha, R. Environmental Impact of Ineffective Antibiotic Disposal: Strategies and Remedial Pathways: A Comprehensive Review. *Environ. Qual. Manag.* **2025**, *34*, e70034. https://doi.org/10.1002/tqem.70034.
7. Tanwar, R.; Mandal, U.K. Photocatalytic Activity of Ni0.5Zn0.5Fe2O4@polyaniline Decorated BiOCl for Azo Dye Degradation Under Visible Light—Integrated Role and Degradation Kinetics Interpretation. *RSC Adv.* **2019**, *9*, 8977–8993. https://doi.org/10.1039/C9RA00548J.
8. Shaikh, B.; Bhatti, M.A.; Shah, A.A.; Tahira, A.; Shah, A.K.; Usto, A.; Aftab, U.; Bukhari, S.I.; Alshehri, S.; Shah Bukhari, S.N.U.; et al. Mn3O4@ZnO Hybrid Material: An Excellent Photocatalyst for the Degradation of Synthetic Dyes Including Methylene Blue, Methyl Orange and Malachite Green. *Nanomaterials* **2022**, *12*, 3754. https://doi.org/10.3390/nano12213754.
9. Botsa, S.M.; Basavaiah, K. Fabrication of Multifunctional TANI/Cu2O/Ag Nanocomposite for Environmental Abatement. *Sci. Rep.* **2020**, *10*, 14080. https://doi.org/10.1038/s41598-020-70194-9.
10. Chudasama, B.; Vala, A.K.; Andhariya, N.; Upadhyay, R.V.; Mehta, R.V. Enhanced Antibacterial Activity of Bifunctional Fe3O4-Ag Core-Shell Nanostructures. *Nano Res.* **2009**, *2*, 955–965. https://doi.org/10.1007/s12274-009-9098-4.
11. Khan, A.; Zaid, M.; Ameen, F.; Khan, M.A.; Kumar, S.; Al-Masri, A.A.; Islam, M.A. Colossal Antibacterial, Antibiofilm and Solar Light-Driven Photocatalytic Activity of Nanoenhanced Conjugate of Bimetallic Ag-Zr Nanoparticles with Graphene Oxide. *J. Mol. Struct.* **2024**, *1300*, 137223. https://doi.org/10.1016/j.molstruc.2023.137223.

12. Mosleh, A.T.; Kamoun, E.A.; EL-Moslamy, S.H.; Salim, S.A.; Zahran, H.Y.; Zyoud, S.H.; Yahia, I.S. Performance of Ag-Doped CuO Nanoparticles for Photocatalytic Activity Applications: Synthesis, Characterization, and Antimicrobial Activity. *Discov. Nano* **2024**, *19*, 166. https://doi.org/10.1186/s11671-024-04108-3.
13. Almutairi, H.H.; Parveen, N.; Ansari, S.A. Hydrothermal Synthesis of Multifunctional Bimetallic Ag-CuO Nanohybrids and Their Antimicrobial, Antibiofilm and Antiproliferative Potential. *Nanomaterials* **2022**, *12*, 4167. https://doi.org/10.3390/nano12234167.
14. Krishnan, M.; Subramanian, H.; Ramachandran, S.K.; Muthukumarasamy, A.; Ramadoss, D.; Mahalingam, A.; Rathinam, A.J.; Dahms, H.-U.; Hwang, J.-S. Synthesis of Bimetallic BiPO4/ZnO Nanocomposite: Enhanced Photocatalytic Dye Degradation and Antibacterial Applications. *Int. J. Mol. Sci.* **2023**, *24*, 1947. https://doi.org/10.3390/ijms24031947.
15. Kgatle, M.; Sikhwivhilu, K.; Ndlovu, G.; Moloto, N. Degradation Kinetics of Methyl Orange Dye in Water Using Trimetallic Fe/Cu/Ag Nanoparticles. *Catalysts* **2021**, *11*, 428. https://doi.org/10.3390/catal11040428.
16. Arif, A.; Zaman, Y.; Ishaque, M.Z.; Siddique, A.B.; Zaman, H.; Shahzad, M.; Ali, D. Temperature-Dependent Heterojunction Ternary Nanocomposite: Assessing Photocatalytic and Antibacterial Applications. *Heliyon* **2024**, *10*, e27550. https://doi.org/10.1016/j.heliyon.2024.e27550.
17. Mukherjee, A.; Dhak, P.; Hazra, V.; Goswami, N.; Dhak, D. Synthesis of Mesoporous Fe/Al/La Trimetallic Oxide for Photodegradation of Various Water-Soluble Dyes: Kinetic, Mechanistic, and PH Studies. *Environ. Res.* **2023**, *217*, 114862. https://doi.org/10.1016/j.envres.2022.114862.
18. Nobile, C.; Cozzoli, P.D. Synthetic Approaches to Colloidal Nanocrystal Heterostructures Based on Metal and Metal-Oxide Materials. *Nanomaterials* **2022**, *12*, 1729. https://doi.org/10.3390/nano12101729.
19. Stefan, M.; Pana, O.; Leostean, C.; Bele, C.; Silipas, D.; Senila, M.; Gautron, E. Synthesis and Characterization of Fe3O4–TiO2 Core-Shell Nanoparticles. *J. Appl. Phys.* **2014**, *116*, 114312. https://doi.org/10.1063/1.4896070.
20. Liu, Y.; Ji, Y.; Li, Q.; Zhu, Y.; Peng, J.; Jia, R.; Lai, Z.; Shi, L.; Fan, F.; Zheng, G.; et al. A Surfactant-Free and General Strategy for the Synthesis of Bimetallic Core–Shell Nanocrystals on Reduced Graphene Oxide through Targeted Photodeposition. *ACS Nano* **2023**, *17*, 15085–15096. https://doi.org/10.1021/acsnano.3c04281.
21. Crane, C.C.; Tao, J.; Wang, F.; Zhu, Y.; Chen, J. Mask-Assisted Seeded Growth of Segmented Metallic Heteronanostructures. *J. Phys. Chem. C* **2014**, *118*, 28134–28142. https://doi.org/10.1021/jp5094433.
22. Aslan, N. Synthesis and Characterization of ZnO@Fe3O4 Composite Nanostructures by Using Hydrothermal Synthesis Method. *Türk Doğa ve Fen Derg.* **2022**, *11*, 95–101. https://doi.org/10.46810/tdfd.1011220.
23. Bian, N.; Mayanovic, R.A.; Benamara, M. Synthesis and Characterization of Co3O4-MnxCo3-XO4 Core-Shell Nanoparticles. *MRS Adv.* **2018**, *3*, 2899–2904. https://doi.org/10.1557/adv.2018.453.
24. Keleşoğlu, G.S.; Özdinçer, M.; Dalmaz, A.; Zenkin, K.; Durmuş, S. Green Synthesis and Structural Characterization of ZnO Nanoparticle and ZnO@TiO2 Nanocomposite by Cinnamomum Verum Bark Extract. *Turk. J. Anal. Chem.* **2023**, *5*, 118–123. https://doi.org/10.51435/turkjac.1395817.
25. Zanganeh, N.; Guda, V.K.; Toghiani, H.; Keith, J.M. Sinter-Resistant and Highly Active Sub-5 Nm Bimetallic Au–Cu Nanoparticle Catalysts Encapsulated in Silica for High-Temperature Carbon Monoxide Oxidation. *ACS Appl. Mater. Interfaces* **2018**, *10*, 4776–4785. https://doi.org/10.1021/acsami.7b19299.
26. Bhuskute, B.D.; Tinus, T.; Ali-Löytty, H.; Saari, J.; Lahtonen, K.; Valden, M. Low-Density Ag–Au Nanoparticle Photodeposition on TiO_2 Thin Film Photocatalysts Grown by Atomic Layer Deposition. *Phys. Chem. Chem. Phys.* **2025**, *27*, 16865–16874. https://doi.org/10.1039/D5CP00834D.
27. Kumar-Krishnan, S.; Estevez-González, M.; Pérez, R.; Esparza, R.; Meyyappan, M. A General Seed-Mediated Approach to the Synthesis of AgM (M = Au, Pt, and Pd) Core–Shell Nanoplates and Their SERS Properties. *RSC Adv.* **2017**, *7*, 27170–27176. https://doi.org/10.1039/C7RA04301E.
28. Bukka, S.; Umehara, Y.; Higashimine, K.; Badam, R.; Vedarajan, R.; Matsumi, N. Ultrafast Electrochemical Deposition of Core Shell Metal Nanoparticles on TiO_2 Nanotubes for Electrocatalytic Applications. *Mater. Res. Express* **2018**, *5*, 115016. https://doi.org/10.1088/2053-1591/aadc82.
29. Goswami, M.; Pal, D.; Ghosh, M.K.; Dwivedi, S.; Chandraker, S.K. Bimetallic Nanoparticles: A Comprehensive Review of Synthesis Methods and Their Potential Application. *ChemistrySelect* **2025**, *10*, e01493. https://doi.org/10.1002/slct.202501493.
30. Idris, D.S.; Roy, A. Synthesis of Bimetallic Nanoparticles and Applications—An Updated Review. *Crystals* **2023**, *13*, 637. https://doi.org/10.3390/cryst13040637.
31. Buck, M.R.; Bondi, J.F.; Schaak, R.E. A Total-Synthesis Framework for the Construction of High-Order Colloidal Hybrid Nanoparticles. *Nat. Chem.* **2012**, *4*, 37–44. https://doi.org/10.1038/nchem.1195.

32. Wang, R.; Yang, W.; Song, Y.; Shen, X.; Wang, J.; Zhong, X.; Li, S.; Song, Y. A General Strategy for Nanohybrids Synthesis via Coupled Competitive Reactions Controlled in a Hybrid Process. *Sci. Rep.* **2015**, *5*, 9189. https://doi.org/10.1038/srep09189.
33. Foucher, A.C.; Yang, S.; Rosen, D.J.; Lee, J.D.; Huang, R.; Jiang, Z.; Barrera, F.G.; Chen, K.; Hollyer, G.G.; Friend, C.M.; et al. Synthesis and Characterization of Core-Shell Cu-Ru, Cu-Rh, and Cu-Ir Nanoparticles. *J. Am. Chem. Soc.* **2022**, *144*, 7919–7928. https://doi.org/10.1021/jacs.2c02538.
34. Song, S.; Wang, X.; Zhang, H. CeO2-Encapsulated Noble Metal Nanocatalysts: Enhanced Activity and Stability for Catalytic Application. *NPG Asia Mater.* **2015**, *7*, e179. https://doi.org/10.1038/am.2015.27.
35. Panferov, V.G.; Byzova, N.A.; Shumaev, K.B.; Zherdev, A.V.; Dzantiev, B.B. Tetrametallic Au@Ag-Pd-Pt Nanozyme with Surface-Exposed Active Sites for Enhanced Catalytic Activity. *Nanomaterials* **2025**, *15*, 1833. https://doi.org/10.3390/nano15231833.
36. Bera, K.K.; Chowdhury, A.; Bera, S.K.; Das, M.R.; Roy, A.; Das, S.; Bhattacharya, S.K. Pd Nanoparticle-Decorated Novel Ternary $Bi_2O_2CO_3$-Bi_2MoO_6-CuO Heterojunction for Enhanced Photo-Electrocatalytic Ethanol Oxidation. *ACS Omega* **2023**, *8*, 28419–28435. https://doi.org/10.1021/acsomega.3c02669.
37. Sun, L.; Wen, K.; Li, G.; Zhang, X.; Zeng, X.; Johannessen, B.; Zhang, S. High-Entropy Alloys in Catalysis: Progress, Challenges, and Prospects. *ACS Mater. Au* **2024**, *4*, 547–556. https://doi.org/10.1021/acsmaterialsau.4c00080.
38. Hashimoto, N.; Mori, K.; Yoshida, H.; Kamiuchi, N.; Kitaura, R.; Hirasawa, R.; Yamashita, H. Thermal Stability of High-Entropy Alloy Nanoparticles Evaluated by In Situ TEM Observations. *Nano Lett.* **2024**, *24*, 7063–7068. https://doi.org/10.1021/acs.nanolett.4c01625.
39. Bolar, S.; Ito, Y.; Fujita, T. Future Prospects of High-Entropy Alloys as next-Generation Industrial Electrode Materials. *Chem. Sci.* **2024**, *15*, 8664–8722. https://doi.org/10.1039/D3SC06784J.
40. Garcia-Torres, J.; Vallés, E.; Gómez, E. Synthesis and Characterization of Co@Ag Core–Shell Nanoparticles. *J. Nanoparticle Res.* **2010**, *12*, 2189–2199. https://doi.org/10.1007/s11051-009-9784-x.
41. Ariga, K.; Vinu, A.; Yamauchi, Y.; Ji, Q.; Hill, J.P. Nanoarchitectonics for Mesoporous Materials. *Bull. Chem. Soc. Jpn.* **2012**, *85*, 1–32. https://doi.org/10.1246/bcsj.20110162.
42. Tancredi, P.; Moscoso Londoño, O.; Rivas Rojas, P.C.; Wolff, U.; Socolovsky, L.M.; Knobel, M.; Muraca, D. Strategies to Tailor the Architecture of Dual Ag/Fe-Oxide Nano-Heterocrystals—Interfacial and Morphology Effects on the Magnetic Behavior. *J. Phys. D Appl. Phys.* **2018**, *51*, 295303. https://doi.org/10.1088/1361-6463/aaccc3.
43. Chen, G.; Du, J.; Gu, L.; Wang, Q.; Qi, Q.; Li, X.; Zhang, R.; Yang, H.; Miao, Y.; Li, Y. Metal-Sensitized Au-Bi2O3 Nanoheterojunction for Immunogenic Cell Death-Boosted Sono-Immuno Cancer Therapy. *Chem. Eng. J.* **2024**, *482*, 148953. https://doi.org/10.1016/j.cej.2024.148953.
44. Elsayed, K.A.; Alomari, M.; Drmosh, Q.A.; Manda, A.A.; Haladu, S.A.; Olanrewaju Alade, I. Anticancer Activity of TiO2/Au Nanocomposite Prepared by Laser Ablation Technique on Breast and Cervical Cancers. *Opt. Laser Technol.* **2022**, *149*, 107828. https://doi.org/10.1016/j.optlastec.2021.107828.
45. Ramamoorthy, S.; Reji, R.P.; Jayaraman, S.V.; Sundaramurthy, A. Fabrication of BiCuOS Nanoflowers Acting as Nanoarrays on Photonic Nanoparticles for Chemo-Photothermal Therapy. *Appl. Surf. Sci.* **2023**, *640*, 158360. https://doi.org/10.1016/j.apsusc.2023.158360.
46. Elsayed, K.A.; Alomari, M.; Drmosh, Q.A.; Alheshibri, M.; Al Baroot, A.; Kayed, T.S.; Manda, A.A.; Al-Alotaibi, A.L. Fabrication of ZnO-Ag Bimetallic Nanoparticles by Laser Ablation for Anticancer Activity. *Alexandria Eng. J.* **2022**, *61*, 1449–1457. https://doi.org/10.1016/j.aej.2021.06.051.
47. Alinaghi, M.; Mokarram, P.; Ahmadi, M.; Bozorg-ghalati, F. Biosynthesis of Palladium, Platinum, and Their Bimetallic Nanoparticles Using Rosemary and Ginseng Herbal Plants: Evaluation of Anticancer Activity. *Sci. Rep.* **2024**, *14*, 5798. https://doi.org/10.1038/s41598-024-56275-z.
48. Lu, Y.; Wu, Y.; Tang, Z.; Hou, Y.; Cui, M.; Huang, S.; Long, B.; Yu, Z.; Iqbal, M.Z.; Kong, X. Synthesis of Multifunctional Mn3O4-Ag2S Janus Nanoparticles for Enhanced T1-Magnetic Resonance Imaging and Photo-Induced Tumor Therapy. *Sensors* **2023**, *23*, 8930. https://doi.org/10.3390/s23218930.
49. Basit, A.; Munir, R.M.; Liaqat, M.; Iqbal, T.; Afsheen, S.; Azam, A.; Maryam, I.; Khan, R.R.M.; Sayed, M.A.; Ali, A.M. Bi2O3/MoO3 Composites: A Synergistic Approach towards Photocatalytic Degradation and Enhanced Antimicrobial Activity. *Electrochim. Acta* **2024**, *497*, 144583. https://doi.org/10.1016/j.electacta.2024.144583.
50. Yu, Z.; Zhou, Y.; Zhang, H.; Zhang, M.; Zhang, R.; Yin, H.; Wang, J. One-Pot Hydrothermal Preparation of Rich-Oxygen Vacant Bi2SiO5/CuBi2O4 Z-Scheme Heterojunction for Visible Light-Driven Photocatalytic Removal of Antibiotic-Resistant Bacteria. *Chem. Eng. J.* **2023**, *478*, 147353. https://doi.org/10.1016/j.cej.2023.147353.

51. Ahmed, M.A.; Ahmed, M.A.; Mohamed, A.A. Fabrication of NiO/g-C3N4 Z-Scheme Heterojunction for Enhanced Photocatalytic Degradation of Methylene Blue Dye. *Opt. Mater.* **2024**, *151*, 115339. https://doi.org/10.1016/j.optmat.2024.115339.
52. Balu, K.; Abisheik, T.; Durai, M.; Pushpalatha, S.; Rajendran, A.; Kumaravel, S.; Kaliyamoorthy, S.; Al-Asbahi, B.A.; Pandiyan, V.; Ahn, Y.-H. Highly Efficient Ag Adorned HMTA Assisted ZnO Nanocomposite for Rapid Removal of Emerging Pollutants Based on Dangerous Dyes. *Opt. Mater.* **2024**, *151*, 115392. https://doi.org/10.1016/j.optmat.2024.115392.
53. Singh, P.; Devi, P. Deciphering the Photoelectrochemical Behaviour of MoSe2-Decorated BiVO4 as a Dual System for Concurrent Degradation of Methylene Blue and Hydrogen Generation. *J. Clean. Prod.* **2024**, *448*, 141502. https://doi.org/10.1016/j.jclepro.2024.141502.
54. Saeed, M.; Albalawi, K.; Khan, I.; Akram, N.; Abd El-Rahim, I.H.A.; Alhag, S.K.; Ezzat Ahmed, A. Faiza Synthesis of P-n NiO-ZnO Heterojunction for Photodegradation of Crystal Violet Dye. *Alex. Eng. J.* **2023**, *65*, 561–574. https://doi.org/10.1016/j.aej.2022.09.048.
55. Muhambihai, P.; Rama, V.; Subramaniam, P. Photocatalytic Degradation of Aniline Blue, Brilliant Green and Direct Red 80 Using NiO/CuO, CuO/ZnO and ZnO/NiO Nanocomposites. *Environ. Nanotechnol. Monit. Manag.* **2020**, *14*, 100360. https://doi.org/10.1016/j.enmm.2020.100360.
56. Shathy, R.A.; Fahim, S.A.; Sarker, M.; Quddus, M.S.; Moniruzzaman, M.; Masum, S.M.; Molla, M.A.I. Natural Sunlight Driven Photocatalytic Removal of Toxic Textile Dyes in Water Using B-Doped ZnO/TiO2 Nanocomposites. *Catalysts* **2022**, *12*, 308. https://doi.org/10.3390/catal12030308.
57. Shahzad, R.; Muneer, M.; Khalid, R.; Amin, H.M.A. ZnO-Bi2O3 Heterostructured Composite for the Photocatalytic Degradation of Orange 16 Reactive Dye: Synergistic Effect of UV Irradiation and Hydrogen Peroxide. *Catalysts* **2023**, *13*, 1328. https://doi.org/10.3390/catal13101328.
58. Khurram, R.; Wang, Z.; Ehsan, M.F.; Peng, S.; Shafiq, M.; Khan, B. Synthesis and Characterization of an α-Fe_2O_3/ZnTe Heterostructure for Photocatalytic Degradation of Congo Red, Methyl Orange and Methylene Blue. *RSC Adv.* **2020**, *10*, 44997–45007. https://doi.org/10.1039/D0RA06866G.
59. Bano, K.; Mittal, S.K.; Singh, P.P.; Kaushal, S. Sunlight Driven Photocatalytic Degradation of Organic Pollutants Using a MnV2O6/BiVO4 Heterojunction: Mechanistic Perception and Degradation Pathways. *Nanoscale Adv.* **2021**, *3*, 6446–6458. https://doi.org/10.1039/D1NA00499A.
60. Abduh, N.A.Y.; Al-Odayni, A.-B. Green Synthesis of ZnO/SnO2 Hybrid Nanocomposite for Degradation of Cationic and Anionic Dyes Under Sunlight Radiation. *Materials* **2023**, *16*, 7398. https://doi.org/10.3390/ma16237398.
61. Hasan, I.; Albaeejan, M.A.; Alshayiqi, A.A.; Al-Nafaei, W.S.; Alharthi, F.A. In Situ Hydrothermal Synthesis of Ni1−xMnxWO4 Nanoheterostructure for Enhanced Photodegradation of Methyl Orange. *Molecules* **2023**, *28*, 1140. https://doi.org/10.3390/molecules28031140.
62. Abdelrahman, E.A.; Al-Farraj, E.S. Facile Synthesis and Characterizations of Mixed Metal Oxide Nanoparticles for the Efficient Photocatalytic Degradation of Rhodamine B and Congo Red Dyes. *Nanomaterials* **2022**, *12*, 3992. https://doi.org/10.3390/nano12223992.
63. Oroumi, G.; Samimi, F.; Mahdi, M.A.; Dawi, E.A.; Salavati-Niasari, M. Insights into the Photocatalytic Role of Glycine-Assisted Sol-Gel Auto-Combustion Synthesized (Co, Mn)(Co, Mn)2O4 Nanostructures for Efficient Visible Light-Driven Degradation of Methyl Orange. *Arab. J. Chem.* **2024**, *17*, 105588. https://doi.org/10.1016/j.arabjc.2023.105588.
64. Ameen, F.; Aygun, A.; Seyrankaya, A.; Elhouda Tiri, R.N.; Gulbagca, F.; Kaynak, İ.; Majrashi, N.; Orfali, R.; Dragoi, E.N.; Sen, F. Photocatalytic Investigation of Textile Dyes and E. Coli Bacteria from Wastewater Using Fe3O4@MnO2 Heterojunction and Investigation for Hydrogen Generation on NaBH4 Hydrolysis. *Environ. Res.* **2023**, *220*, 115231. https://doi.org/10.1016/j.envres.2023.115231.
65. Alafaleq, N.O.; Zughaibi, T.A.; Jabir, N.R.; Khan, A.U.; Khan, M.S.; Tabrez, S. Biogenic Synthesis of Cu-Mn Bimetallic Nanoparticles Using Pumpkin Seeds Extract and Their Characterization and Anticancer Efficacy. *Nanomaterials* **2023**, *13*, 1201. https://doi.org/10.3390/nano13071201.
66. Baig, U.; Dastageer, M.A.; Gondal, M.A.; Khalil, A.B. Photocatalytic Deactivation of Sulphate Reducing Bacteria Using Visible Light Active CuO/TiO2 Nanocomposite Photocatalysts Synthesized by Ultrasonic Processing. *J. Photochem. Photobiol. B Biol.* **2023**, *242*, 112698. https://doi.org/10.1016/j.jphotobiol.2023.112698.
67. Almahdy, A.G.; El-Sayed, A.; Eltarahony, M. A Novel Functionalized CuTi Hybrid Nanocomposites: Facile One-Pot Mycosynthesis, Characterization, Antimicrobial, Antibiofilm, Antifouling and Wastewater Disinfection Performance. *Microb. Cell Fact.* **2024**, *23*, 148. https://doi.org/10.1186/s12934-024-02400-6.

68. Abdallah, E.M.; Modwi, A.; Al-Mijalli, S.H.; Mohammed, A.E.; Idriss, H.; Omar, A.S.; Afifi, M.; AL-Farga, A.; Goh, K.W.; Ming, L.C. In Vitro Influence of ZnO, CrZnO, RuZnO, and BaZnO Nanomaterials on Bacterial Growth. *Molecules* **2022**, *27*, 8309. https://doi.org/10.3390/molecules27238309.
69. Jayanetti, M.; Thambiliyagodage, C.; Liyanaarachchi, H.; Ekanayake, G.; Mendis, A.; Usgodaarachchi, L. In Vitro Influence of PEG Functionalized ZnO–CuO Nanocomposites on Bacterial Growth. *Sci. Rep.* **2024**, *14*, 1293. https://doi.org/10.1038/s41598-024-52014-6.
70. Xu, Q.; Li, D.; Zhou, H.; Chen, B.; Wang, J.; Wang, S.-B.; Chen, A.; Jiang, N. MnO_2-Coated Porous Pt@CeO_2 Core–Shell Nanostructures for Photoacoustic Imaging-Guided Tri-Modal Cancer Therapy. *Nanoscale* **2021**, *13*, 16499–16508. https://doi.org/10.1039/D1NR03246A.
71. Dash, P.; Nataraj, N.; Panda, P.K.; Tseng, C.-L.; Lin, Y.-C.; Sakthivel, R.; Chung, R.-J. Construction of Methotrexate-Loaded Bi_2S_3 Coated with Fe/Mn-Bimetallic Doped ZIF-8 Nanocomposites for Cancer Treatment Through the Synergistic Effects of Photothermal/Chemodynamic/Chemotherapy. *ACS Appl. Mater. Interfaces* **2025**, *17*, 222–234. https://doi.org/10.1021/acsami.4c13465.
72. Zhang, Y.; Liu, D.; Qiao, B.; Luo, Y.; Zhang, L.; Cao, Y.; Ran, H.; Yang, C. Breakthrough of Hypoxia Limitation by Tumor-Targeting Photothermal Therapy-Enhanced Radiation Therapy. *Int. J. Nanomed.* **2024**, *19*, 6499–6513. https://doi.org/10.2147/IJN.S450124.
73. Ahamed, M.; Lateef, R.; Khan, M.A.M.; Rajanahalli, P.; Akhtar, M.J. Biosynthesis, Characterization, and Augmented Anticancer Activity of ZrO2 Doped ZnO/RGO Nanocomposite. *J. Funct. Biomater.* **2023**, *14*, 38. https://doi.org/10.3390/jfb14010038.
74. Wang, Z.; Wang, G.; Kang, T.; Liu, S.; Wang, L.; Zou, H.; Chong, Y.; Liu, Y. BiVO4/Fe3O4@polydopamine Superparticles for Tumor Multimodal Imaging and Synergistic Therapy. *J. Nanobiotechnology* **2021**, *19*, 90. https://doi.org/10.1186/s12951-021-00802-x.
75. Huang, H.; Fang, L.; Wansapura, J.; Prior, J.L.; Manion, B.; Xu, B.; Hongsermeier, C.; Gamadia, N.; Blasi, N.; Tang, R.; et al. Cancer-Targeted pro-Theranostic Bi-Metallic Organo-Coordination Nanoparticles. *Theranostics* **2025**, *15*, 1205–1220. https://doi.org/10.7150/thno.99863.
76. 76. kumar, P.; Ramesh, M.R.; Doddamani, M.; Suresh, J.; Lingaraj, R. Green Synthesis of CuO/MgO/ZnO Nanoparticles Using Costus Pictus Leaf Extract for Effective Antibacterial Applications. *Mater. Lett.* **2024**, *359*, 135918. https://doi.org/10.1016/j.matlet.2024.135918.
77. Tong, J.; Zhai, H.; Zhao, S.; Song, L.; Wang, G.; Feng, N.; Tan, P.; Xie, J.; Pan, J. Visible Light-Driven Sliver-Modified Titanium Dioxide / Bismuth Molybdenum Oxide with Rapid Interfacial Charge-Transfer for Dual Highly Efficient Photocatalytic Degradation and Disinfection. *J. Colloid Interface Sci.* **2024**, *653*, 285–295. https://doi.org/10.1016/j.jcis.2023.09.069.
78. Parameswaran, S.; Shanmugam, P.; Bakkiyaraj, R.; T, V. Fabrication and Assessment of CuO and NiO-Infused MnO2 Nanocomposites: Characterization, Methylene Blue Degradation, and Antibacterial Efficacy. *J. Mol. Struct.* **2024**, *1303*, 137560. https://doi.org/10.1016/j.molstruc.2024.137560.
79. Khormali, K.; Mizwari, Z.M.; Masoumeh Ghoreishi, S.; Mortazavi-Derazkola, S.; Khezri, B. Novel Dy2O3/ZnO-Au Ternary Nanocomposites: Green Synthesis Using Pomegranate Fruit Extract, Characterization and Their Photocatalytic and Antibacterial Properties. *Bioorg. Chem.* **2021**, *115*, 105204. https://doi.org/10.1016/j.bioorg.2021.105204.
80. Ma, W.; Zhang, Y.; Chen, L.; Xie, X.; Yuan, S.; Qiu, Z.; Zhu, G.; Guo, J. A Novel ZnO-TiO2-Bi2WO6/Carboxymethyl Chitosan Composite with High Antimicrobial Activity and Visible-Light Catalytic Degradation of Ethylene towards Banana Preservation in Hot and Humid Environments. *Int. J. Biol. Macromol.* **2024**, *281*, 136559. https://doi.org/10.1016/j.ijbiomac.2024.136559.
81. Wang, Y.; Zhang, Z.; Chen, Y.; Zhu, Z.; Wang, H.; Tang, X. Enhanced LED Light-Driven Antibacterial System with Efficient Charge Transfer Coordinated by Bi2WO6/TiO2 Z-Scheme Heterojunction. *Ceram. Int.* **2024**, *50*, 9307–9322. https://doi.org/10.1016/j.ceramint.2023.12.247.
82. Rajendaran, K.; Muthuramalingam, R.; Ayyadurai, S. Green Synthesis of Ag-Mo/CuO Nanoparticles Using Azadirachta Indica Leaf Extracts to Study Its Solar Photocatalytic and Antimicrobial Activities. *Mater. Sci. Semicond. Process.* **2019**, *91*, 230–238. https://doi.org/10.1016/j.mssp.2018.11.021.
83. Jabessa Masho, T.; Thillai Arasu, P.; Feyisa Bogale, R.; Amare Zerrefa, E.; Ramamurthy, S. Green Synthesis, Characterization of Ag2O/CuO/ZnO Nano Composites Using Aqueous Extract of Croton Macrostachyus Leaf for Photo Degradation, Anti-Microbial and Antioxidant Activities. *Results Chem.* **2024**, *7*, 101369. https://doi.org/10.1016/j.rechem.2024.101369.
84. Kalita, J.; Das, A.; Bharali, L.; Chakraborty, D.; Dhar, S.S.; Pandey, P. Prompt Antibacterial Activity of Silver Nanoparticle Decorated on HAp Embedded NiFe2O4 Nanocomposite (NiFe2O4@HAp-Ag) against Pathogenic Strains and Investigation of Its Photocatalytic Activity towards Degradation of Antibiotics. *Mater. Today Sustain.* **2023**, *24*, 100552. https://doi.org/10.1016/j.mtsust.2023.100552.

85. Ye, L.; He, X.; Obeng, E.; Wang, D.; Zheng, D.; Shen, T.; Shen, J.; Hu, R.; Deng, H. The CuO and AgO Co-Modified ZnO Nanocomposites for Promoting Wound Healing in Staphylococcus Aureus Infection. *Mater. Today Bio* **2023**, *18*, 100552. https://doi.org/10.1016/j.mtbio.2023.100552.
86. Nayak, S.K.; Dash, P.; Bariki, R.; Pradhan, S.K.; Panda, S.; Nayak, B.; Mishra, B.G. Metal–Organic Framework-Derived Hierarchical Ag/Sr6Bi2O9-α-Bi2O3 Ternary Photocatalyst for Micropollutant Remediation and Bacterial Photoinactivation. *ACS Appl. Eng. Mater.* **2024**, *2*, 179–194. https://doi.org/10.1021/acsaenm.3c00710.
87. Ma, Z.; Li, J.; Wang, N.; Guo, W.; Zhang, K. Antibacterial Activity and the Mechanism of the Z-Scheme Bi2MoO6/Bi5O7I Heterojunction Under Visible Light. *Molecules* **2023**, *28*, 6786. https://doi.org/10.3390/molecules28196786.
88. Aziz, S.N.; Abdulwahab, A.M.; Aldeen, T.S.; Alqabili, D.M.A. Synthesis, Characterization, and Evaluation of Antibacterial and Antifungal Activities of CuO-ZnO-Co3O4 Nanocomposites. *Heliyon* **2024**, *10*, e37802. https://doi.org/10.1016/j.heliyon.2024.e37802.
89. Al-Gaashani, R.; Pasha, M.; Jabbar, K.A.; Shetty, A.R.; Baqiah, H.; Mansour, S.; Kochkodan, V.; Lawler, J. Antimicrobial Activity of ZnO-Ag-MWCNTs Nanocomposites Prepared by a Simple Impregnation–Calcination Method. *Sci. Rep.* **2023**, *13*, 21418. https://doi.org/10.1038/s41598-023-48831-w.
90. Orshiso, T.A.; Zereffa, E.A.; Murthy, H.C.A.; Demissie, T.B.; Ghotekar, S.; Pagar, K.; Pardeshi, O. One-Pot Biopreparation of Trimetallic ZnO–MgO–CuO Nanoparticles: Enhanced Cytotoxicity, Antibacterial Activities and Molecular Docking Studies. *Chem. Afr.* **2024**, *7*, 1963–1980. https://doi.org/10.1007/s42250-023-00830-0.
91. Menon, K.; Lopis, A.D.; Choudhari, K.S.; Kulkarni, B.; Maradur, S.; Kulkarni, S.D. Scavenger-Free Solar Photocatalytic Degradation of Textile Dyes and Antibiotics Using Magnetically Separable Bi-Junctional Photocatalyst. *Mater. Res. Bull.* **2025**, *181*, 113074. https://doi.org/10.1016/j.materresbull.2024.113074.
92. Rahman, T.U.; Roy, H.; Shoronika, A.Z.; Fariha, A.; Hasan, M.; Islam, M.S.; Marwani, H.M.; Islam, A.; Hasan, M.M.; Alsukaibi, A.K.D.; et al. Sustainable Toxic Dye Removal and Degradation from Wastewater Using Novel Chitosan-Modified TiO2 and ZnO Nanocomposites. *J. Mol. Liq.* **2023**, *388*, 122764. https://doi.org/10.1016/j.molliq.2023.122764.
93. Nagesh, T.; Ramesh, K.; Ashok, B.; Jyothi, L.; Vijaya Kumar, B.; Upender, G. Insights into Charge Transfer via Z-Scheme for Rhodamine B Degradation over Novel Co3O4/ZnFe2O4 Nanocomposites. *Opt. Mater.* **2023**, *143*, 114140. https://doi.org/10.1016/j.optmat.2023.114140.
94. Singh, S.; Verma, N.; Umar, A.; Kansal, S.K. ZnCdS Nanoparticles Decorated Three-Dimensional MoO3 Polygonal Structure: A Novel Photocatalyst for Enhanced Solar Light-Driven Degradation of Methyl Orange Dye. *J. Alloys Compd.* **2024**, *997*, 174714. https://doi.org/10.1016/j.jallcom.2024.174714.
95. Nuengmatcha, P.; Kuyyogsuy, A.; Porrawatkul, P.; Pimsen, R.; Chanthai, S.; Nuengmatcha, P. Efficient Degradation of Dye Pollutants in Wastewater via Photocatalysis Using a Magnetic Zinc Oxide/Graphene/Iron Oxide-Based Catalyst. *Water Sci. Eng.* **2023**, *16*, 243–251. https://doi.org/10.1016/j.wse.2023.01.004.
96. Gorouhi, N.; Haghighi, M.; Shabani, M.; Almasi Jaf, C. Double Z-Scheme Ag2CrO4/Bi2O3–KBi6O9Br Nanophotocatalysts Designed via Microwave-Assisted Combustion-Precipitation Method for Degrading Toxic Organic Dyes. *J. Clean. Prod.* **2024**, *450*, 141850. https://doi.org/10.1016/j.jclepro.2024.141850.
97. Saravanan, R.; Agarwal, S.; Gupta, V.K.; Khan, M.M.; Gracia, F.; Mosquera, E.; Narayanan, V.; Stephen, A. Line Defect Ce3+ Induced Ag/CeO2/ZnO Nanostructure for Visible-Light Photocatalytic Activity. *J. Photochem. Photobiol. A Chem.* **2018**, *353*, 499–506. https://doi.org/10.1016/j.jphotochem.2017.12.011.
98. Dursun, S.; Akyıldız, H.; Kalem, V. Production of CuCoO2 Nanoparticle/SnO2 Nanofiber Heterostructures for Visible Light Photocatalytic Applications. *J. Photochem. Photobiol. A Chem.* **2023**, *434*, 114233. https://doi.org/10.1016/j.jphotochem.2022.114233.
99. Verma, R.; Khan, A.B.; Kumar, A.; Amar, A.K.; Kumar, N.; Dabodiya, T.S.; Barman, B. Photo-Catalytic Applications of Green Synthesized AM-Ag/CuO/ZnO Nano-Composite and Its Synergistic Effects. *Inorg. Chem. Commun.* **2023**, *157*, 111385. https://doi.org/10.1016/j.inoche.2023.111385.
100. Bhattacharya, D.; Ghoshal, D.; Mondal, D.; Paul, B.K.; Bose, N.; Das, S.; Basu, M. Visible Light Driven Degradation of Brilliant Green Dye Using Titanium Based Ternary Metal Oxide Photocatalyst. *Results Phys.* **2019**, *12*, 1850–1858. https://doi.org/10.1016/j.rinp.2019.01.065.
101. Taddesse, A.M.; Alemu, M.; Kebede, T. Enhanced Photocatalytic Activity of P-n-n Heterojunctions Ternary Composite Cu2O/ZnO/Ag3PO4 Under Visible Light Irradiation. *J. Environ. Chem. Eng.* **2020**, *8*, 104356. https://doi.org/10.1016/j.jece.2020.104356.

102. Gholamian, S.; Hamzehloo, M.; Farrokhnia, A. Enhanced Visible-Light Photocatalysis of TiO2/Fe3O4/BiOI Nanocomposites as Magnetically Recoverable for the Degradation of Dye Pollutants. *J. Environ. Chem. Eng.* **2021**, *9*, 104937. https://doi.org/10.1016/j.jece.2020.104937.
103. Jebelli, F.; Hasheminejad, H.; Zarean Mousaabadi, K. Efficient Photocatalytic Decolorization of Textile Wastewater Using Fe-Mo LDH/ZnO Nanocomposite: A Sustainable Approach for Environmental Remediation. *J. Water Process Eng.* **2024**, *59*, 104981. https://doi.org/10.1016/j.jwpe.2024.104981.
104. Jasim, N.A.; Ebrahim, S.E.; Ammar, S.H. Visible Light-Boosted Photodegradation Activity of Ag–$AgVO_3$/$Zn_{0.5}Mn_{0.5}Fe_2O_4$ Supported Heterojunctions for Effective Degradation of Organic Contaminates. *Open Eng.* **2024**, *14*, 20220585. https://doi.org/10.1515/eng-2022-0585.
105. Qamar, M.A.; Shahid, S.; Javed, M.; Shariq, M.; Fadhali, M.M.; Madkhali, O.; Ali, S.K.; Syed, I.S.; Awaji, M.Y.; Shakir Khan, M.; et al. Accelerated Decoloration of Organic Dyes from Wastewater Using Ternary Metal/g-C3N4/ZnO Nanocomposites: An Investigation of Impact of g-C3N4 Concentration and Ni and Mn Doping. *Catalysts* **2022**, *12*, 1388. https://doi.org/10.3390/catal12111388.
106. Xu, H.; Fan, P.; Xu, L. CuO/ZnO/CQDs@PAN Nanocomposites with Ternary Heterostructures for Enhancing Photocatalytic Performance. *Catalysts* **2023**, *13*, 110. https://doi.org/10.3390/catal13010110.
107. Saira; Abd El-Fattah, W.; Shahid, M.; Ashraf, S.; Sandhu, Z.A.; Guesmi, A.; Ben Hamadi, N.; Farhan, M.; Raza, M.A. Solar-Activated Titanium-Based Cu4O3/ZrO2/TiO2 Ternary Nano-Heterojunction for Rapid Photocatalytic Degradation of the Textile Dye Everzol Yellow 3RS. *Catalysts* **2025**, *15*, 751. https://doi.org/10.3390/catal15080751.
108. Dharmana, G.; Gurugubelli, T.R.; Viswanadham, B.; Bathula, B.; Yoo, K. Novel In Situ Fabrication of Fe-Doped Zinc Oxide/Tin Sulfide Heterostructures for Visible-Light-Driven Photocatalytic Degradation of Methylene Blue. *J. Chem.* **2023**, *2023*, 1–13. https://doi.org/10.1155/2023/1407395.
109. Gupta, S.V.; Kulkarni, V.V.; Ahmaruzzaman, M. Bandgap Engineering Approach for Designing CuO/Mn3O4/CeO2 Heterojunction as a Novel Photocatalyst for AOP-Assisted Degradation of Malachite Green Dye. *Sci. Rep.* **2023**, *13*, 3009. https://doi.org/10.1038/s41598-023-30096-y.
110. Mohammed, W.; Matalkeh, M.; Al Soubaihi, R.M.; Elzatahry, A.; Saoud, K.M. Visible Light Photocatalytic Degradation of Methylene Blue Dye and Pharmaceutical Wastes over Ternary NiO/Ag/TiO_2 Heterojunction. *ACS Omega* **2023**, *8*, 40063–40077. https://doi.org/10.1021/acsomega.3c01766.
111. Alshammari, N.A.; Kosa, S.A.; Patel, R.; Malik, M.A. Heterojunction-Based Photocatalytic Degradation of Rose Bengal Dye via Gold-Decorated α-Fe2O3-CeO2 Nanocomposites Under Visible-Light Irradiation. *Water* **2024**, *16*, 1334. https://doi.org/10.3390/w16101334.
112. Baig, M.T.; Kayan, A. Sol Gel Obtained Ti/Co/Mn Oxides Doped with 5wt% CuO for the Photocatalytic Removal of Organic Azo Dyes from Wastewater. *Mater. Res. Bull.* **2024**, *180*, 113070. https://doi.org/10.1016/j.materresbull.2024.113070.
113. Masula, K.; Kore, R.; Bhongiri, Y.; Pola, S.; Basude, M. Ag-Li-ZnO Nanostructures for Efficient Photocatalytic Degradation of Organic Dyes and Textile Wastewater Under Visible Light Treatment. *J. Mol. Struct.* **2024**, *1305*, 137750. https://doi.org/10.1016/j.molstruc.2024.137750.
114. Vaseghi, Z.; Tavakoli, O.; Nematollahzadeh, A. Rapid Biosynthesis of Novel Cu/Cr/Ni Trimetallic Oxide Nanoparticles with Antimicrobial Activity. *J. Environ. Chem. Eng.* **2018**, *6*, 1898–1911. https://doi.org/10.1016/j.jece.2018.02.038.
115. Tao, W.; Tuo, Z.; Wu, F.; Mu, K.; Xu, C.; Shi, Y.; Sun, Z.; Wang, Y.; Li, Y.; Zhong, Z.; et al. Albumin-Assembled Copper-Bismuth Bimetallic Sulfide Bioactive Nanosphere as an Amplifier of Oxidative Stress for Enhanced Radio-Chemodynamic Combination Therapy. *Regen. Biomater.* **2022**, *9*, rbac045. https://doi.org/10.1093/rb/rbac045.
116. Padervand, M.; Ghasemi, S.; Hajiahmadi, S.; Wang, C. K4Nb6O17/Fe3N/α-Fe2O3/C3N4 as an Enhanced Visible Light-Driven Quaternary Photocatalyst for Acetamiprid Photodegradation, CO2 Reduction, and Cancer Cells Treatment. *Appl. Surf. Sci.* **2021**, *544*, 148939. https://doi.org/10.1016/j.apsusc.2021.148939.
117. Sultana, M.; Mohapatra, S.R.; Ahmaruzzaman, M. A Novel Porous and Highly Efficient Fe-Ce-Co Nanoparticles Anchored in Biochar Derived from Coconut Husk for Photo-Fenton Degradation of Binary Mixtures of Dyes. *Environ. Nanotechnol. Monit. Manag.* **2023**, *20*, 100901. https://doi.org/10.1016/j.enmm.2023.100901.
118. Guo, P.; Zhang, D.; Liu, X.; Liu, W.; Wang, R.; Zhang, Z.; Qiu, S. In Situ Self-Assembly of Mesoporous Zn-Cd-Mo-S Quaternary Metal Sulfides with Double Heterojunction Synergistic Charge Transfer for Boosting Photocatalytic Hydrogen Production. *J. Alloys Compd.* **2022**, *921*, 166066. https://doi.org/10.1016/j.jallcom.2022.166066.

119. Yu, C.; Zeng, D.; Chen, F.; Ji, H.; Zeng, J.; Li, D.; Yang, K. Construction of Efficient Solar-Light-Driven Quaternary Ag3VO4/Zn3(VO4)2/Zn2V2O7/ ZnO Heterostructures for Removing Organic Pollutants via Phase Transformation and in-Situ Precipitation Route. *Appl. Catal. A Gen.* **2019**, *578*, 70–82. https://doi.org/10.1016/j.apcata.2019.04.002.
120. Sabarinathan, A.; Chinnathambi, M.; Jayaprakash, R.; Robert, R.; Uthrakumar, R.; Kaviyarasu, K. An Effective Photocatalytic Degradation of Methylene Blue with ZnO/SnO2—CeO2/CuO Quaternary Nanocomposite Driven by Visible Light Irradiation. *Inorg. Chem. Commun.* **2023**, *156*, 111164. https://doi.org/10.1016/j.inoche.2023.111164.
121. Ghorbani, M.; Abdouss, M. Fabrication of Quaternary Ag/BiOBr@Bi2MoO6/ZnO/g-C3N4 Composite for Direct Red 23 Dye Removal from Water. *Chem. Eng. J. Adv.* **2026**, *26*, 101085. https://doi.org/10.1016/j.ceja.2026.101085.
122. Sabzehmeidani, M.M.; Karimi, H.; Ghaedi, M. Nanofibers Based Quaternary CeO2/Co3O4/Ag/Ag3PO4 S-Scheme Heterojunction Photocatalyst with Enhanced Degradation of Organic Dyes. *Mater. Res. Bull.* **2022**, *147*, 111629. https://doi.org/10.1016/j.materresbull.2021.111629.
123. Murugadoss, G.; Thiruppathi, K.; Venkatesh, N.; Hazra, S.; Mohankumar, A.; Thiruppathi, G.; Kumar, M.R.; Sundararaj, P.; Rajabathar, J.R.; Sakthivel, P. Construction of Novel Quaternary Nanocomposite and Its Synergistic Effect towards Superior Photocatalytic and Antibacterial Application. *J. Environ. Chem. Eng.* **2022**, *10*, 106961. https://doi.org/10.1016/j.jece.2021.106961.
124. Yuan, L.; Gu, Z.; Zhang, J.; Zhang, Z.; Wan, Q.; Yu, L.; Mu, Q.; Sun, T.; Gao, G. A Pentametallic High-Entropy Mixed-Dimensional Mesoporous Heterostructure for Azo-Dye Wastewater Degradation and Decolorization. *Sep. Purif. Technol.* **2024**, *350*, 127951. https://doi.org/10.1016/j.seppur.2024.127951.
125. Mahmoud, R.; Eldin, Z.E.; Khalifa, A.; Ahmed Anwar, A.A.; GadelHak, Y.; Othman, S.I.; Allam, A.A.; Essam, D.; Abo El-Ela, F.I.; Aleem Abdel Aziz, S.A.; et al. Antifungal and Antibacterial Investigation of Quinary Zr Al Fe Co Ni Layered Double Hydroxide and Its Al Fe Co Ni Quaternary and Fe Co Ni Tertiary Roots. *RSC Adv.* **2024**, *14*, 14815–14834. https://doi.org/10.1039/D4RA00508B.
126. Negrescu, A.M.; Killian, M.S.; Raghu, S.N.V.; Schmuki, P.; Mazare, A.; Cimpean, A. Metal Oxide Nanoparticles: Review of Synthesis, Characterization and Biological Effects. *J. Funct. Biomater.* **2022**, *13*, 274. https://doi.org/10.3390/jfb13040274.
127. Zhang, Y.; Gao, X.; Zhi, L.; Liu, X.; Jiang, W.; Sun, Y.; Yang, J. The Synergetic Antibacterial Activity of Ag Islands on ZnO (Ag/ZnO) Heterostructure Nanoparticles and Its Mode of Action. *J. Inorg. Biochem.* **2014**, *130*, 74–83. https://doi.org/10.1016/j.jinorgbio.2013.10.004.
128. Maximenko, A.; Depciuch, J.; Łopuszyńska, N.; Stec, M.; Światkowska-Warkocka, Ż.; Bayev, V.; Zieliński, P.M.; Baran, J.; Fedotova, J.; Węglarz, W.P.; et al. Fe_3O_4@SiO_2@Au Nanoparticles for MRI-Guided Chemo/NIR Photothermal Therapy of Cancer Cells. *RSC Adv.* **2020**, *10*, 26508–26520. https://doi.org/10.1039/D0RA03699D.
129. Chlumsky, O.; Purkrtova, S.; Michova, H.; Sykorova, H.; Slepicka, P.; Fajstavr, D.; Ulbrich, P.; Viktorova, J.; Demnerova, K. Antimicrobial Properties of Palladium and Platinum Nanoparticles: A New Tool for Combating Food-Borne Pathogens. *Int. J. Mol. Sci.* **2021**, *22*, 7892. https://doi.org/10.3390/ijms22157892.
130. Pandey, M.; Singh, M.; Wasnik, K.; Gupta, S.; Patra, S.; Gupta, P.S.; Pareek, D.; Chaitanya, N.S.N.; Maity, S.; Reddy, A.B.M.; et al. Targeted and Enhanced Antimicrobial Inhibition of Mesoporous ZnO–Ag_2O/Ag, ZnO–CuO, and ZnO–SnO_2 Composite Nanoparticles. *ACS Omega* **2021**, *6*, 31615–31631. https://doi.org/10.1021/acsomega.1c04139.
131. Jiménez, A.B.P.; Aguilar, C.A.H.; Ramos, J.M.V.; Thangarasu, P. Synergistic Antibacterial Activity of Nanohybrid Materials ZnO–Ag and ZnO–Au: Synthesis, Characterization, and Comparative Analysis of Undoped and Doped ZnO Nanoparticles. *Aust. J. Chem.* **2015**, *68*, 288–297. https://doi.org/10.1071/CH14123.
132. Lin, C.-Y.; Li, W.-P.; Huang, S.-P.; Yeh, C.-S.; Yang, C.-M. Hollow Mesoporous Silica Nanosphere-Supported FePt Nanoparticles for Potential Theranostic Applications. *J. Mater. Chem. B* **2017**, *5*, 7598–7607. https://doi.org/10.1039/C7TB01812F.
133. Ye, J.; Hou, F.; Chen, G.; Zhong, T.; Xue, J.; Yu, F.; Lai, Y.; Yang, Y.; Liu, D.; Tian, Y.; et al. Novel Copper-Containing Ferrite Nanoparticles Exert Lethality to MRSA by Disrupting MRSA Cell Membrane Permeability, Depleting Intracellular Iron Ions, and Upregulating ROS Levels. *Front. Microbiol.* **2023**, *14*, 1023036. https://doi.org/10.3389/fmicb.2023.1023036.
134. Gudkov, S.V.; Burmistrov, D.E.; Fomina, P.A.; Validov, S.Z.; Kozlov, V.A. Antibacterial Properties of Copper Oxide Nanoparticles (Review). *Int. J. Mol. Sci.* **2024**, *25*, 11563. https://doi.org/10.3390/ijms252111563.
135. Zarenezhad, E.; Abdulabbas, H.T.; Marzi, M.; Ghazy, E.; Ekrahi, M.; Pezeshki, B.; Ghasemian, A.; Moawad, A.A. Nickel Nanoparticles: Applications and Antimicrobial Role against Methicillin-Resistant Staphylococcus Aureus Infections. *Antibiotics* **2022**, *11*, 1208. https://doi.org/10.3390/antibiotics11091208.
136. Karami, A.; Toronjo-Urquiza, L.; Kidd, S.; Sumby, C.J.; Bi, J. UCNP@ZnO:Co/Ag Composites: A Dual-Action Platform for Antibacterial Photodynamic Therapy via Synergistic Silver Ion and Reactive Oxygen Species Release. *ACS Appl. Mater. Interfaces* **2025**, *17*, 46850–46860. https://doi.org/10.1021/acsami.5c12472.

137. Li, W.; Anantachaisophon, S.; Vachiraanun, T.; Promchaisri, W.; Sangsawang, P.; Tanalikhit, P.; Ittisanronnachai, S.; Atithep, T.; Sanguanchua, P.; Ratanasangsathien, A.; et al. Enhanced Antibacterial Activity at Ag–Cu Nanojunctions: Unveiling the Mechanism with Simple Surfaces of CuNPs-on-Ag Films. *ACS Omega* **2023**, *8*, 34919–34927. https://doi.org/10.1021/acsomega.3c04303.
138. Govindasamy, G.A.; Mydin, R.B.S.M.N.; Sreekantan, S.; Harun, N.H. Compositions and Antimicrobial Properties of Binary ZnO–CuO Nanocomposites Encapsulated Calcium and Carbon from Calotropis Gigantea Targeted for Skin Pathogens. *Sci. Rep.* **2021**, *11*, 99. https://doi.org/10.1038/s41598-020-79547-w.
139. Soliman, M.K.Y.; Doghish, A.S.; Hashem, A.H.; Abdel-Maksoud, M.; El-Dakroury, W.A.; Alamri, A.; Ebaid, H.; Hasanin, M.S.; Saied, E. Novel Trimetallic (TiO_2–MgO–Au) Nanoparticles: Biosynthesis, Characterization, Antimicrobial, and Anticancer Activities. *Green Process. Synth.* **2025**, *14*, 20250007. https://doi.org/10.1515/gps-2025-0007.
140. Amin, M.A.; Algamdi, N.A.; Waznah, M.S.; Bukhari, D.A.; Alsharif, S.M.; Alkhayri, F.; Abdel-Nasser, M.; Fouda, A. An Insight into Antimicrobial, Antioxidant, Anticancer, and Antidiabetic Activities of Trimetallic Se/ZnO/CuO Nanoalloys Fabricated by Aqueous Extract of Nitraria Retusa. *J. Clust. Sci.* **2025**, *36*, 19. https://doi.org/10.1007/s10876-024-02742-6.
141. Guo, S.-B.; Chen, H.; Liu, Z.; Shi, J.; Li, C.; Qiao, Y.; Zhang, D.; Guo, T.; Ji, X.; Han, H.; et al. The Mechanisms of Lysis Triggered of Bacterial Cell Wall by Synergism of Ultrasmall Ag Quantum Dots and Zn Cu-Based Ferrites. 2023. Available online: https://ssrn.com/abstract=4653965.
142. Ratova, M.; Redfern, J.; Verran, J.; Kelly, P.J. Highly Efficient Photocatalytic Bismuth Oxide Coatings and Their Antimicrobial Properties Under Visible Light Irradiation. *Appl. Catal. B Environ.* **2018**, *239*, 223–232. https://doi.org/10.1016/j.apcatb.2018.08.020.
143. Alavi, M.; Kamarasu, P.; McClements, D.J.; Moore, M.D. Metal and Metal Oxide-Based Antiviral Nanoparticles: Properties, Mechanisms of Action, and Applications. *Adv. Colloid Interface Sci.* **2022**, *306*, 102726. https://doi.org/10.1016/j.cis.2022.102726.
144. Yapa, P.N.; Munaweera, I.; Sandaruwan, C.; Weerasinghe, L.; Weerasekera, M.M. Metal Doped Silica Nanohybrids with Extensive Bacterial Coverage for Antibacterial Applications Exhibit Synergistic Activity. *Biomater. Adv.* **2024**, *157*, 213753. https://doi.org/10.1016/j.bioadv.2023.213753.
145. Cho, E.-C.; Hsiao, Y.-S.; Huang, J.-H.; Sung, M.-Y.; Chen, Y.-L.; Wu, N.-J.; Hsu, S.-C.; Weng, H.C.; Lee, K.-C. Construction of BiVO4/Bi2WO6/WO3 Heterojunctions with Improved Photocatalytic Capability in Elimination of Dye and Antibiotics and Inactivation of E. Coli. *J. Taiwan Inst. Chem. Eng.* **2023**, *149*, 104991. https://doi.org/10.1016/j.jtice.2023.104991.
146. Kannaiyan, S.K.; Rengaraj, R.; Venkata Krishnan, G.R.; Gayathri, P.K.; Lavanya, G.; Hemapriya, D. Antimicrobial Activity of Green Synthesized Tri-Metallic Oxide Ni/Cr/Cu Nanoparticles. *J. Niger. Soc. Phys. Sci.* **2021**, *3*, 144–147. https://doi.org/10.46481/jnsps.2021.237.
147. Alnehia, A.; Al-Sharabi, A.; Alnahari, H.; Hadi, M. Synthesis and Characterization of MgO–CuO–Fe2O3 Nanocomposite: A Study of Its Structural, Optical, and Antibacterial Properties. *J. Chem.* **2024**, *2024*, 8129748. https://doi.org/10.1155/joch/8129748.
148. Ishaque, M.Z.; Zaman, Y.; Arif, A.; Siddique, A.B.; Shahzad, M.; Ali, D.; Aslam, M.; Zaman, H.; Faizan, M. Fabrication of Ternary Metal Oxide (ZnO:NiO:CuO) Nanocomposite Heterojunctions for Enhanced Photocatalytic and Antibacterial Applications. *RSC Adv.* **2023**, *13*, 30838–30854. https://doi.org/10.1039/D3RA05170F.
149. He, J.; Ma, Y.; Niu, X.; Pei, J.; Yan, R.; Xu, F.; Ma, J.; Ma, X.; Jia, S.; Ma, W. Silver Nanoparticles Induce Endothelial Cytotoxicity through ROS-Mediated Mitochondria-Lysosome Damage and Autophagy Perturbation: The Protective Role of N-Acetylcysteine. *Toxicology* **2024**, *502*, 153734. https://doi.org/10.1016/j.tox.2024.153734.
150. Wang, X.; Wang, W.-X. Cu(I)/Cu(II) Released by Cu Nanoparticles Revealed Differential Cellular Toxicity Related to Mitochondrial Dysfunction. *Environ. Sci. Technol.* **2023**, *57*, 9548–9558. https://doi.org/10.1021/acs.est.3c00864.
151. Zhou, T.; Huang, J.; Zhao, W.; Guo, R.; Cui, S.; Li, Y.; Kadasala, N.R.; Jiang, Y.; Liu, Y.; Zhang, Q. A Multifunctional Nanoplatform Based on Fe3O4@Au NCs with Magnetic Targeting Ability for Single NIR Light-Triggered PTT/PDT Synergistic Therapy of Cancer. *J. Alloys Compd.* **2023**, *944*, 169206. https://doi.org/10.1016/j.jallcom.2023.169206.
152. Chen, S.; Huang, B.; Pei, W.; Xu, Y.; Jiang, Z.; Li, J.; Wang, L.; Niu, C. Magnetically Targeted Nanoparticles for Imaging-Guided Photothermal Therapy of Cancer. *RSC Adv.* **2019**, *9*, 38154–38164. https://doi.org/10.1039/C9RA08281F.
153. Milan, J.; Niemczyk, K.; Kus-Liśkiewicz, M. Treasure on the Earth—Gold Nanoparticles and Their Biomedical Applications. *Materials* **2022**, *15*, 3355. https://doi.org/10.3390/ma15093355.
154. Song, Y.; Qu, Z.; Li, J.; Shi, L.; Zhao, W.; Wang, H.; Sun, T.; Jia, T.; Sun, Y. Fabrication of the Biomimetic DOX/Au@Pt Nanoparticles Hybrid Nanostructures for the Combinational Chemo/Photothermal Cancer Therapy. *J. Alloys Compd.* **2021**, *881*, 160592. https://doi.org/10.1016/j.jallcom.2021.160592.

155. El-Shahawy, A.A.G.; Abdel Moaty, S.A.; Zaki, A.H.; Mohamed, N.A.E.; GadelHak, Y.; Khalid Mahmoud, R.; Ali Farghali, A. Prostate Cancer Cellular Uptake of Ternary Titanate Nanotubes/CuFe2O4/Zn-Fe Mixed Metal Oxides Nanocomposite. *Int. J. Nanomed.* **2020**, *15*, 619–631. https://doi.org/10.2147/IJN.S228279.
156. Chakinala, N.; Gogate, P.R.; Chakinala, A.G. Photocatalytic Degradation of Rhodamine-B over Mono- & Bi-Metallic TiO2 Catalysts. *Mater. Today Proc.* **2021**, *43*, 3066–3070. https://doi.org/10.1016/j.matpr.2021.01.403.
157. Kadem, A.J.; Tan, Z.M.; Mohana Suntharam, N.; Pung, S.-Y.; Ramakrishnan, S. Synthesis of CuO, ZnO and SnO2 Coupled TiO2 Photocatalyst Particles for Enhanced Photodegradation of Rhodamine B Dye. *Bull. Chem. React. Eng. Catal.* **2023**, *18*, 506–520. https://doi.org/10.9767/bcrec.19532.
158. Kusumah, A.D.; Yulizar, Y.; Apriandanu, D.O.B.; Surya, R.M. Fabrication of ZnO and ZnO/CuMoO4 for the Improvement of Photocatalytic Performance. *Vacuum* **2024**, *222*, 113034. https://doi.org/10.1016/j.vacuum.2024.113034.
159. Loka, C.; Lee, K.-S. Enhanced Visible-Light-Driven Photocatalysis of Ag/Ag2O/ZnO Nanocomposite Heterostructures. *Nanomaterials* **2022**, *12*, 2528. https://doi.org/10.3390/nano12152528.
160. Majeed, I.; Ali, H.; Idrees, A.; Arif, A.; Ashraf, W.; Rasul, S.; Khan, M.A.; Nadeem, M.A.; Nadeem, M.A. Understanding the Role of Metal Supported on TiO2 in Photoreforming of Oxygenates. *Energy Adv.* **2022**, *1*, 842–867. https://doi.org/10.1039/D2YA00110A.
161. Yan, F.; Wang, Y.; Zhang, J.; Lin, Z.; Zheng, J.; Huang, F. Schottky or Ohmic Metal–Semiconductor Contact: Influence on Photocatalytic Efficiency of Ag/ZnO and Pt/ZnO Model Systems. *ChemSusChem* **2014**, *7*, 101–104. https://doi.org/10.1002/cssc.201300818.
162. Takhar, V.; Banerjee, R. Emerging Photocatalytic Applications of Transition Metal Dichalcogenides and Hybrid Composites for Energy Applications and Environmental Remediation. *ChemCatChem* **2025**, *17*, e00405. https://doi.org/10.1002/cctc.202500405.
163. Manuel, A.; Shankar, K. Hot Electrons in TiO2–Noble Metal Nano-Heterojunctions: Fundamental Science and Applications in Photocatalysis. *Nanomaterials* **2021**, *11*, 1249. https://doi.org/10.3390/nano11051249.
164. Chen, L.; Hu, H.; Chen, Y.; Gao, J.; Li, G. Plasmonic Cu2−xS Nanoparticles: A Brief Introduction of Optical Properties and Applications. *Mater. Adv.* **2021**, *2*, 907–926. https://doi.org/10.1039/D0MA00837K.
165. Velgosova, O.; Mačák, L.; Lisnichuk, M.; Varga, P. Influence of PH and Temperature on the Synthesis and Stability of Biologically Synthesized AgNPs. *Appl. Nano* **2025**, *6*, 22. https://doi.org/10.3390/applnano6040022.
166. Farooq, S.; Wali, F.; Zezell, D.M.; de Araujo, R.E.; Rativa, D. Optimizing and Quantifying Gold Nanospheres Based on LSPR Label-Free Biosensor for Dengue Diagnosis. *Polymers* **2022**, *14*, 1592. https://doi.org/10.3390/polym14081592.
167. Preethi, S.; Vivek, S.; Priya, R.; Balakumar, S.; Suresh Babu, K. Enhanced Photocatalytic Performance of CuFeO2-ZnO Heterostructures for Methylene Blue Degradation Under Sunlight. *J. Mater. Sci. Mater. Electron.* **2021**, *32*, 22256–22269. https://doi.org/10.1007/s10854-021-06712-w.
168. Tang, Y.; Jiang, Z.; Xing, G.; Li, A.; Kanhere, P.D.; Zhang, Y.; Sum, T.C.; Li, S.; Chen, X.; Dong, Z.; et al. Efficient Ag@AgCl Cubic Cage Photocatalysts Profit from Ultrafast Plasmon-Induced Electron Transfer Processes. *Adv. Funct. Mater.* **2013**, *23*, 2932–2940. https://doi.org/10.1002/adfm.201203379.
169. Zahedi, M.M.; Samarin, S.K.; Abkenar, S.D.; Pebdeni, A.B.; Hosseini, M.; Kalikeri, S.; Karimi-Maleh, H. Efficient Visible Light-Driven Photodegradation of Malachite Green Dye Using Carbon Quantum Dots-MXene Nanocomposite: Synthesis, Characterization, and Performance Evaluation. *J. Taiwan Inst. Chem. Eng.* **2025**, *166*, 105521. https://doi.org/10.1016/j.jtice.2024.105521.
170. Zhao, X.; Mao, L.; Feng, S.; Zhang, C.; Shi, Z.; Chang, N.; Wang, H. Bimetallic Synergetic Regulating Effect on Electronic Structure in Co/V Co-Doped ZnIn2S4 towards Enhancing Photocatalytic Activity. *Mater. Res. Bull.* **2026**, *195*, 113878. https://doi.org/10.1016/j.materresbull.2025.113878.
171. Sahu, N.; Parida, K.M. Photocatalytic Activity of Au/TiO2 Nanocomposite for Azo-Dyes Degradation. *Kinet. Catal.* **2012**, *53*, 197–205. https://doi.org/10.1134/S0023158412020097.
172. Paul, K.K.; Giri, P.K. Role of Surface Plasmons and Hot Electrons on the Multi-Step Photocatalytic Decay by Defect Enriched Ag@TiO_2 Nanorods Under Visible Light. *J. Phys. Chem. C* **2017**, *121*, 20016–20030. https://doi.org/10.1021/acs.jpcc.7b05328.
173. Sewnet, A.; Alemayehu, E.; Abebe, M.; Mani, D.; Thomas, S.; Lennartz, B. Hydrothermal Synthesis of Heterostructured G-C3N4/Ag–TiO2 Nanocomposites for Enhanced Photocatalytic Degradation of Organic Pollutants. *Materials* **2023**, *16*, 5497. https://doi.org/10.3390/ma16155497.
174. Mei, X.; Yuan, H.; Li, C. Study on the MOF Frame Pt-TiO2 Hybrid Photocatalyst and Its Photocatalytic Performance. *Sustainability* **2023**, *15*, 1403. https://doi.org/10.3390/su15021403.

175. Sahu, P.; Das, D. Two-Step Visible Light Photocatalytic Dye Degradation Phenomena in Ag2O-Impregnated ZnO Nanorods via Growth of Metallic Ag and Formation of ZnO/Ag0/Ag2O Heterojunction Structures. *Langmuir* **2022**, *38*, 4503–4520. https://doi.org/10.1021/acs.langmuir.1c02860.
176. Lee, S.J.; Jung, H.J.; Koutavarapu, R.; Lee, S.H.; Arumugam, M.; Kim, J.H.; Choi, M.Y. ZnO Supported Au/Pd Bimetallic Nanocomposites for Plasmon Improved Photocatalytic Activity for Methylene Blue Degradation Under Visible Light Irradiation. *Appl. Surf. Sci.* **2019**, *496*, 143665. https://doi.org/10.1016/j.apsusc.2019.143665.
177. Gavade, N.L.; Babar, S.B.; Kadam, A.N.; Gophane, A.D.; Garadkar, K.M. Fabrication of M@Cu$_x$O/ZnO (M= Ag, Au) Heterostructured Nanocomposite with Enhanced Photocatalytic Performance Under Sunlight. *Ind. Eng. Chem. Res.* **2017**, *56*, 14489–14501. https://doi.org/10.1021/acs.iecr.7b03168.
178. Malefane, M.E.; Khutlane, J.T.; Managa, M.; van Sittert, C.G.C.E.; Nkambule, T.T.I.; Kuvarega, A.T. Triple S-Scheme BiOBr@LaNiO3/CuBi2O4/Bi2WO6 Heterojunction with Plasmonic Bi-Induced Stability: Deviation from Quadruple S-Scheme and Mechanistic Investigation. *Adv. Compos. Hybrid Mater.* **2024**, *7*, 181. https://doi.org/10.1007/s42114-024-01014-1.
179. Kanakaraju, D.; Chandrasekaran, A. Recent Advances in TiO2/ZnS-Based Binary and Ternary Photocatalysts for the Degradation of Organic Pollutants. *Sci. Total Environ.* **2023**, *868*, 161525. https://doi.org/10.1016/j.scitotenv.2023.161525.
180. Yang, F.; Zhang, B.; Dong, S.; Wang, C.; Feng, A.; Fan, X.; Li, Y. Reduced Graphene Oxide Supported Pd-Cu-Co Trimetallic Catalyst: Synthesis, Characterization and Methanol Electrooxidation Properties. *J. Energy Chem.* **2019**, *29*, 72–78. https://doi.org/10.1016/j.jechem.2018.02.007.
181. 181. do Carmo Neto, J.R.; Franco, P.I.R.; Braga, Y.L.L.; de Oliveira, J.F.; Perini, H.F.; Albuquerque, L.F.D.; Martins, D.B.; Helmo, F.R.; Andrade, A.A.; Miguel, M.P.; et al. Toxicity Assessment of New Ag-ZnO/AgO Nanocomposites: An In Vitro and In Vivo Approach. *J. Funct. Biomater.* **2024**, *15*, 51. https://doi.org/10.3390/jfb15030051.
182. Padervand, M.; Heidarpour, H.; Goshadehzehn, M.; Hajiahmadi, S. Photocatalytic Degradation of 3-Methyl-4-Nitrophenol over Ag/AgCl-Decorated/[MOYI]-Coated/ZnO Nanostructures: Material Characterization, Photocatalytic Performance, and in-Vivo Toxicity Assessment of the Photoproducts. *Environ. Technol. Innov.* **2021**, *21*, 101212. https://doi.org/10.1016/j.eti.2020.101212.
183. Das, S.; Sanjay, M.; Kumar, S.; Sarkar, S.; Tiwary, C.S.; Chowdhury, S. Magnetically Separable MnFeCoNiCu-Based High Entropy Alloy Nanoparticles for Photocatalytic Oxidation of Antibiotic Cocktails in Different Aqueous Matrices. *Chem. Eng. J.* **2023**, *476*, 146719. https://doi.org/10.1016/j.cej.2023.146719.
184. Paul, R.K.; Ahmaruzzaman, M. Advanced Photocatalytic Degradation of POPs and Other Contaminants: A Comprehensive Review on Nanocomposites and Heterojunctions. *RSC Adv.* **2025**, *15*, 31313–31359. https://doi.org/10.1039/D5RA04336K.
185. Sun, Y.; Wang, X.; Lee, H.L. Enhanced Photodegradation of Ceftazidime by BiOBr(110)/BiOCl(110) Composite: Its Synthesis, Mechanism, and Degradation Pathways. *J. Environ. Chem. Eng.* **2024**, *12*, 113332. https://doi.org/10.1016/j.jece.2024.113332.
186. Ali, A.M.; Ghazwani, N.A.; Algarni, H.; Ismail, A.A. Structural, Optical Properties of ZnO Doped SnO_2 Nanocomposites with Enhanced Photocatalytic Performance Under UV Illumination. *Mater. Res. Express* **2019**, *6*, 065026. https://doi.org/10.1088/2053-1591/ab0cdd.
187. An, S.S.A.; Yi, D.K.; Ramasamy, M.; Das, M. Role of Surface Modification in Zinc Oxide Nanoparticles and Its Toxicity Assessment toward Human Dermal Fibroblast Cells. *Int. J. Nanomed.* **2014**, *9*, 3707–3718. https://doi.org/10.2147/IJN.S65086.
188. Chandrasekaran, K.; Kakani, V.; Kokkarachedu, V.; Abdulrahman Syedahamed, H.H.; Palani, S.; Arumugam, S.; Shanmugam, A.; Kim, S.; Kim, K. Toxicological Assessment of Divalent Ion-Modified ZnO Nanomaterials through Artificial Intelligence and in Vivo Study. *Aquat. Toxicol.* **2024**, *267*, 106826. https://doi.org/10.1016/j.aquatox.2023.106826.
189. Abdi, J.; Vossoughi, M.; Mahmoodi, N.M.; Alemzadeh, I. Synthesis of Metal-Organic Framework Hybrid Nanocomposites Based on GO and CNT with High Adsorption Capacity for Dye Removal. *Chem. Eng. J.* **2017**, *326*, 1145–1158. https://doi.org/10.1016/j.cej.2017.06.054.
190. Naikoo, G.A.; Bano, M.; Hassan, I.U.; Ayyub, M.M.; Zamani Pedram, M. Trimetallic CuO/Ag/NiO Supported with Silica Nanoparticles Based Composite Materials for Green Hydrogen Production. *Sci. Rep.* **2023**, *13*, 16909. https://doi.org/10.1038/s41598-023-43697-4.
191. Malankowska, A.; Mikołajczyk, A.; Mędrzycka, J.; Wysocka, I.; Nowaczyk, G.; Jarek, M.; Puzyn, T.; Mulkiewicz, E. The Effect of Ag, Au, Pt, and Pd on the Surface Properties, Photocatalytic Activity and Toxicity of Multicomponent TiO_2-Based Nanomaterials. *Environ. Sci. Nano* **2020**, *7*, 3557–3574. https://doi.org/10.1039/D0EN00580K.
192. Gakis, G.P.; Aviziotis, I.G.; Charitidis, C.A. A Structure–Activity Approach towards the Toxicity Assessment of Multicomponent Metal Oxide Nanomaterials. *Nanoscale* **2023**, *15*, 16432–16446. https://doi.org/10.1039/D3NR03174H.

193. Zhu, Z.; Ouyang, H.; Ling, C.; Ma, M.; Wang, J.; Yu, X.; Li, Y. Fabrication of Magnetic α -Fe2O3/Fe3O4 Heterostructure Nanorods via the Urea Hydrolysis-Calcination Process and Their Biocompatibility with LO_2 and $HepG_2$ Cells. *Nanotechnology* **2023**, *34*, 505711. https://doi.org/10.1088/1361-6528/acf939.
194. Li, A.; Yang, Y.; Bai, X.; Bao, H.; He, M.; Zeng, X.; Wang, Y.; Li, F.; Qin, S.; Yang, W.; et al. Trimetallic MOF–Derived Fe–Mn–Sn Oxide Heterostructure Enabling Exceptional Catalytic Degradation of Organic Pollutants. *J. Colloid Interface Sci.* **2025**, *679*, 232–244. https://doi.org/10.1016/j.jcis.2024.10.098.
195. Kim, S.-H.; Lee, J.H.; Jung, K.; Yang, J.-Y.; Shin, H.-S.; Lee, J.P.; Jeong, J.; Oh, J.-H.; Lee, J.K. Copper and Cobalt Ions Released from Metal Oxide Nanoparticles Trigger Skin Sensitization. *Front. Pharmacol.* **2021**, *12*, 627781. https://doi.org/10.3389/fphar.2021.627781.
196. Sotiriou, G.A.; Hirt, A.M.; Lozach, P.-Y.; Teleki, A.; Krumeich, F.; Pratsinis, S.E. Hybrid, Silica-Coated, Janus-Like Plasmonic-Magnetic Nanoparticles. *Chem. Mater.* **2011**, *23*, 1985–1992. https://doi.org/10.1021/cm200399t.
197. Su, J.; Zhang, Y.; Xu, S.; Wang, S.; Ding, H.; Pan, S.; Wang, G.; Li, G.; Zhao, H. Highly Efficient and Recyclable Triple-Shelled Ag@Fe3O4@SiO2@TiO2 Photocatalysts for Degradation of Organic Pollutants and Reduction of Hexavalent Chromium Ions. *Nanoscale* **2014**, *6*, 5181–5192. https://doi.org/10.1039/c4nr00534a.
198. Lin, F.; Doong, R. Bifunctional Au−Fe_3O_4 Heterostructures for Magnetically Recyclable Catalysis of Nitrophenol Reduction. *J. Phys. Chem. C* **2011**, *115*, 6591–6598. https://doi.org/10.1021/jp110956k.
199. Gao, M.; Peh, C.K.N.; Pan, Y.; Xu, Q.-H.; Ho, G.W. Fine Structural Tuning of Whereabout and Clustering of Metal–Metal Oxide Heterostructure for Optimal Photocatalytic Enhancement and Stability. *Nanoscale* **2014**, *6*, 12655–12664. https://doi.org/10.1039/C4NR03373F.
200. Alex, K.V.; Silva, J.P.B.; Kamakshi, K.; Sekhar, K.C. Ternary Heterostructures Based on $BaTiO_3$/MoO_3/Ag for Highly Efficient and Reusable Photocatalytic Applications. *Adv. Mater. Interfaces* **2023**, *10*, 2201948. https://doi.org/10.1002/admi.202201948.
201. Wu, K.; Wang, X.-Y.; Guo, L.-L.; Xu, Y.-J.; Zhou, L.; Lyu, Z.-Y.; Liu, K.-Y.; Si, R.; Zhang, Y.-W.; Sun, L.-D.; et al. Facile Synthesis of Au Embedded CuOx-CeO2 Core/Shell Nanospheres as Highly Reactive and Sinter-Resistant Catalysts for Catalytic Hydrogenation of p-Nitrophenol. *Nano Res.* **2020**, *13*, 2044–2055. https://doi.org/10.1007/s12274-020-2806-9.
202. Zhang, N.; Xu, Y.-J. Aggregation- and Leaching-Resistant, Reusable, and Multifunctional Pd@CeO2 as a Robust Nanocatalyst Achieved by a Hollow Core–Shell Strategy. *Chem. Mater.* **2013**, *25*, 1979–1988. https://doi.org/10.1021/cm400750c.
203. Jeevarathinam, M.; Halder, A.; Manoj, A.; Asharani, I.V. A Catalytic Reduction of 4-Nitrophenol Utilizing Bimetallic CuO-Co3O4 Nanoparticles Synthesized via Wrightia Tinctoria Extract: A Green Approach. *Asian J. Chem.* **2024**, *36*, 1161–1167. https://doi.org/10.14233/ajchem.2024.31402.
204. Manjari, G.; Saran, S.; Devipriya, S.P.; Rao, A.V.B. Novel Synthesis of Cu@ZnO and Ag@ZnO Nanocomposite via Green Method: A Comparative Study for Ultra-Rapid Catalytic and Recyclable Effects. *Catal. Letters* **2018**, *148*, 2561–2571. https://doi.org/10.1007/s10562-018-2435-z.
205. Dabagh, S.; Haris, S.A.; Isfahani, B.K.; Ertas, Y.N. Silver-Decorated and Silica-Capped Magnetite Nanoparticles with Effective Antibacterial Activity and Reusability. *ACS Appl. Bio Mater.* **2023**, *6*, 2266–2276. https://doi.org/10.1021/acsabm.3c00122.
206. Sotiriou, G.A.; Sannomiya, T.; Teleki, A.; Krumeich, F.; Vörös, J.; Pratsinis, S.E. Non-Toxic Dry-Coated Nanosilver for Plasmonic Biosensors. *Adv. Funct. Mater.* **2010**, *20*, 4250–4257. https://doi.org/10.1002/adfm.201000985.
207. Malvindi, M.A.; De Matteis, V.; Galeone, A.; Brunetti, V.; Anyfantis, G.C.; Athanassiou, A.; Cingolani, R.; Pompa, P.P. Toxicity Assessment of Silica Coated Iron Oxide Nanoparticles and Biocompatibility Improvement by Surface Engineering. *PLoS ONE* **2014**, *9*, e85835. https://doi.org/10.1371/journal.pone.0085835.
208. Sotiriou, G.A.; Watson, C.; Murdaugh, K.M.; Darrah, T.H.; Pyrgiotakis, G.; Elder, A.; Brain, J.D.; Demokritou, P. Engineering Safer-by-Design Silica-Coated ZnO Nanorods with Reduced DNA Damage Potential. *Environ. Sci. Nano* **2014**, *1*, 144–153. https://doi.org/10.1039/c3en00062a.
209. Navarro-Palomares, E.; González-Saiz, P.; Renero-Lecuna, C.; Martín-Rodríguez, R.; Aguado, F.; González-Alonso, D.; Fernández Barquín, L.; González, J.; Bañobre-López, M.; Fanarraga, M.L.; et al. Dye-Doped Biodegradable Nanoparticle SiO2 Coating on Zinc- and Iron-Oxide Nanoparticles to Improve Biocompatibility and for in Vivo Imaging Studies. *Nanoscale* **2020**, *12*, 6164–6175. https://doi.org/10.1039/C9NR08743E.
210. Abedin, M.R.; Umapathi, S.; Mahendrakar, H.; Laemthong, T.; Coleman, H.; Muchangi, D.; Santra, S.; Nath, M.; Barua, S. Polymer Coated Gold-Ferric Oxide Superparamagnetic Nanoparticles for Theranostic Applications. *J. Nanobiotechnology* **2018**, *16*, 80. https://doi.org/10.1186/s12951-018-0405-7.

211. Mathieu, P.; Coppel, Y.; Respaud, M.; Nguyen, Q.T.; Boutry, S.; Laurent, S.; Stanicki, D.; Henoumont, C.; Novio, F.; Lorenzo, J.; et al. Silica Coated Iron/Iron Oxide Nanoparticles as a Nano-Platform for T2 Weighted Magnetic Resonance Imaging. *Molecules* **2019**, *24*, 4629. https://doi.org/10.3390/molecules24244629.
212. Nel, A.; Xia, T.; Mädler, L.; Li, N. Toxic Potential of Materials at the Nanolevel. *Science* **2006**, *311*, 622–627. https://doi.org/10.1126/science.1114397.
213. Malabanan, J.W.T.; Alcantara, K.P.; Jantaratana, P.; Pan, Y.; Nalinratana, N.; Vajragupta, O.; Rojsitthisak, P.; Rojsitthisak, P. Enhancing Physicochemical Properties and Biocompatibility of Hollow Porous Iron Oxide Nanoparticles through Polymer-Based Surface Modifications. *ACS Appl. Bio Mater.* **2023**, *6*, 5426–5441. https://doi.org/10.1021/acsabm.3c00657.
214. Rascol, E.; Daurat, M.; Da Silva, A.; Maynadier, M.; Dorandeu, C.; Charnay, C.; Garcia, M.; Lai-Kee-Him, J.; Bron, P.; Auffan, M.; et al. Biological Fate of Fe3O4 Core-Shell Mesoporous Silica Nanoparticles Depending on Particle Surface Chemistry. *Nanomaterials* **2017**, *7*, 162. https://doi.org/10.3390/nano7070162.
215. Luo, M.; Shen, C.; Feltis, B.N.; Martin, L.L.; Hughes, A.E.; Wright, P.F.A.; Turney, T.W. Reducing ZnO Nanoparticle Cytotoxicity by Surface Modification. *Nanoscale* **2014**, *6*, 5791–5798. https://doi.org/10.1039/C4NR00458B.
216. Hsiao, I.-L.; Huang, Y.-J. Titanium Oxide Shell Coatings Decrease the Cytotoxicity of ZnO Nanoparticles. *Chem. Res. Toxicol.* **2011**, *24*, 303–313. https://doi.org/10.1021/tx1001892.
217. Arif, M.; Mahsud, A.; Ali, A.; Liao, S.; Xia, J.; Xiao, H.; Azam, M.; Muhmood, T.; Lu, Z.; Chen, Y. Unraveling the Synergy of Interface Engineering α-MnO2/Bi2WO6 Heterostructures and Defective Active Sites for Superdurable Photocatalysis: Mechanistic Insights into Charge Separation/Transfer. *Chem. Eng. J.* **2023**, *475*, 146458. https://doi.org/10.1016/j.cej.2023.146458.
218. Liu, Q.; Li, X.; Wan, Z.; Xu, D.; Liu, C. Enhanced Photocatalytic Activity and Antibacterial Potential of a Novel Ternary ZnO-Ag2MoO4-AgI Heterojunction Photocatalyst. *Colloids Surf. A Physicochem. Eng. Asp.* **2024**, *700*, 134765. https://doi.org/10.1016/j.colsurfa.2024.134765.
219. Farhang, M.; Ghadiri, A.M.; Rabbani, M.; Akbarzadeh, A.R. Z-Scheme Heterojunction g-C3N4/GO/CuFe2O4 (CGC) Nanocomposite: Enhanced Photocatalytic, Antibacterial, and Anticancer Properties. *J. Mol. Struct.* **2025**, *1325*, 139711. https://doi.org/10.1016/j.molstruc.2024.139711.
220. Naaz, K.F.; Tiwari, A.; Shaik, A.H.; P, I.; Brianna, B.; Anwar, A.; Chandan, M.R. Anti-Cancer and Antimicrobial Efficacy of ZnO Nanoparticles Synthesized via Green Route Using *Amaranthus dubius* (Spleen Amaranth) Leaves Extract. *Green Chem. Lett. Rev.* **2025**, *18*, 2453532. https://doi.org/10.1080/17518253.2025.2453532.
221. Sabit, D.A.; Ebrahim, S.E.; Jabbar, Z.H. Immobilization of 0D CuO/ZnFe2O4 Nanoparticles onto 2D BiOBr Nanoplates as Dual S-Scheme Heterostructure for Boosting Photocatalytic Oxidation of Levofloxacin in Wastewater: Magnetic Reusability and Mechanism Insights. *J. Photochem. Photobiol. A Chem.* **2023**, *443*, 114849. https://doi.org/10.1016/j.jphotochem.2023.114849.
222. Hazrati Saadabadi, R.; Shariatmadar Tehrani, F.; Sabouri, Z.; Darroudi, M. Photocatalytic Activity and Anticancer Properties of Green Synthesized ZnO-MgO-Mn2O3 Nanocomposite via *Ocimum basilicum* L. Seed Extract. *Sci. Rep.* **2024**, *14*, 29812. https://doi.org/10.1038/s41598-024-81692-5.
223. Dubey, S.; Virmani, T.; Yadav, S.K.; Kumar, G.; Sharma, A.; Gugulothu, D. Utilizing Plant Phytoconstituents in Metal Oxide Nanoparticle Synthesis for Cancer Therapies. *Curr. Pharm. Des.* **2025**, *31*, 1270–1289. https://doi.org/10.2174/0113816128329342241120105041.

Disclaimer/Publisher's Note: The statements, opinions and data contained in all publications are solely those of the individual author(s) and contributor(s) and not of MDPI and/or the editor(s). MDPI and/or the editor(s) disclaim responsibility for any injury to people or property resulting from any ideas, methods, instructions or products referred to in the content.